Long-Range Interactions in One- and Two-Electron Rydberg Atoms

VAILLANT, CHRISTOPHE,LOUIS,J

Long-Range Interactions in One- and Two-Electron Rydberg Atoms

Christophe L. Vaillant

Abstract

We present calculations of long-range interactions in Rydberg atoms, with a focus on the dipole-dipole interactions of strontium Rydberg states. The growing use of Rydberg states in the field of cold atoms necessitates a more detailed understanding of the effects of dipole-dipole interactions, which are currently being investigated in a number of research groups worldwide.

Calculations of long-range interactions in Rydberg states of caesium, calcium, rubidium, strontium and ytterbium are presented. By taking the one active electron approximation we develop consistent models of these long-range interactions, and construct a survey of the Rydberg state dipole-dipole interactions and quadrupole-quadrupole interactions. We compare the interactions between series and between atoms, highlighting the importance of certain series for applications suggested in previous works.

In order to include two-electron effects in the description of dipole-dipole interactions in divalent atoms, we use multichannel quantum defect theory (MQDT) to develop models of the Rydberg series of strontium. We use an empirical reactance matrix formalism, where the reactance matrix is fitted to reproduce experimentally measured values of the bound state energy levels. Models are found for all series of strontium with $L \leq 3$. We extend the MQDT formalism to the description of the natural radiative lifetimes of strontium, where the perturbers are found to have a large quenching effect on these lifetimes.

By incorporating the MQDT description of the Rydberg states of strontium into the calculation of dipole-dipole interactions, we find a spin-forbidden two-atom resonance in the $^3\mathrm{D}_2$ states of strontium. We consider a one-dimensional lattice of strontium atoms, and find that the internal dynamics of the Rydberg atoms demonstrates spin transport for large lattice spacings and a separation of the spin and total angular momentum dynamics for small lattice spacings. Spin-angular momentum separation (analogous to spin-charge separation in condensed matter) in strontium Rydberg atoms may have uses in the investigation of one-dimensional Fermi gases and their description using Luttinger liquid theory.

Long-Range Interactions in One- and Two-Electron Rydberg Atoms

Christophe L. Vaillant

A Thesis presented for the degree of
Doctor of Philosophy

Department of Physics
University of Durham

March 2014

Contents

List of Figures

Declaration

The work in this thesis is based on research carried out at the Atomic and Molecular Group, the Department of Physics, Durham, England. No part of this thesis has been submitted elsewhere for any other degree or qualification and it is all my own work unless referenced to the contrary in the text.

Acknowledgements

There are many people without whom this thesis would have been either non-existant or a much lower quality piece of writing, and this list is far from exhaustive!

First and foremost, I would like to thank my two supervisors, Robert Potvliege and Matt Jones. It is rare to have two supervisors who both contribute so much to a project, and (although I may not have enjoyed receiving some of the criticism at times) the comments and guidance provided by both Matt and Robert were indispensable over the three and half years I spent on this work. I would also like to give special thanks to Ifan Hughes for the many discussions, the guidance and the banter, as well as Simon Gardiner for the useful discussions and suggestions.

More generally, I have to thank the whole of the AtMol group for the good company and the countless little suggestions and bits of support provided over the years. In particular, thank you to David Szwer, Christoph Weiss, David Holdaway, John Helm, Tom Billam, Tom Ogden, James Keavney, Peter Mason and many others (I will have missed a lot of people, and I can only apologize for that!) for providing useful tips and tricks that have improved the way I work in large and small ways. A very big thank you to David Paredes especially, for the rubber-duck debugging sessions, the sports, the banter, the chocolate and everything else! Thank you as well to the whole of team strontium (past and present), Danielle Boddy, Dan Saddler, James Millen, Graham Lochead, Alistair Bounds and Liz Bridge, for discussions and many enjoyable lunches!

On a more personal side, I would like to thank my two housemates, Scott Silburn and Ophélie Lebrasseur, for keeping me sane and for being good friends for the whole seven and a half years in Durham. Thank you to my parents, for their love and moral support (as well as financial support of course), and to my grandparents for their encouragement. Finally, thank you to François Argentin, for being there.

Chapter 1

Introduction

1.1 General Introduction

Over one hundred years ago, Johannes Rydberg first derived the now famous Rydberg formula [1]. At this time, the structure of the atom was completely unknown, and the observation of transitions between atomic states represented a large step forward in the understanding of atoms (although at the time the existence of atoms had not been confirmed). Highly excited atoms (meaning atoms with large principal quantum number, n) are now known as Rydberg atoms, in honour of Johannes Rydberg's discovery.

Nowadays, Rydberg atoms are amongst the most widely understood regime of excited atoms in terms of their structure [2]. Combined with the development of laser cooling of atoms, experimental control of Rydberg atoms has reached unprecedented levels, leading to increased interest in these atomic states due to their unique properties. In particular, the physical properties of the atomic states (for example lifetimes, polarizability and van der Waals interactions) scale with principal quantum number, n, making highly excited atoms interesting for applications such as quantum information processing [3] and simulations of quantum many-body physics [4].

A number of experimental groups work in the field of cold Rydberg atoms, making use of the highly-excited atoms for applications ranging from quantum simulators [5] to the production of very high n and high l (where l is

the orbital angular momentum quantum number) atom states resembling the states of classical Bohr model [6]. Key to many of the uses of Rydberg atoms is the presence of long-range interactions between the atoms. We discuss the use of these interatomic forces in the next section.

1.1.1 Long-Range Interactions

The principal reason for the modern interest in Rydberg atoms is the magnitude of their electric dipole-dipole interactions [7]. Resonant dipole-dipole interactions (which have a functional form of R^{-3}, where R is the interatomic distance between two atoms) scale as n^4, and induced dipole-dipole interactions (usually known as van der Waals interactions) scale as n^{11} for low orbital angular momentum states [2]. Resonant dipole-dipole interactions occur for hydrogenic atoms (due to the degeneracies in l for hydrogen) and for two atoms in dipole-coupled states, whereas induced dipole-dipole interactions occur for other atoms with states not degenerate in l.

The large magnitude and tunability of these interactions over a wide range of n is of great interest, for example for the implementation of quantum information gates where the interactions between the atoms can be selectively switched on and off [3]. In particular, the strong dipole-dipole interactions can shift the energy levels of the states being addressed by laser excitation off resonance, creating what is known as the dipole blockade [8, 9]. By exploiting this blockade effect, quantum gates can be engineered that manipulate quantum bits (qubits) for non-classical computation [10]. The blockade effect has also been applied to the study of quantum optics [11].

Another avenue of research involves the study of quantum many-body physics, which is particularly challenging due to the large scaling of the Hilbert spaces with particle number. The strong interactions in Rydberg atoms enable the controlled creation of entangled many-body states, thus giving a pathway to the study of entangled quantum many-body physics [12]. The study of Rydberg lattices has also garnered attention due to the systems being strongly interacting, a regime for which few models have analytic results and have implications in the study of magnetic materials [4]. The dynamics of strongly interacting Rydberg gases have been shown to exhibit

collective behaviour at high densities [13].

Related to the research on quantum many-body physics in Rydberg atoms, the strong correlations between atoms mean that systems with Rydberg atoms can be driven into new, exotic states of matter. The strong correlations can be engineered in ground state atoms by a process known as Rydberg dressing [14], whereby weakly laser-coupling Rydberg states to the ground state atoms allows the interatomic potential to be tailored to the needs of the experiment. The Rydberg dressing procedure involves continuously coupling a cloud of atoms in ground or low-excited states, and by appropriate choice of Rabi frequency and detuning the admixture of the Rydberg character in the atomic cloud can in principle be controlled. Below a critical radius, however, the Rydberg blockade effect prevents any admixture of Rydberg character in the atomic state, allowing the potential to have a sharp cut-off. By Rydberg-dressing a Bose-Einstein condensate (BEC), the sharp cut-off in the potential has been shown to lead to a supersolid phase of matter [15], where the superfluid phase-correlations in the gas also show spatial correlations. Supersolids have been predicted in other systems for many years, although the experimental verification of this phase of matter in ^{4}He has remained highly controversial [16, 17].

We have discussed the application of Rydberg atoms to the study of quantum information technology and quantum many body physics. In the next section, we examine the particular advantages of exciting the divalent element strontium to Rydberg states for these studies.

1.1.2 Strontium Rydberg Atoms

Many experimental groups use alkali metals as the elements of choice for exciting to Rydberg states. Rubidium and caesium are amongst the most common, mainly due to the availability of diode laser systems in the wavelength region of the principal transition ($5, 6^2\mathrm{S}_{1/2} \rightarrow 5, 6^2\mathrm{P}_{1/2,3/2}$ for rubidium and caesium respectively) of these elements (which happily coincides with a range of wavelengths used for reading optical disks). The first atoms to be cooled were sodium atoms [18]. The alkaline-earth metals, however, have been largely ignored by the cold Rydberg atom community beyond earlier

studies of the structure of their Rydberg series [19]. Recently, the first experimental realisation of cold Rydberg atoms of strontium has been achieved at Durham University [20], enabling more detailed studies of the strontium Rydberg states [21, 22].

Part of the motivation for moving to alkaline-earth atoms is the existence of separate singlet and triplet spin Rydberg series, where singlet-triplet transitions are dipole forbidden [23]. Various effects (some of which will be discussed in chapter 4) lead to mixing between states, thus weakly allowing transitions between singlet and triplet states. These weak transitions mean that the 5s5p $^3P_0$ states are very long lived (and therefore the transition linewidths are very narrow); the use of these states has therefore generated interest to enter new regimes of many-body states, for example in optical lattices [24]. These lines are also commonly exploited in atomic clocks to achieve fractional uncertainties on time measurements reaching 10^{-18} [25].

Finally, the long lifetime of the 5s5p $^3P_0$ state could be used to create Rydberg-dressed BECs more easily than in alkali metal systems. Due to competing processes in three-level atomic systems, the short lifetime of the intermediate states in alkali metals means that the Rydberg dressing of a BEC requires a very large detuning from the Rydberg state, which is experimentally very challenging. The long lived 5s5p $^3P_0$ state of strontium allows for larger Rabi frequencies, hence reducing the detuning required for Rydberg dressing [14, 26]. Rydberg dressing, however, has not been achieved experimentally to date. The use of Rydberg dressing in atomic clocks has been proposed as a method of spin-squeezing the measurements (spin-squeezing is a method of reducing the quantum uncertainty on one physical variable at the expense of the conjugate variable's uncertainty) of the clock transition frequency [26].

While it appears strontium Rydberg atoms are good candidates for observing new physics experimentally, the theory efforts have been much less satisfactory in recent years. In the alkali metal atoms, many different methods are used for the calculation of Rydberg state wavefunctions (see for example [27–29]), although the range of applicability of these methods in two-electron atoms has never been conclusively studied. In strontium, the presence of

doubly-excited states can coincide in total energy, total angular momentum and parity with singly-excited Rydberg states, causing a perturbation to these Rydberg states. Effects of these doubly-excited "perturbers" include energy shifts, quenching of the Rydberg state lifetimes (as the doubly-excited states are very short lived) and allowing dipole-forbidden transitions [19, 30].

New numerical methods of calculating wavefunctions and matrix elements are necessary for a theoretical study of the properties of strontium. Currently, the only existing techniques that have been applied to the calculation of strontium Rydberg states either employ a one-electron model (completely ignoring the effects of the second electron and doubly excited states) [22] or employ complex *ab initio* techniques [31]. To our knowledge, the two-electron effects on the Rydberg states have not been comprehensively studied for principal numbers greater than $n = 10$.

The aim of the work developed in this thesis is to explore the properties of Rydberg states of strontium. We employ a range of techniques, including one-electron approximations and multichannel quantum defect theory, which ultimately allows us to explore the long-range interactions of strontium Rydberg atoms. The work is an important step in improving the descriptions of strontium Rydberg states, and paves the way for the realization of many of the studies mentioned in section 1.1.1.

1.2 Structure of the Thesis

The layout of the thesis is as follows. In chapter 2, we briefly review the theoretical background of the one-electron approximation for Rydberg atoms. Towards the end of the chapter, the use of experimental energy levels as input for a range of calculations will be detailed, with formulae and fits to these formulae included for several atoms of interest throughout this thesis. Finally, radiative lifetimes in Rydberg states of rubidium are calculated using the discussed models, demonstrating the effectiveness of these models.

Following the development of the one-electron model, chapter 3 describes the use of this model to develop the theory of long-range interactions in Rydberg atoms, and to provide calculations of long-range interactions in a variety of

atoms. The chapter will also include a discussion of the uncertainties in these calculations. The calculations are the first of their kind in strontium, calcium and ytterbium, and are also the most comprehensive calculations of the long-range interactions in rubidium and caesium.

After the important initial survey of the theory of long-range interactions, chapter 4 addresses the important question of the validity of the one-electron model for strontium. We develop details of numerical descriptions of strontium Rydberg states, making use of multichannel quantum defect theory (MQDT), which has long been used in the description of multielectron atoms [30]. The basics of the theory are reviewed, before presenting new MQDT models for Rydberg states of strontium. Finally, at the end of the chapter we show how these MQDT models can be used to numerically calculate properties such as radiative lifetimes of strontium Rydberg states.

In chapter 5, the theory of long-range interactions from chapter 3 is combined with MQDT formalism of chapter 4 and applied to the investigation of two-electron effects on the interactions of Rydberg states of strontium. We show that spin-forbidden interactions arise as a consequence of state-mixing, and that an intercombination-induced Förster resonance (a resonance feature caused by a near-degeneracy of two-atom states) arises in the $^3D_2$ series. We explore the application of this Förster resonance to a chain of Rydberg atoms, and demonstrate the separation of the spin dynamics from the dynamics of the total angular momentum, a situation that is analogous to spin-charge separation in Luttinger liquids [32].

Finally, the last chapter concludes on these investigations.

1.3 Publications Arising from this Work

The following is a list of publications that are linked with the work presented in this thesis, along with the references to the related chapters.

- **Long-range Rydberg-Rydberg interactions in calcium, strontium and ytterbium**
  C L Vaillant, M P A Jones and R M Potvliege, Journal of Physics B

45, pp. 135004 (2012).
Basis for chapter 3.

- **Multichannel Quantum Defect Theory Models of Rydberg States of Strontium**
  C L Vaillant, M P A Jones and R M Potvliege, submitted to Journal of Physics B (2014).
  Pre-print reference arXiv:1402.5802.
  Basis for chapter 4.

- **Spin-Charge Separation in Spin Chains of Strontium Rydberg Atoms**
  C L Vaillant, M P A Jones and R M Potvliege, in preparation (2014).
  Basis for chapter 5.

Another related publication not included in this thesis is

- **Cooperative Enhancement of Energy Transfer in a High-Density Thermal Vapor**
  L Weller, R Bettles, C L Vaillant, M A Zentile, R M Potvliege, C S Adams and I G Hughes, submitted to Physical Review Letters (2013).
  Pre-print reference arXiv:1308.0129.

1.4 Atomic Units

Before proceeding to a description of Rydberg atoms, it is important to include a discussion of atomic units. Atomic units are defined by setting $\hbar = m_e = e = a_0 = 1$, where $\hbar$ is Planck's constant, m_e is the mass of the electron, a_0 is the Bohr radius and e is the elementary charge (where the electron has a charge of $-e$). The resulting conversion factors are presented in table 1.1. Energies are quoted in Hartree atomic units (not in Rydberg atomic units, which differ by a factor of two).

Hartree atomic units are used throughout the thesis, unless otherwise stated.

Quantity	Symbolic Conversion Factor	Numerical Conversion Factor
Mass	m_e	$9.10938291(40) \times 10^{-31}$ Kg
Charge	e	$1.602176565(35) \times 10^{-19}$ C
Angular Momentum	$\hbar$	$1.054571726(47) \times 10^{-34}$ Js
Length	a_0	$5.2917721092(17) \times 10^{-11}$ m
Velocity	αc	$2.18769126379(71) \times 10^{6}$ ms^{-1}
Time	$a_0/\alpha c$	$2.418884326502(12) \times 10^{-17}$ s
Frequency	$\alpha c/2\pi a_0$	$6.57968392073(33) \times 10^{15}$ s^{-1}
Energy	$e^2/4\pi\epsilon_0 a_0$	$4.35974434(19) \times 10^{-18}$ J
Wave number	$\alpha/2\pi a_0$	$2.194746313708(11) \times 10^{7}$ m^{-1}

Table 1.1: Conversion factors between atomic units and SI units, as well as symbolic conversions [33]. Numbers in brackets denote the uncertainty in the corresponding value. The symbol $\alpha = 7.2973525698(24) \times 10^{-3}$ is the fine-structure constant.

Chapter 2

Rydberg Atoms

2.1 Introduction

In the introductory chapter, a non-exhaustive list of applications for Rydberg atoms was given as a motivation for the study of these highly excited states. The physics of Rydberg atoms has been studied extensively for many years, although the applications of Rydberg atoms has only begun to make an impact in the field due to the invention of laser cooling [18]. Cold atoms are not a requirement, however, for the theoretical and experimental study of the properties of Rydberg states. The alkali metals, in particular, have numerous works associated with them, with numerical techniques for the calculation of their Rydberg states being well-established [2].

In this chapter, we provide a (somewhat) brief overview of Rydberg atoms under the one-electron approximation. The goal is to develop the theoretical techniques and descriptions that will later be extended to the case of two-electron atoms. To know where we are going, we must know where we are coming from.

2.2 Rydberg Atoms

Rydberg atoms are atoms with a single electron that is excited to high values of principal quantum number n. At these large values of n, it is useful to

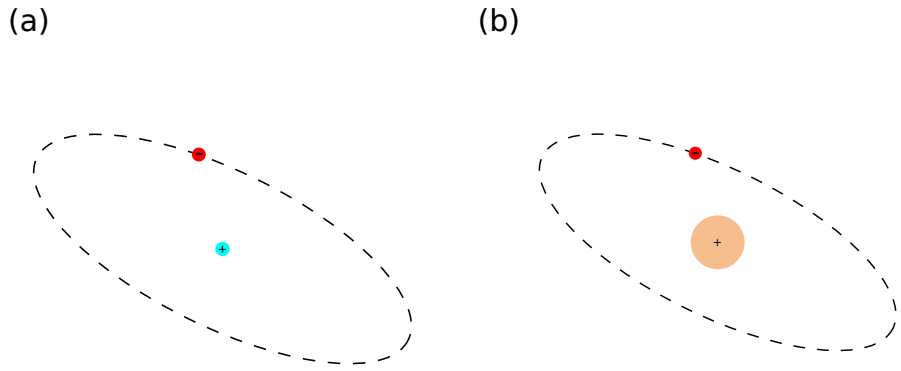

Figure 2.1: Sketch of the one-electron model. Panel (a) shows a sketch of hydrogen, with the cyan core being a proton. Panel (b) shows a sketch of a multielectron model, with the beige core being the combination of the nucleus and the other atomic electrons. The red dot for both denotes the valence electron, and the dashed line indicates a classical electron orbit.

consider the valence electron interacting with a core. A sketch of the single valence electron interacting with a core composed of the nucleus and the other atomic electrons is shown in figure 2.1. If we consider the contributions to the potential felt by the valence electron, we can split this into the attractive potential from the positive charge of the nucleus and the complicated repulsive potential due to the effect of the core electrons. When the valence electron is very far from the nucleus compared to the distance between the core electrons, then the inner core can be approximated as a polarizable charged cloud. The potential felt by the valence electron at large radial distances is therefore the sum of the long-range Coulomb potential due to the charge and the short range polarization term from the core electrons. At shorter distances ($\sim$ 1 a.u.) this breaks down due to the action of the core electrons.

To accommodate the action of the core at small distances, we introduce the quantum defect, δ. The quantum defect is a dimensionless state-dependent quantity that depends on the principal quantum number, n, and the angular momentum quantum number, l, of the atomic state. The effect of the quantum defect is to introduce an energy shift and a phase-shift in the oscillation of the wavefunction. The only remaining terms to be treated in the potential are the Coulomb potential and the core-polarization terms. Denoting the separation between the nucleus and the valence electron by $\underline{r}$ (with

magnitude r), the potential experienced by the valence electron, $V(r)$, is then

$$V(r) = -\frac{1}{r} - \frac{\alpha_{\text{core}}}{r^4}, \tag{2.1}$$

where α_{core} is the core polarizability.

For very large r, the r^{-4} core-polarization term in (2.1) can be neglected. This is known as the Coulomb approximation; this approximation will be used throughout the rest of this thesis. It can be shown by perturbative arguments that the core-polarization term leads to an energy dependence in the quantum defect [34]. This implies that knowing the state-specific quantum defect to a good accuracy is enough to account for most of the effect of core-polarization, except for an r-dependent phase-shift for small r. For Rydberg atoms, the details of the wavefunction for small r are unimportant, as the amplitude of the wavefunction is small in this region.

In non-hydrogenic atoms (hydrogenic atoms are atoms with only one electron interacting with the nucleus) the states with the same values of n but different values of l are non-degenerate. By grouping together the states that have the same value of l, the quantum defects for high n values are found to be nearly constant. We call a collection of states with the same value of l (and when spin is included, the same term symbol) and increasing values of n a Rydberg series (in chapter 4 we will see that the concept of a series is more tricky for multiple valence electrons). The energy levels for a Rydberg series, E_n, of a one-electron atom can be written as

$$E_n = -\frac{1}{2\nu^2} = -\frac{1}{2[n-\delta(n)]^2}, \tag{2.2}$$

where n is the principal quantum number, and $\nu = n - \delta(n)$ is the effective principal quantum number. For hydrogen, $\delta = 0$ and $n = \nu$, such that the principal quantum number determines the energy of the atomic state. The quantum defect, δ, therefore serves to characterize the departure from hydrogenic behaviour.

Within a Rydberg series, the principal quantum number is an important label for the states within the series. Many atomic properties depend on the value of n, not just the energy. For hydrogen, the properties of the atom depend entirely on the values of n and l (despite the degeneracy in l); in non-hydrogenic

Quantity	Scaling
Energy	n^{-2}
Energy spacing	n^{-3}
Expectation value of radius	n^{2}
Dipole matrix element	n^{2}
Radiative Lifetime	n^{3}
Polarizability*	n^{7}
van der Waals interaction*	n^{11}

Table 2.1: The scaling of different bound state properties of Rydberg atoms with the principal quantum number, n [2]. The properties marked with an asterisk are properties where this scaling is only true for non-hydrogenic atoms— in hydrogen, the degeneracy in l modifies the n-dependence.

atoms the situation is more complicated, although clear dependences on n are observed. Some of the scalings of Rydberg state properties are shown in table 2.1.

The dependence of the state properties on n arises from the n-dependence of the wavefunctions. In the next section, we examine the wavefunctions in more detail in order to elucidate the role of the principal quantum number.

2.3 Wavefunctions

The wavefunctions in one-electron atoms can differ significantly between hydrogenic atoms and non-hydrogenic atoms. In particular, the quantum defect vanishes for hydrogenic atoms, meaning that the states are degenerate in l (ignoring effects such as the Lamb shift [23]), modifying greatly the behaviour of properties such as the interatomic forces. Nevertheless, the study of hydrogenic wavefunctions yields insight into the properties of other Rydberg atoms, as the wavefunctions are analytic. In this section we will first discuss the behaviour of wavefunctions for hydrogen (in particular looking at the scaling with n) before examining the differences between hydrogen and non-hydrogenic atoms.

2.3.1 Hydrogen

The hydrogen atom is the simplest atom, and is one of the purest examples of the quantum two-body problem. Hydrogen is also the only atom whose wavefunctions can be calculated analytically. The wavefunctions and bound state energies can be determined with the knowledge of the values of the principal quantum number, n and the orbital angular momentum quantum number, l. For this section we will ignore the effect of spin, which causes small splittings of the energy levels due to the spin-orbit coupling; this splitting is known as the fine structure splitting.

The time-independent Schrödinger equation for the internal motion of atomic hydrogen is simply given by the equation

$$\left[-\frac{\nabla^2}{2} - \frac{1}{r}\right]\psi_{nlm} = E_{nlm}\psi_{nlm}, \tag{2.3}$$

where l is the orbital angular momentum quantum number, m is the magnetic quantum number, r is the radial distance of the electron from the nucleus (taken to be a point charge of infinite mass) and E_{nlm} is the energy for the state uniquely labelled by the quantum numbers n, l and m, with wavefunction ψ_{nlm}. The eigenfunctions for (2.3) are given by [23]

$$\psi_{nlm} = -\left[\left(\frac{2}{n}\right)^3 \frac{(n-l-1)!}{2n[(n+l)!]^3}\right]^{1/2} e^{-r/2} r^l L_{n+l}^{2l+1}(r) Y_{lm}(\theta,\phi), \tag{2.4}$$

where $Y_{lm}(\theta,\phi)$ is a spherical harmonic, θ and ϕ are angular coordinates (using spherical polar coordinates) and $L_{n+l}^{2l+1}(r)$ is an associated Laguerre polynomial given by [23]

$$L_{n+l}^{2l+1}(r) = \sum_{k=0}^{n-l-1} (-1)^{k+1} \frac{[(n+l)!]^2}{(n-l-1-k)!(2l+1+k)!} \frac{r^k}{k!}. \tag{2.5}$$

Using (2.4), the expectation value of the radial distance is then given by

$$\langle r\rangle_{nlm} = n^2\left\{1 + \frac{1}{2}\left[1 - \frac{l(l+1)}{n^2}\right]\right\}. \tag{2.6}$$

The n^2 scaling of $\langle r\rangle_{nlm}$, as noted in table 2.1, can thus be seen to arise from a combination of the normalization of the atomic wavefunction in (2.4) and the pre-factors appearing in the associated Laguerre polynomial in (2.5). While the situation is different in non-hydrogenic atoms due to the presence of the core electrons, the same scaling can be seen in the Rydberg states.

2.3.2 Non-Hydrogenic Atoms

In non-hydrogenic atoms, the low-excited and ground states of the atom involve the valence electron interacting heavily with the core electrons (indeed, symmetrization renders even the simple picture of a valence electron and core electrons non-sensical), making these states very different from the hydrogenic picture discussed above. For Rydberg states, however, the wavefunction of the valence electron is far more extended, and there is very little overlap between the wavefunctions of the core electrons and the valence electron. The Coulomb potential in (2.1) dominates at large r, meaning that the Coulomb approximation improves for higher values of n.

One cannot simply substitute $n \to \nu$ for the wavefunctions, as was done for the energy levels. The wavefunctions are not eigenstates of the Coulomb potential when the substitution $n \to \nu$ is made. In fact, wavefunctions for non-hydrogenic atoms are not analytic, meaning that the wavefunctions can only be calculated numerically. Some numerical methods for one-electron non-hydrogenic atoms will be discussed in section 2.4.1.

Despite the lack of analytic solutions for non-hydrogenic atoms, most differences between hydrogenic and non-hydrogenic Rydberg state wavefunctions are quite small. The first difference is that the wavefunctions are non-degenerate in l, hence the scaling laws that are true in hydrogen are not necessarily directly applicable to non-hydrogenic atoms. A good example is the Stark shift, where electric fields shift the energy of the bare states. In hydrogen, the shift is dominated by the linear term due to the degeneracy in l [23]. In other atoms, however, the non-degeneracy in l implies that the linear term is zero, making the quadratic Stark shift the dominant term. The differences between the linear and quadratic terms also implies that the n-scaling laws for the Stark shifts differ between hydrogen and other atoms (as highlighted in table 2.1).

The second difference in the wavefunctions comes about due to a small admixture between the different solutions of the Schrödinger equation. This admixture is the source of the phase-shift in the wavefunction, and is caused by the interaction of the Rydberg electron with the core. The different solutions of the Schrödinger equation will be discussed in section 2.4.1.

2.4 Rydberg State Transitions

Many properties of atoms arise due to their interactions with electromagnetic fields. Even when no external fields are applied, the atoms can still be affected by interactions with electromagnetic radiation. The vacuum field, for example, causes spontaneous emission from excited states to lower excited states or the ground state [35]. The interaction of atoms with electromagnetic fields depends crucially on transitions between different atomic states.

For Rydberg states, the interaction of the atom with electromagnetic fields can be separated into two types of transitions: Rydberg state to Rydberg state transitions, and Rydberg to low-excited state transitions. These two different cases lead to different scalings with n, as the dominant coupling terms behave in different ways. For example, we contrast the radiative lifetime of Rydberg states and the interaction of Rydberg atoms with static electric fields. In the case of radiative lifetimes, the dominant contributions are from Rydberg to low excited state transitions induced by the absorption of photons from the vacuum. The scaling of the lifetimes make Rydberg atoms particularly well-suited to the storage and manipulation of qubit states [36]. Electric fields, however, couple states that lie close together in energy, meaning that the polarizability of Rydberg states is dominated by Rydberg to Rydberg state transitions. The large polarizability of Rydberg atoms makes them extremely sensitive to electric fields, and Rydberg atoms have been used for sensitive electrometry [37].

Many radiative properties of atoms (i.e. the properties of the atoms interacting with electromagnetic radiation), such as the natural lifetimes, depend crucially on the dipole moment of particular transitions (especially if the radiation is resonant with the transition). In an electromagnetic field, the matrix element describing the transition probability between state a and state b, with energy separation $\omega = E_b - E_a$, is given by [23]

$$M_{ba} = \langle b|e^{i\underline{k}.\underline{r}}\underline{\hat{\epsilon}} \cdot \underline{\nabla}|a\rangle, \tag{2.7}$$

where $\omega = |\underline{k}|c$ ($\underline{k}$ points in the direction of propagation of the light) and $\underline{\hat{\epsilon}}$ is the polarization of the light. For the full time-dependent transition probability it is necessary to integrate over all frequencies, while including the

spectral function of the light, although the properties of atomic transitions depend mostly on the matrix element in (2.7). A full derivation of various quantities such as absorption widths that arise from atom-light interactions can be found in [23].

Using a Maclaurin expansion of the exponential term in (2.7), such that $e^{i\underline{k}.\underline{r}} \approx 1 + i\underline{k} \cdot \underline{r} + O(k^2 r^2)$, we note that, for optical transitions, $k\langle r \rangle \ll 1$, and the exponential can be safely approximated to unity. This approximation is known as the dipole approximation, and constitutes one of the most important approximations in the study of atom-light interactions. There are many situations where this approximation breaks down (for example in strong-field physics [38]), although for Rydberg atoms interacting with visible light the approximation is generally well justified.

By using the Heisenberg equation of motion,

$$\frac{dA}{dt} = \frac{\partial A}{\partial t} - i[A, H], \tag{2.8}$$

where A is an operator and $H = -(\underline{\nabla}^2/2) - (1/r)$ is the unperturbed Hamiltonian of the system, and rewriting the $\underline{\nabla}$ term using $\underline{p} = m\dot{\underline{r}} = i\hbar\underline{\nabla}$, the matrix element in (2.7) can be written in its final form as

$$M_{ba} = -\omega\langle b|\underline{\epsilon} \cdot \underline{r}|a\rangle. \tag{2.9}$$

We thus see that the transitions induced by the absorption and emission of light is proportional to the matrix element of the dipole operator, $\langle b|\underline{D}|a\rangle$ (where $\underline{D} = e\underline{r}$). The interaction with external electric fields also turns out to be dependent on the dipole matrix element.

2.4.1 Calculation of Dipole Matrix Elements

The dipole matrix elements (which scale as n^2) are crucial properties of Rydberg transitions, whether the transition is to another Rydberg state or to a low excited or ground state. Dipole matrix elements are key to many of the calculations presented in this thesis, therefore it is worth examining these matrix elements in some detail.

Two methods will be used: a semiclassical approximation, and the quantum defect theory (QDT) method. The first makes use of semiclassical

approximations to obtain a semianalytic expression for the dipole matrix elements, which can be rapidly evaluated when precise values of the energy levels of the two states are known. This semiclassical technique is particularly well-suited for the calculation of Rydberg-Rydberg state transitions. The second method, QDT, makes use of the properties of the eigenfunctions of the Coulomb equation, and accounts for the deviation from purely hydrogenic wavefunctions by using the quantum defect. Thus, the wavefunctions can be obtained numerically and applied to the calculation of the dipole matrix elements. The QDT method is well-suited for Rydberg-Rydberg, Rydberg-excited and Rydberg-ground state transitions, and is the most flexible method of calculation for dipole matrix elements.

We note another common method of calculating Rydberg atom wavefunctions involving the use of model potentials, where a suitable functional form of the potential between the core and the valence electron is assumed and free parameters are fitted to reproduce experimental energy levels. Depending on the model potential, core polarization can be included [39]. This method can usually only be applied over a limited range of n, however, and requires the determination of the model potential parameters for each series of interest.

Both the semiclassical and QDT methods make use of the Coulomb approximation, which is the assumption that (for high enough n) the valence electron moves through a purely Coulombic potential at large r. Starting from the Schrödinger equation in (2.3), we separate the wavefunction into radial and angular parts, such that $\psi_{nlm} = R_{nl}(r)Y_{lm}(\hat{r})$ (ignoring spin), where $\hat{r}$ denotes the angular coordinates. Separating (2.3) into its radial and angular parts, we obtain the Coulomb equation,

$$\left[-\frac{d^2}{dr^2} + \frac{l(l+1)}{r^2} + \frac{2\mu}{r}\right] u_{E,l}(r) = 2\mu E u_{E,l}(r), \tag{2.10}$$

where $u_{E,l}(r) = rR_{E,l}(r)$. The substitution $m_e \to \mu$ (where μ is the reduced mass) has been made to make (2.10) valid for all one-electron atoms under the Coulomb approximation. Note that as the full time-independent Schrödinger equation is separable, the $Y_{lm}(\hat{r})$ functions are eigenfunctions of the angular part of the full Schrödinger equation.

The dipole matrix elements are correspondingly split into angular and radial

parts, such that

$$\langle n'l'm'|\underline{r}|nlm\rangle = \langle l'm'|\hat{r}|lm\rangle\langle n'l'|r|nl\rangle, \tag{2.11}$$

where $\hat{r}$ denotes the angular coordinates of the vector $\underline{r}$ and r denotes the radial coordinate. In (2.11) we have ignored the spin, although in reality the spins and angular momenta all couple together. This will be incorporated into the calculation of the radiative lifetimes in section 2.6, although all single-atom angular matrix elements can be calculated analytically in terms of Clebsch-Gordan coefficients and Wigner-6j symbols [40]. Appendix A provides derivations of the angular matrix elements for various cases. We note that for a closed subshell $M_L^{(\text{shell})} = \sum_i m_{l_i} = 0$ and $M_S^{(\text{shell})} = \sum_i m_{s_i} = 0$, leading directly to $L^{(\text{shell})} = S^{(\text{shell})} = 0$, thus implying that there is no angular momentum contribution from the core (provided the subshell is closed).

The rest of this section is dedicated to the numerical calculations of the radial dipole matrix elements (the right hand matrix element in (2.11)).

Semiclassical Approximation

For transitions between close-lying Rydberg states, the dipole matrix elements depend largely on the behaviour of the wavefunctions at large r. For high n, the majority of the wavefunction is found in the classically allowed region (where the kinetic energy is larger than the potential energy), therefore the dipole matrix elements between Rydberg states are particularly well suited to semiclassical approximations.

We start by considering a wavefunction for (2.10) under a WKB approximation (an approximation where the wavefunction can be found using a series solution; WKB stands for Wentzel, Kramers and Brillouin, the pioneers of the technique) [41],

$$u_{E,l} = \sqrt{\frac{2}{\pi\nu^3 k}}\cos\left(\int_{r_{\max}}^{r} k(r')dr' + \frac{\pi}{4}\right), \tag{2.12a}$$

$$u_{E,l} = \sqrt{\frac{2}{\pi\nu^3 k}}\cos\left(\int_{r_{\min}}^{r} k(r')dr' - \frac{\pi}{4}\right). \tag{2.12b}$$

where

$$k(r) = \left[2E + \frac{2}{r} - \frac{\left(l+\frac{1}{2}\right)^2}{r^2}\right]^{1/2} \tag{2.13}$$

is the momentum of the valence electron, and ν is the effective principal quantum number (as in (2.2)). The quantities r_{min} and r_{max} are classical turning points (i.e. where the momentum becomes zero), such that the classically allowed region is within $r_{\text{min}} \leq r \leq r_{\text{max}}$. These turning points are given by

$$r_{\text{min,max}} = \nu^2 \left\{ 1 \pm \left[1 - \frac{\left(l + \frac{1}{2}\right)^2}{\nu^2} \right]^{1/2} \right\}. \tag{2.14}$$

We note the modification of the quantity $l(l+1) \to (l+1/2)^2$. This correction, known as Langer's correction [42], arises due to the nature of the application of the WKB approximation in this context. As the WKB approximation can only be applied in the classically allowed region of the Coulomb equation, the effect of neglecting the classically forbidden region leads to an erroneous phase for the wavefunction. This can be accounted for by the above modification of the quantity $l(l+1)$, which is equivalent to raising the potential barrier.

As noted in [41], the lower turning point is likely to have a larger error associated with it due to the effect of the core. Hence, the use of the wavefunction in (2.12b) would cause the whole spectrum to be shifted due to this error, causing a much larger error in the results. As such, the wavefunction in (2.12a) is used in the calculation of the radial dipole matrix elements, giving [41]

$$\langle \nu l | r | \nu' l' \rangle = \frac{1}{\pi \left(\nu\nu'\right)^{3/2}} \int_{r_{\text{min}}}^{r_{\text{max}}} \frac{r dr}{\sqrt{k_{\nu l}(r) k_{\nu' l'}(r)}} \cos\left[\Phi_{\nu l}(r) - \Phi_{\nu' l'}(r)\right], \tag{2.15}$$

where

$$\Phi_{\nu l}(r) = \int_{r_{\text{max}}}^{r} k_{\nu l}(r') dr'. \tag{2.16}$$

We note that we have written $\langle nl|r|n'l' \rangle$ as $\langle \nu l|r|\nu' l' \rangle$ to distinguish the latter from the hydrogenic case, following the conventions in the literature [28, 41, 43, 44].

At this point, it is convenient to rewrite (2.15). Following [43], we introduce

the parameters

$$\epsilon = \left(1 - \frac{l_c}{\nu_c}\right)^{1/2}, \tag{2.17a}$$

$$l_c = \frac{l + l' + 1}{2}, \tag{2.17b}$$

$$\nu_c = \sqrt{\nu\nu'}, \tag{2.17c}$$

where $\Delta l = l' - l$. Here, ϵ is the eccentricity of the classical Kepler orbit of the electron, and l_c and ν_c are representative values of l and ν respectively. The final results depend very weakly on the exact form chosen for l_c and ν_c, and different authors define these quantities differently [41, 43].

Historically, the calculation was most conveniently expressed as a series expansion, such that [28, 43, 44]

$$\langle \nu' l' | r | \nu l \rangle = \frac{3}{2}\nu_c^2 \left[1 - \left(\frac{l_c}{\nu_c}\right)^2\right]^{1/2} \sum_{p=0}^{\infty} \gamma^p g_p(\Delta\nu), \tag{2.18}$$

where $\gamma = \Delta l \, l_c/\nu_c$ and $\Delta\nu = \nu - \nu'$. The radial dipole matrix element is then defined by the $g_p(\Delta\nu)$ functions. Taking the first four terms in the expansion in (2.18) is enough to converge the series for small values of the angular momentum and high values of ν. Previously, the first four $g_p(\Delta\nu)$ functions were interpolated using tabulated values of the functions [28, 44], although the values can also be expressed in terms of Anger functions [41, 43],

$$\mathcal{J}_s(x) = \frac{1}{\pi}\int_0^{\pi} d\theta \cos\left(s\theta - x\sin\theta\right). \tag{2.19}$$

The first four $g_p(\Delta\nu)$ functions are thus given by [43]

$$g_0(\Delta\nu) = \frac{1}{3\Delta\nu}\left[\mathcal{J}_{\Delta\nu-1}(-\Delta\nu) - \mathcal{J}_{\Delta\nu+1}(-\Delta\nu)\right], \tag{2.20a}$$

$$g_1(\Delta\nu) = -\frac{1}{3\Delta\nu}\left[\mathcal{J}_{\Delta\nu-1}(-\Delta\nu) + \mathcal{J}_{\Delta\nu+1}(-\Delta\nu)\right], \tag{2.20b}$$

$$g_2(\Delta\nu) = g_0(\Delta\nu) - \frac{\sin\pi\Delta\nu}{\pi\Delta\nu}, \tag{2.20c}$$

$$g_3(\Delta\nu) = \frac{\Delta\nu}{2} g_0(\Delta\nu) + g_1(\Delta\nu). \tag{2.20d}$$

For completeness, we also include the radial quadrupole matrix element expansions. The selection rules for quadrupole selections are $\Delta l = 0, \pm 2$;

$\Delta l = 0$ transitions are treated separately to $\Delta l = \pm 2$ transitions. For $\Delta l = 0$ transitions we have the expansion [43]

$$\langle \nu' l | r^2 | \nu l \rangle = \frac{5}{2}\nu_c^4 \left[1 - \frac{3l_c^2}{5\nu_c^2}\right] \sum_{p=0}^{1} \gamma^{2p} Q_{2p}(\Delta\nu), \tag{2.21}$$

and for $\Delta l = \pm 2$ transitions

$$\langle \nu' l' | r^2 | \nu l \rangle = \frac{5}{2}\nu_c^4 \left[1 - \frac{(l_c+1)^2}{\nu_c^2}\right]^{1/2} \left[1 - \frac{(l_c+2)^2}{\nu_c^2}\right]^{1/2} \sum_{p=0}^{3} \gamma^{p} Q_{p}(\Delta\nu). \tag{2.22}$$

The quadrupole expansion functions, $Q_p(\Delta\nu)$, are given by

$$Q_0(\Delta\nu) = -\frac{6}{5(\Delta\nu)^2} g_1(\Delta\nu), \tag{2.23a}$$

$$Q_1(\Delta\nu) = -\frac{6}{5\Delta\nu} g_0(\Delta\nu) + \frac{6}{5}\frac{\sin(\pi\Delta\nu)}{\pi(\Delta\nu)^2}, \tag{2.23b}$$

$$Q_2(\Delta\nu) = -\frac{3}{4}\left[\frac{6}{5\Delta\nu} g_1(\Delta\nu) + g_0(\Delta\nu)\right], \tag{2.23c}$$

$$Q_3(\Delta\nu) = \frac{1}{2}\left[\frac{\Delta\nu}{2} Q_0(\Delta\nu) + Q_1(\Delta\nu)\right]. \tag{2.23d}$$

These expressions will be used in chapter 3 when evaluating the strength of quadrupole-quadrupole interactions. We note that equations (2.23) do not diverge at $\Delta\nu \to 0$ as the various terms are generally sinusoidal functions divided by polynomials; these types of functions converge to finite values (as predicted by l'Hôpital's rule).

The calculation of dipole matrix elements thus boils down to a simple integral that can be calculated numerically very precisely, given the knowledge of $\Delta\nu$ and some quantum numbers. The value of $\Delta\nu$ is fixed by the measured energy levels (see equation (2.2)), which are crucial to the calculation of dipole matrix elements calculated using the semiclassical approximation.

Figure 2.2 shows the four functions in (2.20). From the figure, it is clear that the radial dipole matrix elements decrease rapidly with the value of $\Delta\nu$; this decrease is particularly useful when deciding where to truncate large basis sets of atomic states (as will be discussed in chapter 3).

The results of the radial dipole matrix elements calculated numerically using (2.18) were compared to results from model potentials that had previously

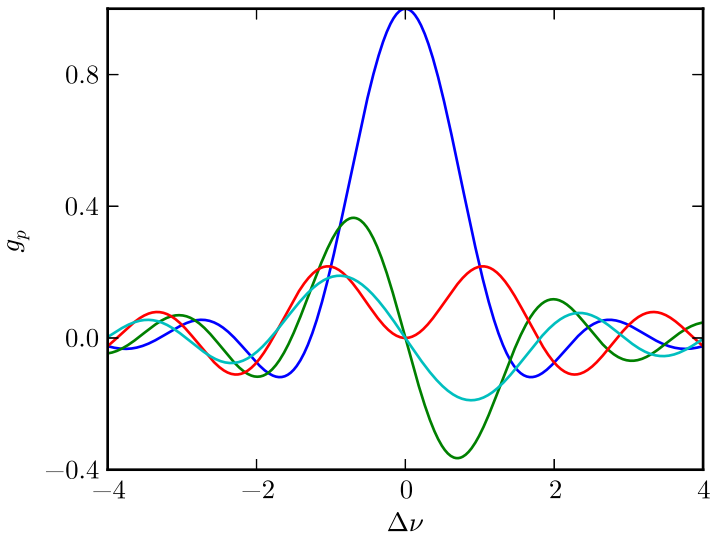

Figure 2.2: The $g_0(\Delta\nu)$ (blue curve), $g_1(\Delta\nu)$ (green curve), $g_2(\Delta\nu)$ (red curve) and $g_3(\Delta\nu)$ (cyan curve) functions defined in (2.20).

been calculated for strontium (the same energy levels were used as those output from the model potential) [22]. The difference between the two calculations were below 1%, although for lower values of n (around $n \sim 10$) the difference increased sharply, as expected from the approximations. For high values of n, this semiclassical method provides a semianalytic, and therefore rapid, way of calculating Rydberg-to-Rydberg state transitions.

Quantum Defect Theory

For many situations, transitions between high lying Rydberg states are not sufficient. The semiclassical method presented in the previous section breaks down for n as low as 20, even though the Coulomb approximation can still be valid down to much lower n. This is due to the neglect of the wavefunctions in the classically-forbidden region, an approximation which quickly breaks down when the two wavefunctions being calculated have significant overlap in the classically-forbidden region.

Quantum defect theory (QDT) is a much more general way of calculating radial matrix elements, by producing numerical wavefunctions for the valence electron. As the wavefunctions need to be determined for calculations of dipole matrix elements, QDT calculations are slower than the semiclassical

method. QDT wavefunctions, however, are applicable to more calculations than just calculations of dipole matrix elements.

QDT relies on finding numerical solutions to the Coulomb equation in (2.10) using experimentally determined values of the energy E. In this section, we define $W = -1/\nu^2$, which is the binding energy of the valence electron in Rydberg units (2 Ry = 1 a.u.). Rydberg units are used in this section only, in order to maintain consistency with [45–48] upon which this section is based.

As (2.10) is a second order differential equation, it has two linearly independent solutions. We choose to write these solutions as the regular solution, $s_{W,l}(r)$, and the irregular solution, $c_{W,l}(r)$ (so-called because the regular function is zero at the origin and the irregular solution diverges at the origin). The turning points for (2.10) are given by [45]

$$r_{\text{min,max}} = \nu^2 \left\{ 1 \pm \left[1 - \frac{l\,(l+1)}{\nu^2} \right]^{1/2} \right\}, \tag{2.24}$$

where we note that as there is no WKB approximation, (2.24) does not show the Langer correction [42]. In terms of the regular and irregular Coulomb functions, the wavefunction of the valence electron for $r \gg a_0$ is given by [48]

$$u_{W,l}(r) = s_{W,l}(r)\cos\pi\nu + c_{W,l}(r)\sin\pi\nu. \tag{2.25}$$

Numerically, to find the solution with an exponentially decreasing large-r behaviour, it is possible to use a Numerov integration method [47]. The asymptotic $r \to \infty$ behaviour of the regular and irregular Coulomb functions, $s_{W,l}(r)$ and $c_{W,l}(r)$, are given by [45]

$$s_{W,l}(r) = (-1)^l \sqrt{\frac{A(W,l)}{2}}\nu^{l+1}\left[-\frac{\theta\cos(\pi\nu)}{\Gamma(l+\nu+1)} + \frac{\eta}{\pi}\sin(\pi\nu)\Gamma(\nu-l) \right], \tag{2.26a}$$

$$c_{W,l}(r) = (-1)^l \sqrt{\frac{1}{2A(W,l)}}\nu^{l+1}\left[\frac{\theta\sin(\pi\nu)}{\Gamma(l+\nu+1)} + \frac{\eta}{\pi}\cos(\pi\nu)\Gamma(\nu-l) \right], \tag{2.26b}$$

where $\theta \sim e^{-r/\nu}(2r/\nu)^{\nu}$, $\eta \sim e^{r/\nu}(2r/\nu)^{-\nu}$ and

$$A(W,l) = \prod_{p=0}^{l}(1+p^2W). \tag{2.27}$$

Choosing a sufficiently large value of r from which to start the Numerov integration, r_{start} (we choose $r_{\text{start}} = 5n^2$, which was found to be a suitably large value for the wavefunction to be extremely small), we evaluate the wavefunction using (2.26) at r_{start} and $r_{\text{start}} - dr$, where dr is the step size. The Numerov algorithm is then used to integrate inwards until the inner turning point, r_{min} [47].

Below the inner turning point, the wavefunction becomes divergent if the Numerov integration is integrated all the way to the origin, due to the presence of the irregular solution in (2.25). To solve this, we compute the $s_{W,l}(r)$ and $c_{W,l}(r)$ functions using a series expansion in r [46]. The functions $f_{W,l}(r)$, $g_{W,l}(r)$ and $h_{W,l}(r)$ (which are linear combinations of $s_{W,l}(r)$ and $c_{W,l}(r)$) are used as they have convenient forms for the series expansion. The functions are related by

$$s(W,l,r) = \sqrt{\frac{A(W,l)}{2}} f(W,l,r), \tag{2.28a}$$

$$c(W,l,r) = \sqrt{\frac{1}{2A(W,l)}} h(W,l,r), \tag{2.28b}$$

$$h(W,l,r) = -g(W,l,r) - A(W,l)\mathcal{G}(W,l) f(W,l,r), \tag{2.28c}$$

where

$$\mathcal{G} = \frac{1}{2\pi} \Re \left[\frac{\mathrm{d}}{\mathrm{d}(\nu+l+1)} \ln \Gamma(\nu+l+1) + \frac{\mathrm{d}}{\mathrm{d}(\nu-l)} \ln \Gamma(\nu-l) - 2\ln\nu \right], \tag{2.29}$$

with $\Re$ denoting the real part.

Given a general expansion

$$f(W,l,r) = \sum_{n=0}^{\infty} a_n r^{n+l+1}, \tag{2.30}$$

the coefficients a_n can be found for both the regular and irregular functions, f and g, and a recurrence relation used to rapidly generate the numerical solution for many values of r. For the regular wavefunctions, the coefficients

are [48]

$$a_0 = \frac{2^{l+1}}{(2l+1)!}, \tag{2.31a}$$

$$a_1 = -\frac{a_0}{l+1}, \tag{2.31b}$$

$$n(n+2l+1)a_n + 2a_{n-1} + Wa_{n-2} = 0. \tag{2.31c}$$

For the irregular wavefunctions the expansions are more complicated, and the function is given by[48]

$$g(W,l,r) = \frac{1}{2\pi}\left[A(W,l)Y(W,l+\frac{1}{2},r) - Y(W,-l-\frac{1}{2},r)\right], \tag{2.32}$$

where the function $Y(W,\lambda,r)$ has the expansion

$$Y(W,\lambda,r) = \ln(r)f(W,\lambda-\frac{1}{2},r) + \sum_{n=0}^{\infty} b_n r^{n+\lambda+1/2}, \tag{2.33}$$

with coefficients

$$b_0 = \left[\ln 2 - 2\frac{\mathrm{d}}{\mathrm{d}(2\lambda+1)}\ln\Gamma(2\lambda+1)\right]a_0, \tag{2.34a}$$

$$b_1 = \left[\ln 2 - 2\frac{\mathrm{d}}{\mathrm{d}(2\lambda+2)}\ln\Gamma(2\lambda+2)\right]a_1, \tag{2.34b}$$

$$n(n+2\lambda)b_n + 2b_{n-1} + Wb_{n-2} + 2na_n = 0. \tag{2.34c}$$

Finally, once the $s_{W,l}(r)$ and $c_{W,l}(r)$ functions have been calculated, the total wavefunction can be determined using (2.25). Near the origin the valence electron penetrates the core; defining r_{core} as a length characterising the extent of the core electron wavefunctions, we see that for $r < r_{\mathrm{core}}$ fewer and fewer core electrons will contribute to the deformation of the valence electron wavefunction (working in an independent electron framework). For this reason, the quantum defect can be expected to go to zero for sufficiently small values of r, hence the wavefunction will be regular at the origin [49]. We introduce a variation of the quantum defect of the form $\delta = \delta^{(\infty)}(1 - \exp\left[-(r/r_{\mathrm{core}})^N\right])$ for $r < r_{\mathrm{core}}$, where $\delta^{(\infty)}$ is the value of the quantum defect at large r, and N is an integer (we use $N = 10$, as this gave the

best results for small values of n). For the value of r_{core}, Roothan-Hartree-Fock wavefunctions [50] can be used to determine an expectation value for the radial extent of the core electron orbitals. We find, however, that using $r_{\text{core}} = r_{\text{min}}$ produces results that do not differ significantly from using the Roothan-Hartree-Fock results.

To test the QDT calculation of the dipole matrix elements, we compare the oscillator strengths for various transitions with reference values [51] in table 2.2. The oscillator strength for a transition between state b and state a, f_{ba}, is defined as [23]

$$f_{ba} = \frac{2\omega_{ba}}{3}|\langle n_b L_b S_b J_b|\underline{r}|n_a L_a S_a J_a\rangle|^2, \tag{2.35}$$

where $\omega_{ba} = E_b - E_a$, and $\langle n_b L_b S_b J_b|\underline{r}|n_a L_a S_a J_a\rangle$ is the dipole matrix element for the transition.

Initial State	Final State	QDT Value	Reference Value	% Difference
5 $S_{1/2}$	5 $P_{1/2}$	0.347	0.3456	0.5
5 $S_{1/2}$	5 $P_{3/2}$	0.703	0.7015	0.3
7 $S_{1/2}$	8 $P_{1/2}$	0.0189	0.0185	2.2
7 $S_{1/2}$	8 $P_{3/2}$	0.0436	0.0428	2.0
5 $P_{1/2}$	7 $D_{3/2}$	0.0163	0.01711	4.4
5 $P_{3/2}$	7 $D_{3/2}$	0.00176	0.00186	5.3
5 $P_{3/2}$	7 $D_{5/2}$	0.0157	0.01657	5.2
4 $D_{3/2}$	5 $P_{1/2}$	0.304	0.3324	8.5
4 $D_{3/2}$	5 $P_{3/2}$	0.0605	0.0654	7.5
4 $D_{3/2}$	7 $P_{1/2}$	0.0118	0.0077	54.4
4 $D_{3/2}$	7 $P_{3/2}$	0.00233	0.0015	51.7
5 $D_{3/2}$	6 $P_{3/2}$	0.0989	0.0975	1.4
5 $D_{5/2}$	6 $P_{3/2}$	0.594	0.5864	1.3

Table 2.2: Comparison between some oscillator strengths of transitions between low-lying states of rubidium calculated using the QDT method (third column) and reference values (fourth column) given in [51].

The comparison of the oscillator strengths in table 2.2 shows that the QDT method works very well, even for low n states where we would not expect the Coulomb approximation to be valid. The exception is for transitions involving the $4D_J$ states, where the percentage difference between the reference

values and the calculated values can be as large as 50%, implying a very poor description of the 4D states. This poor description is unsurprising, as the effective principal quantum number ($\nu \approx 2.7$ [52]) is very close to the value of the orbital angular momentum quantum number, a regime where the Coulomb function description significantly breaks down [45].

For Rydberg states, we test the QDT method in section 2.6 using calculations of the radiative lifetimes in rubidium.

2.5 Energy Levels

In section 2.4.1, two different methods of calculating numerical wavefunctions were presented. Both methods, however, require the input of accurate binding energies for the relevant atomic states. In general, we use accurate values of the energies that have been measured experimentally, or extrapolate from fits to the quantum defects.

The quality of the available energy level data varies widely between atoms and between series. Two of the most common types of measurements are laser spectroscopy, where an energy level is determined by scanning the laser frequency and noting the position of resonances [53], and microwave spectroscopy, where microwaves are used to excite transitions between Rydberg states [54]. In general, laser spectroscopy gives a wider range of data but is less accurate, whereas fits to the quantum defects provided by microwave spectroscopy measurements are highly accurate and therefore more desirable.

Equation (2.2) relates the binding energy of the atomic state to the quantum defect, δ, of the state. For large values of n, δ is approximately constant or varies smoothly and slowly with n, making the quantum defect an excellent quantity to extrapolate. The variation of the quantum defect can be expressed using the well-known Rydberg-Ritz formula [2, 23]

$$\delta = \delta_0 + \frac{\delta_2}{(n-\delta_0)^2} + \frac{\delta_4}{(n-\delta_0)^4} + \ldots, \tag{2.36}$$

which constitutes an expansion of the quantum defect in a power series in energy (c.f. (2.2)). In order to extrapolate from the (often limited) sets of experimental energy level data, the values of the quantum defects are extracted,

and the $\delta_0, \delta_2, \delta_4 \ldots$ coefficients (also known as Rydberg-Ritz coefficients) are used as free parameters in a fitting procedure.

For the cases where fits to (2.36) are not provided by the reference, we apply a least-squares fitting procedure to obtain the Rydberg-Ritz coefficients. For this fitting procedure the cost-function, χ^2, is defined as

$$\chi^2 = \sum_i [(\delta_{\text{exp}}^{(i)} - \delta_{\text{theory}}^{(i)})/\alpha_{\text{exp}}^{(i)}]^2, \tag{2.37}$$

where i labels the particular measurement in a data set, $\delta_{\text{exp}}^{(i)}$ is the experimental measurement, $\delta_{\text{theory}}^{(i)}$ is the theory, and $\alpha_{\text{exp}}^{(i)}$ is the uncertainty on the experimental value [55]. The χ^2-function is a statistical measure of the deviation between theoretical values and the experimentally measured values, and a normal distribution between calculated and measured data results in a value of $\chi^2_\nu \sim 1$ (where $\chi^2_\nu = \chi^2/\nu$ is the reduced χ^2, and ν here is the number of degrees of freedom). We thus minimize χ^2 to find the best fit for each series.

The uncertainties in the fit parameters (in this case the Rydberg-Ritz coefficients) are then found by plotting χ^2 as a function of the fitting parameters about the minimum. The uncertainty in each parameter (neglecting correlations between the parameters) is then given by the difference in the parameter that gives a corresponding change of $\chi^2 \to \chi^2 + 1$. For the case of fits to equation (2.36), correlations between the errors of different parameters were found to be small, and are thus ignored.

Table 2.3 shows Rydberg-Ritz coefficients for rubidium and caesium. Results from microwave spectroscopy are available for both atoms; indeed, due to the usage of the caesium ground state hyperfine transition as a frequency standard, certain energy levels of caesium are particularly well known [56].

In contrast, no microwave measurements of the energy levels of strontium are available. Measurements from laser spectroscopy, however, exist for all series of strontium for S, P, D and F states, over wide ranges of n [61–70]. The highest accuracy measurements from references [61–65] are used to obtain Rydberg-Ritz coefficients, which are provided in table 2.4. The data fits (2.36) well for all series except the $^3P_2$ and $^1S_0$ series, where substantial deviations are observed for higher values of n in the ranges quoted by the

Series	δ_0	δ_2	δ_4	δ_6	δ_8	Ref.
Rb						
$ns_{1/2}$	3.1311804 (10)	0.1784 (6)				[57]
$np_{1/2}$	2.6548849 (10)	0.2900 (6)				[57]
$np_{3/2}$	2.6416737 (10)	0.2950 (7)				[57]
$nd_{3/2}$	1.34809171 (40)	-0.60286 (26)				[57]
$nd_{5/2}$	1.34646572 (30)	-0.59600 (18)				[57]
$nf_{5/2}$	0.0165192 (9)	-0.085 (9)				[58]
$nf_{7/2}$	0.0165437 (7)	-0.086 (7)				[58]
Cs						
$ns_{1/2}$	4.0493527	0.238100	0.24688	0.06785	0.1135	[59]
$np_{1/2}$	3.5914856	0.380223	-0.64771	20.9538	-84.108	[59]
$np_{3/2}$	3.5589599	0.392469	-0.67431	22.3531	-92.289	[59]
$nd_{3/2}$	2.4754562	0.009320	-0.43498	-0.76358	-18.0061	[59]
$nd_{5/2}$	2.4663091	0.014964	-0.45828	-0.25489	-19.6900	[59]
$nf_{5/2}$	0.03341424 (96)	-0.198674	0.28953	-0.2601		[60]

Table 2.3: The Rydberg-Ritz coefficients for rubidium and caesium, with uncertainties in the last digits given in brackets and references in the last column. All parameters are taken from the quoted references. The quantum defects obtained from these parameters are generally valid for $n \gtrsim 10$ (although the absolute lower bound will depend on the series and is not necessarily explored in the literature).

respective references. For the $^1S_0$ series, this has been attributed to collisional shifts with the buffer gas used in the experiment [62]. It should also be noted that the $^{1,3}D_2$ series show considerable configuration mixing, although the series are well described by equation (2.36) for $n \geq 20$. The issue of configuration mixing will be covered more thoroughly in chapter 4.

Microwave spectroscopy measurements have been performed for limited series of calcium [71, 72] and ytterbium [73], and for some other series laser spectroscopy measurements are available for calcium [65] and ytterbium [74]. Despite these measurements, the list of measured series for calcium and ytterbium is less exhaustive than those for the previously mentioned elements. Additionally, both the $^1D_2$ series of calcium and the $^1F_3$ series of ytterbium contain doubly excited perturbers that cause large deviations from (2.36); Rydberg-Ritz coefficients for these series are thus not available.

Perturbers will also be discussed in 4. The Rydberg-Ritz coefficients are shown in table 2.4. Small perturbers also exist in certain series of calcium; due to these perturbers, the term $9.08(9) \times 10^{-4}\left[(n-\delta_0)^{-2} - 0.01676700\right]^{-1}$ must be added to equation (2.36) for the 4snd ^{3}D$_2$ series, and $8.51(9) \times 10^{-4}\left[(n-\delta_0)^{-2} - 0.01685410\right]^{-1}$ must be added for the 4snd ^{3}D$_1$ series of calcium.

2.6 Radiative Lifetimes of Alkali Metals Rydberg States

In sections 2.4.1 and 2.5, all the components required for the calculation of dipole matrix elements were presented. Precision calculations of dipole matrix elements are available for low values of n [51], although there are no published precision calculations of dipole matrix elements (to the best of our knowledge) for high values of n. We therefore use experimental values of the natural radiative lifetimes, τ, of Rydberg states as a test of the calculations of dipole matrix elements.

The general expression for the natural radiative lifetime of an excited atomic state, a, is given by [23]

$$\frac{1}{\tau_a} = \frac{4\alpha^3}{3}\sum_b \omega_{ba}^3 |\langle n_b L_b S_b J_b | \underline{r} | n_a L_a S_a J_a \rangle|^2, \tag{2.38}$$

where b are dipole-coupled atomic states below a in energy, $\omega_{ba} = E_b - E_a$ and $|n_a L_a S_a J_a\rangle$ is the wavefunction for atomic state a. Here, and throughout the rest of the thesis, L denotes a total orbital angular momentum, S denotes total spin and J is the total angular momentum. The corresponding angular momenta of individual electrons are denoted by lower case letters.

For one-electron atoms, the angular dipole matrix elements can be evaluated (see appendix A) to give [27]

$$\frac{1}{\tau_a} = \frac{4\alpha^3}{3}\sum_b \omega_{ba}^3 \max(l_a, l_b)(2J'+1) \begin{Bmatrix} L & 1 & L' \\ J' & S & J \end{Bmatrix}^2 |\langle n_b l_b | r | n_a l_a \rangle|^2, \tag{2.39}$$

where the symbol with curly brackets is a Wigner-6j symbol [40], and $\langle n_b l_b | r | n_a l_a \rangle$ is the radial dipole matrix element between states a and b. Here,

Series	δ_0	δ_2	δ_4	Fitted Range	Ref.
Sr					
5sns $^1S_0$	3.26896 (2)	-0.138 (7)	0.9 (6)	$14 \leq n \leq 34$	[62]
5snp $^1P_1$	2.7295 (7)	-4.67 (4)	-157 (2)	$10 \leq n \leq 29$	[63]
5snd $^1D_2$	2.3807 (2)	-39.41 (6)	-109 (2)$\times 10^1$	$20 \leq n \leq 50$	[62]
5snf $^1F_3$	0.089 (1)	-2.0 (2)	3 (2)$\times 10^1$	$10 \leq n \leq 25$	[63]
5sns $^3S_1$	3.371 (2)	0.5 (2)	-1 (2)$\times 10^1$	$13 \leq n \leq 45$	[64]
5snp $^3P_2$	2.8719 (2)	0.446 (5)	-1.9 (1)	$8 \leq n \leq 18$	[65]
5snp $^3P_1$	2.8824 (2)	0.407 (5)	-1.3 (1)	$8 \leq n \leq 22$	[65]
5snp $^3P_0$	2.8866 (1)	0.44 (1)	-1.9 (1)	$8 \leq n \leq 15$	[65]
5snd $^3D_3$	2.63 (1)	-42.3 (3)	-18 (1) $\times 10^3$	$20 \leq n \leq 45$	[64]
5snd $^3D_2$	2.636 (5)	-1 (2)	-9.8 (9)$\times 10^3$	$22 \leq n \leq 37$	[61]
5snd $^3D_1$	2.658 (6)	3 (2)	-8.8 (7)$\times 10^3$	$20 \leq n \leq 32$	[64]
5snf $^3F_4$	0.120 (1)	-2.4 (2)	12 (2)$\times 10^1$	$10 \leq n \leq 24$	[63]
5snf $^3F_3$	0.120 (1)	-2.2 (2)	12 (2)$\times 10^1$	$10 \leq n \leq 24$	[63]
5snf $^3F_2$	0.120 (1)	-2.2 (2)	12 (2)$\times 10^1$	$10 \leq n \leq 24$	[63]
Ca					
4sns $^1S_0$	*2.337930 (3)*	*-3.96 (10)*			[71]
4snp $^1P_1$	*1.885584 (3)*	*-0.114 (3)*	*-23.8 (25)*		[71]
4snd $^1D_2$	Highly perturbed series				[71]
4snf $^1F_3$	*0.09864 (9)*	*-1.29 (9)*	*36*		[72]
4sns $^3S_1$	*2.440956 (3)*	*0.350 (3)*			[71]
4snp $^3P_2$	1.9549 (8)	2.5 (1)	-16 (1) $\times 10^1$	$12 \leq n \leq 60$	[65]
4snp $^3P_1$	*1.964709 (3)*	*0.228 (3)*			[71]
4snd $^3D_2$*	*0.8859 (5)*	*0.13 (4)*			[71]
4snd $^3D_1$*	*0.8833 (5)*	*-0.02 (4)*			[71]
Yb					
6sns $^1S_0$	*4.27914 (4)*	*-7.06 (6)*	*565 (25)*		[73]
6snp $^1P_1$	*3.95433 (5)*	*-12.33 (6)*	*1729 (27)*		[73]
6snd $^1D_2$	*2.71363 (4)*	*-2.01 (4)*			[73]
6snf $^1F_3$	Highly perturbed series				[74]

Table 2.4: The Rydberg-Ritz coefficients for strontium, calcium and ytterbium, with uncertainties in the last digits given in brackets and references in the last column. Parameters in italics are quoted from the reference. The series marked with asterisks require modifications to the Rydberg-Ritz formula due to perturbers; see the text for details. Italics denote coefficients taken from the quoted reference.

we use QDT to calculate these radial dipole matrix elements, as the states that need to be included cover a large range of n, rendering the semiclassical approximation unsuitable.

When comparing theoretical Rydberg state lifetimes to experimental results, it is important to also include the effect of blackbody radiation, as this can affect the lifetimes significantly [2]. Many authors have investigated the inclusion of blackbody radiation, using various techniques ranging from asymptotic expressions [75] to quasiclassical calculations [76]. Here, we follow the work of [77] and [27].

The average number of thermal photons with an energy of ω for a temperature T is given by

$$\langle n(\omega) \rangle = \frac{1}{e^{\omega/k_{\mathrm{B}}T} - 1}. \tag{2.40}$$

Spontaneous emission in the absence of thermal photons is due to the coupling of the excited atom to the vacuum field [35]. In the presence of thermal photons, the natural width of the state, $\Gamma_a = \tau_a^{-1}$, depends on the sum of the coupling to the thermal field and the coupling to the vacuum, such that

$$\Gamma_a = \sum_b \Gamma_b \left(1 + \frac{1}{e^{|\omega_{ab}|/k_{\mathrm{B}}T} - 1}\right) + \sum_c \frac{\Gamma_c}{e^{|\omega_{ac}|/k_{\mathrm{B}}T} - 1}, \tag{2.41}$$

where b denotes a state lower in energy to the initial state a, c denotes a state higher in energy, and Γ_b denotes the partial decay width to a single state b (given by (2.39), neglecting the sum).

Figure 2.3 shows a comparison of theoretical (with and without blackbody widths included) and experimental lifetimes [78, 79] for Rydberg states of rubidium. In general the agreement is satisfactory, although the agreement varies from series to series. The S state lifetimes show excellent agreement with both sets of data, and the D states are in excellent agreement with the data from [78]. The lifetimes from [79] for the D states, however, are slightly lower; the source of this discrepancy is unknown. The P state lifetimes show the largest deviation, with all three data sets being in disagreement with each other for some states. The theoretical lifetimes are predicted to be lower than both the experimentally measured data sets, which is probably a consequence of the poor description of the 4D states (to which the Rydberg P states couple strongly), as mentioned in section 2.4.1.

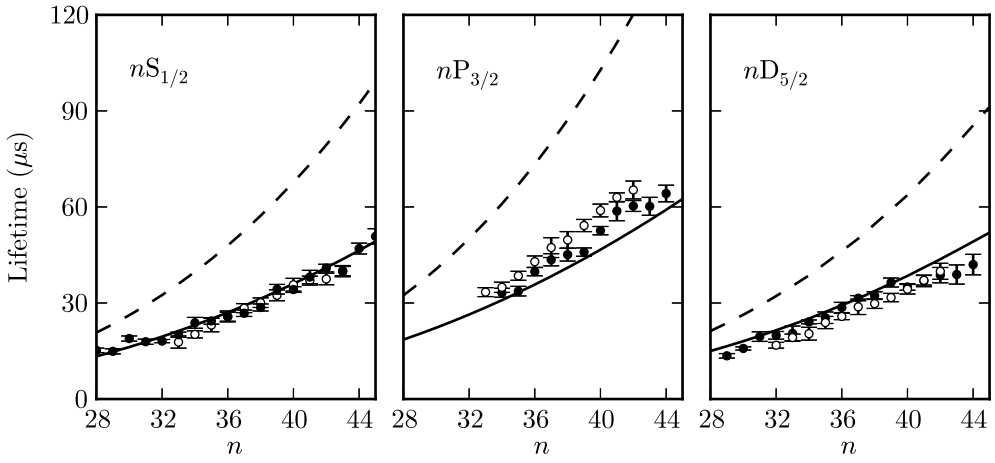

Figure 2.3: Lifetimes for rubidium Rydberg states in microseconds, as a function of the principal quantum number, n. Solid lines represent calculations of lifetimes based on QDT (see section 2.4.1) including the blackbody width for $T = 300$ K, dashed lines are QDT calculations without blackbody widths, the closed symbols are experimental data from [78] and the open symbols are experimental data from [79].

Nevertheless, the overall agreement between the experimental values of the lifetimes and the values calculated using QDT is very good, and highlights the validity of the approximations made. The application of these numerical techniques to other calculations is thus well-motivated.

2.7 Conclusions

In this chapter, we have seen a brief introduction to Rydberg atoms and their properties. The scaling of the physical properties of the atoms with the principal quantum number, n, provide a unique system for exploring the rich dynamics of quantum many-body physics. For example, the van der Waals interactions between Rydberg atoms scale as n^{11}, giving rise to strongly correlated phenomena [11, 15, 24].

The calculations of the properties of Rydberg atoms using a one-electron model have been introduced in this chapter, where we have seen that many properties of Rydberg atoms (such as radiative lifetimes, electric dipole po-

larizabilities and van der Waals interactions) depend strongly on the dipole matrix elements [23]. Two methods of calculations were presented for these dipole matrix elements. The first method of calculation involved a semiclassical approximation, valid only for transitions between close-lying Rydberg states [28, 41, 43, 44]; these types of transitions are important for the calculations of long-range interactions covered in chapter 3. The second method for calculating dipole matrix elements is known as quantum defect theory, and involves the use of Coulomb functions for the generation of any Rydberg atomic wavefunction [45–47]. QDT will be extended in chapter 4 to its multichannel version, allowing calculations of divalent Rydberg states to be explored.

Both the semiclassical and QDT methods rely heavily on the accurate knowledge of energy levels. In order to obtain accurate energy levels we have reviewed the literature to find the best available spectroscopic measurements. We described the variation of (single-channel) quantum defects (from which energy levels can be easily generated) using the Rydberg-Ritz formula [2, 23]; for series with no available fits to this formula, we used a χ^2-fitting procedure to find the Rydberg-Ritz coefficients [55].

Finally, we have showed that the wavefunctions generated by QDT reproduce the natural radiative lifetimes of the Rydberg states of rubidium. We briefly described the calculation, including the effect of blackbody radiation on the Rydberg state lifetimes [27, 77], and compared the results to experimental measurements [78, 79]. Good agreement was found, except in the P states where the description of the 4d state wavefunctions causes a significant error in the calculated lifetimes.

In the next chapter we will make use of the one-electron model to explore the long-range interactions between Rydberg states of different elements.

Chapter 3

Long-Range Interactions — One-Electron Models

3.1 Introduction

In chapters 1 and 2, the importance of long-range interactions in the study of Rydberg atoms was introduced in the context of cold atom physics. In this chapter, we develop theoretical descriptions of long-range interactions in Rydberg atoms using a one electron model.

The interactions between atoms play a key role in the study of cold atomic gases. For example, the concept of the dipole blockade has seen widespread use, where the strong dipole-dipole interactions between two Rydberg atoms shift the excitation energy off-resonance with the excitation laser, thereby preventing more than one excitation within a certain radius of the original excitation [9]. The dipole blockade is used in areas such as quantum information [3] and the implementation of two-qubit gates [80, 81], co-operative nonlinear optics [11], and the study of strongly correlated systems [82–85]. Other examples emphasizing the importance of long-range interactions in Rydberg gases include the formation of long-range molecules [86, 87] and the formation of ultracold plasmas [88].

In order to fully control systems seeking to exploit the strong long-range interactions of Rydberg atoms, detailed knowledge of these long-range in-

teractions is required. The theory of long-range interactions has been well established for some time [89, 90], although has been mostly applied to calculations of interactions for ground state atoms of interest until recently (see for example [39] for ground state alkali metal calculations of dispersion coefficients). Due to the recent interest in Rydberg atoms, many calculations have since been performed for alkali metal atoms (principally rubidium and caesium) [8, 91–95]. The studies include perturbative calculations (both of dipole-dipole interactions and quadrupole-quadrupole interactions) [8, 91, 93], and non-perturbative calculations of dipole-dipole interactions [92, 94, 95]. Our calculations reported in [96] are the first perturbative calculations of the long-range interactions between divalent Rydberg atoms, and include the effect of fine structure as well as Zeeman degeneracy and angular variations. We also compare the range of validity of the perturbative method with non-perturbative calculations.

This chapter begins by reviewing the general theory of long-range, multipolar interactions. This includes a derivation of the interaction Hamiltonian for one- and two-electron systems used in the treatment of long-range interactions, as well as detailing the perturbative treatment and the symmetries emerging from this perturbative calculation; the non-perturbative treatment is briefly mentioned. The rest of the chapter is dedicated to the behaviour of dipole-dipole and quadrupole-quadrupole interactions in various atoms.

3.2 Theory of Multipolar Interactions

3.2.1 Interaction Hamiltonian

We begin by considering two LS-coupled multielectron atoms separated by the internuclear vector $\underline{R}$, each with a single electron excited to a Rydberg state, where atom 1 is in state $|n_1 L_1 S_1 J_1 M_1\rangle$ and atom 2 is in state $|n_2 L_2 S_2 J_2 M_2\rangle$. In this chapter, we assume these Rydberg states have a high enough principal quantum number, n, such that the effects of configuration interactions are negligible; for strontium, this assumption will be seen to be valid for $n \gtrsim 30$ in chapter 4. In particular, the one-electron treatment that

will be presented in this chapter breaks down when applied to divalent atoms in the vicinity of perturbers, and in series where effects such as singlet-triplet mixing are important [61]. For the case of calcium and ytterbium, some series show perturbations from doubly excited states over a wide range of n [74, 97], and for these states the one-electron calculations we present can only be taken as estimates.

For large R (the separation between the two nuclei), we write the full Hamiltonian of the system (for both one and two-electron atoms) as

$$H = H_0 + H_{\rm int}(\underline{R}), \tag{3.1}$$

where H_0 denotes the Hamiltonian of the two atom system with infinite nuclear separation, and $H_{\rm int}(\underline{R})$ is the interaction Hamiltonian describing the interactions of the two atoms. We proceed to treat the cases of one- and two-electron long-range interaction Hamiltonians separately.

One-Electron Atoms

We first consider the simpler case of one-electron atoms. We consider atoms 1 and 2, separated by a vector $\underline{R}$, with the electron of atom 1 at position $\underline{r}_1$ and the electron of atom 2 at position $\underline{r}_2$ (both with respect to their parent atom). Figure 3.1 gives a sketch of the system of coordinates used. The bare LS-coupled wavefunctions for the one electron atoms (the eigenfunctions of the one-electron version of H_0 in (3.1), $H_0^{(1e)}$) are then given by

$$\psi^{(1e)}(\underline{r}) = \sum_{M_S,M_L} C^{JM_J}_{LM_LSM_S} R_{nl}(r) Y_{l,m}(\hat{r}) \chi_{M_S}, \tag{3.2}$$

where $C^{JM_J}_{j_1 m_{j_1} j_2 m_{j_2}}$ denotes a Clebsch-Gordan coefficient [40], and χ_{M_S} is a spinor for the single electron. As we are only considering one-electron atoms here, $l = L$, $m_l = M_L$, $s = S$ and $m_s = M_S$. Taking the origin to be at the nucleus of atom 1, the interaction Hamiltonian in (3.1) between the one-electron atoms labelled 1 and 2 is given by

$$H^{(1e)}_{\rm int} = \frac{1}{|\underline{r}_1 - \underline{r}_2 - \underline{R}|} - \frac{1}{|\underline{r}_1 - \underline{R}|} - \frac{1}{|\underline{r}_2 + \underline{R}|} + \frac{1}{R}, \tag{3.3}$$

where the first term represents the interaction between the two valence electrons, the second and third terms represent the attraction of the valence

electron of each atom with the nucleus of the other atom, and the final term represents the repulsion between each nucleus.

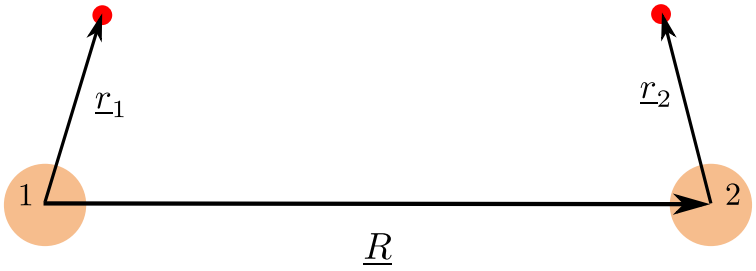

Figure 3.1: Sketch of the coordinate system used in the description of the electrostatic interactions between the electrons and the cores of the atoms in (3.3).

Provided there is no overlap between the charge clouds we can neglect exchange interactions [89] and expand the second and third terms of equation (3.3) (corresponding to the attraction between the Rydberg electron of each atom to the core of the opposite atom) in terms of Legendre functions [98, p. 597], such that

$$\begin{aligned} H_{\text{int}}^{(1e)} = & \frac{1}{|\underline{r}_1 - \underline{r}_2 - \underline{R}|} - \frac{1}{R} \\ & + \sum_{q_1=0}^{\infty} \frac{4\pi}{2q_1+1} \sum_{m_1=-q_1}^{q_1} (-1)^{m_1} \frac{r_1^{q_1}}{R^{q_1+1}} Y_{q_1,-m_1}(\hat{r}_1) Y_{q_1,m_1}(\hat{R}) \\ & + \sum_{q_2=0}^{\infty} \frac{4\pi}{2q_2+1} \sum_{m_2=-q_2}^{q_2} (-1)^{q_2+m_2} \frac{r_2^{q_2}}{R^{q_2+1}} Y_{q_2,-m_2}(\hat{r}_2) Y_{q_2,m_2}(\hat{R}) \end{aligned} \tag{3.4}$$

where q_1 and q_1 are orders of multipoles. We can write equation (3.4) as

$$H_{\text{int}}^{(1e)} = H^{(ee)} + H^{(\text{nucl})} + H^{(\text{pol})}, \tag{3.5}$$

with

$$H^{(ee)} = \frac{1}{|\underline{r}_1 - \underline{r}_2 - \underline{R}|}, \tag{3.6}$$

$$H^{(\text{nucl})} = -\frac{1}{R}, \tag{3.7}$$

and

$$\begin{aligned} H^{(\text{pol})} = & \sum_{q_1=0}^{\infty} \frac{4\pi}{2q_1+1} \sum_{m_1=-q_1}^{q_1} (-1)^{m_1} \frac{r_1^{q_1}}{R^{q_1+1}} Y_{q_1}^{-m_1}(\hat{r}_1) Y_{q_1}^{m_1}(\hat{R}) \\ & + \sum_{q_2=0}^{\infty} \frac{4\pi}{2q_2+1} \sum_{m_2=-q_2}^{q_2} (-1)^{q_2+m_2} \frac{r_2^{q_2}}{R^{q_2+1}} Y_{q_2}^{-m_2}(\hat{r}_2) Y_{q_2}^{m_2}(\hat{R}) \end{aligned} \tag{3.8}$$

corresponding to the valence electron interactions, the nuclear interactions, and the polarization of each atom from the opposite nucleus respectively. The purpose of expanding the terms in (3.3) will become more obvious in section 3.3 when we introduce the multipolar expansion of $H^{(ee)}$.

Two-Electron Atoms

For a two electron Rydberg atom, we describe the atom as having one electron in an extended outer Rydberg orbital with wavefunction ϕ_{o}, and another in a compact inner orbital, with wavefunction ϕ_{i}. We label the two electrons as electron a and electron b, with position vectors from the nucleus $\underline{r}_a$ and $\underline{r}_b$ respectively, leading to the symmetrized eigenfunction of the two-electron bare Hamiltonian $H_0^{(2e)}$,

$$\begin{aligned}\psi^{(2e)}(\underline{r}_a,\underline{r}_b) = \sum_{M_S,M_L}\sum_{m_{l_{\mathrm{i}}}m_{l_{\mathrm{o}}}}\sum_{m_{s_{\mathrm{i}}},m_{s_{\mathrm{o}}}} & C^{JM_J}_{LM_LSM_S} C^{LM_L}_{l_{\mathrm{i}}m_{l_{\mathrm{i}}}l_{\mathrm{o}}m_{l_{\mathrm{o}}}} C^{SM_S}_{s_{\mathrm{i}}m_{s_{\mathrm{i}}}s_{\mathrm{o}}m_{s_{\mathrm{o}}}} \\ & \times \left[\phi_{\mathrm{i}}(\underline{r}_a)\chi_{m_{s_{\mathrm{i}}}}(a)\phi_{\mathrm{o}}(\underline{r}_b)\chi_{m_{s_{\mathrm{o}}}}(b)\right. \\ & \qquad \left. + (-1)^S\phi_{\mathrm{i}}(\underline{r}_b)\chi_{m_{s_{\mathrm{i}}}}(b)\phi_{\mathrm{o}}(\underline{r}_a)\chi_{m_{s_{\mathrm{o}}}}(a)\right],\end{aligned} \tag{3.9}$$

where $\chi_{m_s}(a)$ and $\chi_{m_s}(b)$ are spinors for electrons a and b (i and o refer to the inner and outer orbitals respectively). The coordinate system for the two-electron atoms system is sketched in figure 3.2. Assuming the inner orbital is in its lowest energy state (the 5s state in strontium, 4s in calcium and 6s in ytterbium), the lack of angular momentum of the inner orbital implies $l_{\mathrm{i}} = m_{l_{\mathrm{i}}} = 0$ and $l_{\mathrm{o}} = L$.

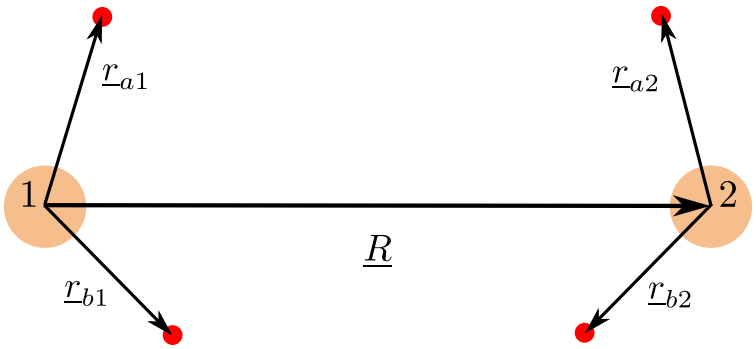

Figure 3.2: Sketch of the two-electron coordinate system used in the description of the electrostatic interactions between the electrons and the cores of the atoms.

Once again taking the origin to be the core of atom 1, the full interaction between the two-electron atoms 1 and 2 is given by

$$H_{\rm int}^{(2e)} = \sum_{\epsilon=a,b}\sum_{\epsilon'=a,b}\frac{1}{|\underline{r}_{\epsilon 1}-\underline{r}_{\epsilon' 2}-\underline{R}|} - \sum_{\epsilon=a,b}\left(\frac{2}{|\underline{r}_{\epsilon 1}-\underline{R}|}+\frac{2}{|\underline{r}_{\epsilon 2}+\underline{R}|}\right)+\frac{4}{R}, \tag{3.10}$$

where we note that the electrostatic interactions between the electrons belonging to the same atoms are implicitly accounted for in H_0.

If the inner valence electron of each two-electron atom is in a compact orbital, then the matrix elements of the first (double) sum in (3.10) associated with transitions between the compact orbitals of either atom will be small compared to the transitions between the Rydberg orbitals. These transitions will effectively be treated in chapter 5, although in this chapter we will neglect them as a first step. The matrix elements of the second sum in (3.10) associated with similar transitions between inner orbitals will also be small, hence we effectively take the inner orbital to be part of the core. By only considering the Rydberg electron, the two-electron Hamiltonian in (3.10) reduces to the one-electron Hamiltonian (3.3), which we will be using throughout the rest of this chapter. We note that this approximation is generally not applicable to ground state atoms or atoms in low excited states.

3.3 Multipolar Expansion

We use a two-centre multipolar expansion of the $H^{(ee)}$ term to obtain [89]

$$\begin{aligned} H^{(ee)} = &\sum_{k_1,k_2=0}^{\infty}\frac{(-1)^{k_2}}{R^{k_1+k_2+1}}\sqrt{\frac{(4\pi)^3(2k_1+2k_2)!}{(2k_1+1)!(2k_2+1)!(2k_1+2k_2+1)}} \\ &\times\sum_{p=-(k_1+k_2)}^{k_1+k_2}\sum_{p_1=-k_1}^{k_1}\sum_{p_2=-k_2}^{k_2} C^{k_1+k_2,p}_{k_1p_1,k_2p_2}\, r_1^{k_1} r_2^{k_2} Y_{k_1,p_1}(\hat{r}_1)Y_{k_2,p_2}(\hat{r}_2)Y_{k_1+k_2,p}(\hat{R}), \end{aligned} \tag{3.11}$$

where k_1 and k_2 denote the order of the multipole, and hats denote angular coordinates. Considering the $k_1 = k_2 = 0$ term, we see that this term cancels the $H^{(\rm nucl)}$ in (3.5). Similarly, the $k_1 = 1\ldots\infty$, $k_2 = 0$ and $k_1 = 0$, $k_2 = 1\ldots\infty$ terms cancel out $H^{(\rm pol)}$ in (3.5). The full interaction Hamiltonian

therefore simplifies to the same expression as in (3.11), with the sums of k_1 and k_2 starting from 1. The lowest order non-zero term gives rise to dipole-dipole interactions ($k_1 = k_2 = 1$), resulting in a matrix element proportional to R^{-3}.

The multipolar expansion and the assumptions made (including the neglect of exchange interactions) to arrive to equation (3.11) all hinge on there being no overlap between the charge clouds of the two atoms. The minimum value of the separation for which this overlap can be neglected can be quantified using a quantity known as the LeRoy radius, R_{LR}, defined by [99]

$$R_{\mathrm{LR}} = 2\left(\langle r_1^2\rangle^{\frac{1}{2}} + \langle r_2^2\rangle^{\frac{1}{2}}\right). \tag{3.12}$$

When the separation between the two atoms falls below the LeRoy radius, all of the approximations become invalid, as does the multipolar expansion; similar multipolar expansions can be derived for the case of overlapping charge clouds, although these become very complicated to calculate [89]. If necessary, damping functions can be used to account for this overlap [100]; however, these damping functions will not be considered in this work.

The matrix elements of (3.11) are now much simpler to solve, as these now involve multipolar matrix elements. The energy shifts due to the long-range interactions can now be found either perturbatively or non-perturbatively. A non-perturbative calculation involves the diagonalization of an effective Hamiltonian matrix representing the energies and couplings of (3.1) projected onto a basis of pairs of atoms; we refer to a pair of atoms in eigenstates of H_0 at infinite internuclear separation as pair states. This effective Hamiltonian matrix can be written as

$$H_{pq} = \delta_{pq}\mathcal{E} + V_{pq}^{(k_1k_2)}(\underline{R}), \tag{3.13}$$

where the indices p and q run over all the basis pair states, $\mathcal{E} = E_1 + E_2$ is the eigenenergy of H_0 (the sum of the two atomic energies at infinite separation), and $V_{pq}^{(k_1k_2)}(\underline{R})$ are the matrix elements of (3.11). Denoting the quantum numbers L_1, S_1, J_1, L_2, S_2, and J_2 by α, the interaction matrix element $V_{pq}^{(k_1k_2)}(\underline{R})$ for two atoms aligned with the z-axis can be written

$$\begin{aligned} V_{pq}^{(k_1k_2)}(\underline{R}) = {} & \frac{1}{R^{k_1+k_2+1}} D_{k_1k_2}(\alpha_q M_{1q}, M_{2q}, \alpha_p M_{1p} M_{2p}; \hat{R} = \hat{z}) \\ & \times \mathcal{R}_{k_1k_2}(n_{1p} n_{2p} \alpha_p; n_{1q} n_{2q} \alpha_q), \end{aligned} \tag{3.14}$$

where $D_{k_1k_2}(\alpha M_1, M_2, \alpha' M_1' M_2'; \hat{R})$ is an angular function given in appendix A and $\mathcal{R}_{k_1k_2}(n_1 n_2 \alpha, n_1' n_2' \alpha')$ is given by

$$\begin{aligned}\mathcal{R}_{k_1k_2}(n_1 n_2 \alpha, n_1' n_2' \alpha') = &\int_0^\infty dr_1 u_{n_1 L_1 S_1 J_1}(r_1) r_1^{k_1} u_{n_1' L_1' S_1' J_1'}(r_1) \\ &\times \int_0^\infty dr_2 u_{n_2 L_2 S_2 J_2}(r_2) r_2^{k_2} u_{n_2' L_2' S_2' J_2'}(r_2).\end{aligned} \tag{3.15}$$

Recall that $u_{nl}(r) = rR_{nl}(r)$ is the atomic reduced radial wavefunction. Equation (3.15) can be calculated either using the semiclassical approximation or the quantum defect theory methods of chapter 1.

The matrix elements $V_{pq}^{(k_1k_2)}(\underline{R})$ will also be used when calculating the long-range interactions perturbatively in the next section.

3.3.1 Perturbative Expansions

Non-perturbative calculations provide exact (to within numerical error) potential curves for a single term in (3.11). Perturbative calculations, however, lead to a sum over powers of R^{-1}; the coefficients associated with each power of R^{-1} in the sum provide a numerical way of comparing interactions between states, series and atoms. We write the sum over powers of R^{-1} as

$$\Delta E^{(\text{int})} = \sum_N \frac{C_N}{R^N}, \tag{3.16}$$

where $\Delta E^{(\text{int})}$ is the energy shift caused by $H^{(\text{int})}(\underline{R})$ and the C_N coefficients are state-dependent constant coefficients. We consider two atoms in the same initial Rydberg state and apply perturbation theory to find the C_N coefficients. In general, the first and second order energy shifts associated with a Hamiltonian $H = H_0 + H'$ are given by [23]

$$\Delta E^{(1)} = \langle \psi^{(0)} | H' | \psi^{(0)} \rangle \tag{3.17}$$

and

$$\Delta E^{(2)} = \sum \frac{\langle \psi^{(0)} | H' | \psi' \rangle \langle \psi' | H' | \psi^{(0)} \rangle}{E^{(0)} - E'}. \tag{3.18}$$

Here, $\psi^{(0)}$ corresponds to the unperturbed wavefunction, $E^{(0)}$ is the unperturbed energy, and the sum in (3.18) is over all (unperturbed) states that are not the initial state, with energy E' and wavefunction $|\psi'\rangle$. For clarity, we

have ignored degeneracies in (3.17) and (3.18); the degeneracies will be included at a later stage. Applying these expressions first to the dipole-dipole term in (3.11) ($k_1 = k_2 = 1$), we see that $\Delta E^{(1)} = 0$ as the initial state cannot be dipole-coupled to itself (noting the appearance of the dipole operator in the multipole expansion).

Hence, the dominant term in (3.16) is the C_6/R^6 term, arising in second order from the dipole-dipole interactions. The next largest term is the C_5/R^5, arising from the first order quadrupole-quadrupole interactions. These two terms will be the only ones considered, as the rest of the terms become sufficiently small as to be neglected [90, 91]. The dipole-quadrupole term ($k_1 = 1$, $k_2 = 2$) can become appreciable at distances very close to the LeRoy radius; however, as the validity of the multipolar expansion is questionable in this region, more advanced techniques would be required to calculate the interactions. At larger distances, the dipole-quadrupole terms can be safely ignored [91].

At infinite separation and in the absence of an external field, the two atoms are degenerate in M_J. As such, applying degenerate perturbation theory, the C_5 and C_6 coefficients are eigenvalues of $(2J_1+1)(2J_2+1)$ by $(2J_1+1)(2J_2+1)$ matrices, which we call $\mathcal{C}_5$ and $\mathcal{C}_6$ respectively. The matrix elements, $\mathcal{C}_5^{(ij)}$ and $\mathcal{C}_6^{(ij)}$ are given by

$$\mathcal{C}_5^{(ij)}(\hat{R}) = D_{22}(\alpha M_1^{(i)}, M_2^{(i)}, \alpha M_1^{(j)} M_2^{(j)}; \hat{R}) \mathcal{R}_{22}(n_1 n_2 \alpha; n_1 n_2 \alpha) \tag{3.19}$$

and

$$\begin{aligned} \mathcal{C}_6^{(ij)} = -\sum_p & \frac{|\mathcal{R}_{11}(n_1 n_2 \alpha; n_{1p} n_{2p} \alpha_p)|^2}{\Delta} \\ & \times D_{11}(\alpha M_1^{(i)}, M_2^{(i)}, \alpha_p M_{1p} M_{2p}; \hat{R}) \\ & \times D_{11}(\alpha_p M_{1p}, M_{2p}, \alpha M_1^{(j)} M_2^{(j)}; \hat{R}) \end{aligned} \tag{3.20}$$

where i and j each label a different possible value of M_1 and M_2. In (3.20), the sum is over all dipole-coupled states, p (where all the p subscripts associated with a quantity refers to that quantity for state p), and $\Delta = \mathcal{E} - \mathcal{E}_p$ (with $\mathcal{E}$ being the eigenergy associated with H_0 in (3.1)) is known as the Förster defect, which is the energy difference between the initial pair state and the intermediate pair state, p.

Thus, finding the long-range interactions for a particular state amounts to finding the eigenvalues of $\mathcal{C}_5$ and $\mathcal{C}_6$. The C_5 and C_6 coefficients scale with principal quantum number as n^8 and n^{11} respectively [101]; when comparing the coefficients between states, it is common to factor out this dependence to make a more direct comparison. The scaled coefficients are thus defined by $\tilde{C}_5 = C_5 n^{-8}$ and $\tilde{C}_6 = C_6 n^{-11}$.

3.3.2 Symmetries

When applying degenerate perturbation theory to obtain equations (3.19) and (3.20), the C_5 and C_6 coefficients were found to be eigenvalues of the matrices $\mathcal{C}_5$ and $\mathcal{C}_6$. As the interaction between the atoms lifts the degeneracy in M_J, the resulting eigenfunctions are linear combinations of pair states with different values of M_1 and M_2. In this section we describe the emergence of symmetries due to the coupling of the two atoms by the dipole-dipole and quadrupole-quadrupole interactions. To simplify the discussion, we consider the case where the internuclear axis is aligned with the z-axis, leading to $\hat{R} = \hat{z}$.

To begin, we first consider the coupling of the angular momentum operators $\underline{J}_1$ and $\underline{J}_2$, such that $\underline{J}_1 + \underline{J}_2 = \underline{\mathcal{J}}$, where $\underline{\mathcal{J}}$ is the total angular momentum operator of the atom pair. The projection of this total atom pair angular momentum onto the internuclear axis is then given by $\mathcal{J}_z$. The eigenvalues of $\mathcal{J}^2$ are $\hbar^2 \mathcal{J}(\mathcal{J}+1)$, and the eigenvalues are $\mathcal{J}$ are $\hbar\Omega$, where $\Omega = M_1 + M_2$. Examining equation (3.11), we see that $H_{\text{int}}^{(1e)}$ couples states with different values of M_J (arising from the Clebsch-Gordan coefficient and the spherical harmonics). The coupling, however, occurs in such a way that any addition of one quantum of angular momentum to one atom is associated with the removal of one quantum of angular momentum from the other atom. Consequently, we see that $\mathcal{J}_z$ commutes with $H_{\text{int}}^{(1e)}$, making Ω a good quantum number. However, $\mathcal{J}^2$ does not generally commute with $H_{\text{int}}^{(1e)}$, meaning that $\mathcal{J}$ is not always a good quantum number. The quantum number $\mathcal{J}$ can take on values ranging from $J_1 + J_2$ to $|J_1 - J_2|$, and as there is no restriction in $H_{\text{int}}^{(1e)}$ on transitions with different values of $\mathcal{J}$, the same values of J_1 and J_2 can lead to different values of $\mathcal{J}$. The ensuing coupling, for both $\hat{H}^{(5)}$ and

$\hat{H}^{(6)}$, mixes different values of $\mathcal{J}$.

Nevertheless, for low L states it is generally possible to associate a given state with an approximate value of $\mathcal{J}$ and an exact value of Ω. This coupling scheme is different from Hund's cases [102], and corresponds to the case where the atomic spin and orbital angular momenta couple more strongly to each other than the internuclear axis. Some authors use Hund's case (c) notation to describe the states (or case (a) when ignoring spin) [91, 92, 95]; however, we will describe the states by their quantum numbers $\mathcal{J}$ and Ω to avoid ambiguity.

Series	Ω	$\mathcal{J}$	Notes	Eigenvector
$^2\Sigma_{1/2}$, $^2\Pi_{1/2}$	0	0	a,b	$\lvert\frac{1}{2},-\frac{1}{2}\rangle$
	0	1	a,b	$\lvert\frac{1}{2},-\frac{1}{2}\rangle$
	1	1	a,b	$\lvert\frac{1}{2},\frac{1}{2}\rangle$
$^2\Pi_{3/2}$, $^2\Delta_{3/2}$,	0	0	a,b	$\frac{1}{2}\left(\lvert\frac{3}{2},-\frac{3}{2}\rangle - \lvert-\frac{3}{2},\frac{3}{2}\rangle - \lvert\frac{1}{2},-\frac{1}{2}\rangle + \lvert-\frac{1}{2},\frac{1}{2}\rangle\right)$
	0	1	a,b	$\frac{1}{2}\left(\lvert\frac{3}{2},-\frac{3}{2}\rangle + \lvert-\frac{3}{2},\frac{3}{2}\rangle - \lvert\frac{1}{2},-\frac{1}{2}\rangle - \lvert-\frac{1}{2},\frac{1}{2}\rangle\right)$
	0	2	b	$\frac{1}{2}\left(\lvert\frac{3}{2},-\frac{3}{2}\rangle - \lvert-\frac{3}{2},\frac{3}{2}\rangle + \lvert\frac{1}{2},-\frac{1}{2}\rangle - \lvert-\frac{1}{2},\frac{1}{2}\rangle\right)$
	0	3	b	$\frac{1}{2}\left(\lvert\frac{3}{2},-\frac{3}{2}\rangle + \lvert-\frac{3}{2},\frac{3}{2}\rangle + \lvert\frac{1}{2},-\frac{1}{2}\rangle + \lvert-\frac{1}{2},\frac{1}{2}\rangle\right)$
	1	1	a,b	$\lvert\frac{1}{2},\frac{1}{2}\rangle$
	1	2	b	$\left(\lvert\frac{3}{2},-\frac{1}{2}\rangle - \lvert-\frac{1}{2},\frac{3}{2}\rangle\right)/\sqrt{2}$
	1	3	b	$\left(\lvert\frac{3}{2},-\frac{1}{2}\rangle + \lvert-\frac{1}{2},\frac{3}{2}\rangle\right)/\sqrt{2}$
	2	2	b	$\left(\lvert\frac{3}{2},\frac{1}{2}\rangle - \lvert\frac{1}{2},\frac{3}{2}\rangle\right)/\sqrt{2}$
	2	3	b	$\left(\lvert\frac{3}{2},\frac{1}{2}\rangle + \lvert\frac{1}{2},\frac{3}{2}\rangle\right)/\sqrt{2}$
	3	3	b	$\lvert\frac{3}{2},\frac{3}{2}\rangle$
$^2\Delta_{5/2}$	0	0		$0.3440\left(\lvert\frac{5}{2},-\frac{5}{2}\rangle - \lvert-\frac{5}{2},\frac{5}{2}\rangle\right) - 0.6158\left(\lvert\frac{3}{2},-\frac{3}{2}\rangle - \lvert-\frac{3}{2},\frac{3}{2}\rangle\right) + 0.0490\left(\lvert\frac{1}{2},-\frac{1}{2}\rangle - \lvert-\frac{1}{2},\frac{1}{2}\rangle\right)$
	0	1		$0.2960\left(\lvert\frac{5}{2},-\frac{5}{2}\rangle + \lvert-\frac{5}{2},\frac{5}{2}\rangle\right) - 0.6002\left(\lvert\frac{3}{2},-\frac{3}{2}\rangle + \lvert-\frac{3}{2},\frac{3}{2}\rangle\right) + 0.2283\left(\lvert\frac{1}{2},-\frac{1}{2}\rangle + \lvert-\frac{1}{2},\frac{1}{2}\rangle\right)$
	0	2		$0.1366\left(\lvert\frac{5}{2},-\frac{5}{2}\rangle - \lvert-\frac{5}{2},\frac{5}{2}\rangle\right) + 0.0211\left(\lvert\frac{3}{2},-\frac{3}{2}\rangle - \lvert-\frac{3}{2},\frac{3}{2}\rangle\right) - 0.6935\left(\lvert\frac{1}{2},-\frac{1}{2}\rangle - \lvert-\frac{1}{2},\frac{1}{2}\rangle\right)$
	0	3		$0.3335\left(\lvert\frac{5}{2},-\frac{5}{2}\rangle + \lvert-\frac{5}{2},\frac{5}{2}\rangle\right) - 0.071\left(\lvert\frac{3}{2},-\frac{3}{2}\rangle + \lvert-\frac{3}{2},\frac{3}{2}\rangle\right) - 0.6195\left(\lvert\frac{1}{2},-\frac{1}{2}\rangle + \lvert-\frac{1}{2},\frac{1}{2}\rangle\right)$
	0	4		$0.6025\left(\lvert\frac{5}{2},-\frac{5}{2}\rangle - \lvert-\frac{5}{2},\frac{5}{2}\rangle\right) + 0.3468\left(\lvert\frac{3}{2},-\frac{3}{2}\rangle - \lvert-\frac{3}{2},\frac{3}{2}\rangle\right) + 0.1292\left(\lvert\frac{1}{2},-\frac{1}{2}\rangle + \lvert-\frac{1}{2},\frac{1}{2}\rangle\right)$
	0	5		$0.5488\left(\lvert\frac{5}{2},-\frac{5}{2}\rangle + \lvert-\frac{5}{2},\frac{5}{2}\rangle\right) + 0.3670\left(\lvert\frac{3}{2},-\frac{3}{2}\rangle\right.$

			$+\lvert-\frac{3}{2},\frac{3}{2}\rangle\big) + 0.2533\left(\lvert\frac{1}{2},-\frac{1}{2}\rangle + \lvert-\frac{1}{2},\frac{1}{2}\rangle\right)$
1	1		$0.6047\left(\lvert\frac{5}{2},-\frac{3}{2}\rangle + \lvert-\frac{3}{2},\frac{5}{2}\rangle\right)$
			$-0.3531\left(\lvert\frac{3}{2},-\frac{1}{2}\rangle + \lvert-\frac{1}{2},\frac{3}{2}\rangle\right) - 0.1391\lvert\frac{1}{2},-\frac{1}{2}\rangle$
1	2		$0.5420\left(\lvert\frac{5}{2},-\frac{3}{2}\rangle - \lvert-\frac{3}{2},\frac{5}{2}\rangle\right)$
			$-0.4541\left(\lvert\frac{3}{2},-\frac{1}{2}\rangle - \lvert-\frac{1}{2},\frac{3}{2}\rangle\right)$
1	3		$0.2077\left(\lvert\frac{5}{2},-\frac{3}{2}\rangle + \lvert-\frac{3}{2},\frac{5}{2}\rangle\right)$
			$+0.4864\left(\lvert\frac{3}{2},-\frac{1}{2}\rangle + \lvert-\frac{1}{2},\frac{3}{2}\rangle\right) - 0.6638\lvert\frac{1}{2},-\frac{1}{2}\rangle$
1	4		$0.4541\left(\lvert\frac{5}{2},-\frac{3}{2}\rangle - \lvert-\frac{3}{2},\frac{5}{2}\rangle\right)$
			$+0.5420\left(\lvert\frac{3}{2},-\frac{1}{2}\rangle - \lvert-\frac{1}{2},\frac{3}{2}\rangle\right)$
1	5		$0.3021\left(\lvert\frac{5}{2},-\frac{3}{2}\rangle + \lvert-\frac{3}{2},\frac{5}{2}\rangle\right)$
			$+0.3725\left(\lvert\frac{3}{2},-\frac{1}{2}\rangle + \lvert-\frac{1}{2},\frac{3}{2}\rangle\right) + 0.7348\lvert\frac{1}{2},-\frac{1}{2}\rangle$
2	2		$0.0729\left(\lvert\frac{5}{2},-\frac{1}{2}\rangle - \lvert-\frac{1}{2},\frac{5}{2}\rangle\right)$
			$-0.7033\left(\lvert\frac{3}{2},\frac{1}{2}\rangle - \lvert\frac{1}{2},\frac{3}{2}\rangle\right)$
2	3		$0.6932\left(\lvert\frac{5}{2},-\frac{1}{2}\rangle + \lvert-\frac{1}{2},\frac{5}{2}\rangle\right)$
			$-0.1394\left(\lvert\frac{3}{2},\frac{1}{2}\rangle + \lvert\frac{1}{2},\frac{3}{2}\rangle\right)$
2	4		$0.7033\left(\lvert\frac{5}{2},-\frac{1}{2}\rangle - \lvert-\frac{1}{2},\frac{5}{2}\rangle\right)$
			$-0.0729\left(\lvert\frac{3}{2},\frac{1}{2}\rangle - \lvert\frac{1}{2},\frac{3}{2}\rangle\right)$
2	5		$0.1394\left(\lvert\frac{5}{2},-\frac{1}{2}\rangle + \lvert-\frac{1}{2},\frac{5}{2}\rangle\right)$
			$+0.6932\left(\lvert\frac{3}{2},\frac{1}{2}\rangle + \lvert\frac{1}{2},\frac{3}{2}\rangle\right)$
3	3		$0.3677\left(\lvert\frac{5}{2},\frac{1}{2}\rangle + \lvert\frac{1}{2},\frac{5}{2}\rangle\right) - 0.8542\lvert\frac{3}{2},\frac{3}{2}\rangle$
3	4	b	$\left(\lvert\frac{5}{2},\frac{1}{2}\rangle - \lvert\frac{1}{2},\frac{5}{2}\rangle\right)/\sqrt{2}$
3	5		$0.6040\left(\lvert\frac{5}{2},\frac{1}{2}\rangle + \lvert\frac{1}{2},\frac{5}{2}\rangle\right) + 0.5199\lvert\frac{3}{2},\frac{3}{2}\rangle$
4	4	b	$\left(\lvert\frac{5}{2},\frac{3}{2}\rangle - \lvert\frac{3}{2},\frac{5}{2}\rangle\right)/\sqrt{2}$
4	5	b	$\left(\lvert\frac{5}{2},\frac{3}{2}\rangle + \lvert\frac{3}{2},\frac{5}{2}\rangle\right)/\sqrt{2}$
5	5	b	$\lvert\frac{5}{2},\frac{5}{2}\rangle$

Table 3.1: The eigenvectors of the $\hat{H}^{(5)}$ Hamiltonian in terms of the $|M_1, M_2\rangle$ Zeeman substates of the pair states, for the case where the interatomic axis is aligned with the z-axis. It is assumed that $L_1 = L_2$, $S_1 = S_2$ and $J_1 = J_2$. Note a: $C_5 = 0$ for this state. Note b: The state specified in the right-hand column is an eigenstate of $\hat{J}_{\rm t}^2$ as well as of $\hat{H}^{(5)}$.

Of course, the eigenstates of the quadrupole-quadrupole interaction will be

Series	Ω	$\mathcal{J}$	Notes	Eigenvector
$^1S_0$, $^3P_0$	0	0	a,b	$\|0,0\rangle$
$^1P_1$, $^3P_1$,	0	0	a,b	$(\|1,-1\rangle + \|-1,1\rangle - \|0,0\rangle)/\sqrt{3}$
$^3D_1$	0	1	a,b	$(\|1,-1\rangle - \|-1,1\rangle)/\sqrt{2}$
	0	2	b	$(\|1,-1\rangle + \|-1,1\rangle)/\sqrt{6} + \sqrt{2/3}\,\|0,0\rangle$
	1	1	a,b	$(\|1,0\rangle - \|0,1\rangle)/\sqrt{2}$
	1	2	b	$(\|1,0\rangle + \|0,1\rangle)/\sqrt{2}$
	2	2	b	$\|1,1\rangle$
$^1D_2$, $^3P_2$,	0	0		$0.4320\,(\|2,-2\rangle + \|-2,2\rangle)$
$^3D_2$				$-0.5593\,(\|1,-1\rangle + \|-1,1\rangle) + 0.0331\,\|0,0\rangle$
	0	1		$0.3717\,(\|2,-2\rangle - \|-2,2\rangle)$
				$-0.6015\,(\|1,-1\rangle - \|-1,1\rangle)$
	0	2		$0.2064\,(\|2,-2\rangle + \|-2,2\rangle)$
				$+0.1316\,(\|1,-1\rangle + \|-1,1\rangle) - 0.9382\,\|0,0\rangle$
	0	3		$0.6015\,(\|2,-2\rangle - \|-2,2\rangle)$
				$+0.3717\,(\|1,-1\rangle - \|-1,1\rangle)$
	0	4		$0.5204\,(\|2,-2\rangle + \|-2,2\rangle)$
				$+0.4121\,(\|1,-1\rangle + \|-1,1\rangle) + 0.3445\,\|0,0\rangle$
	1	1		$0.6971\,(\|2,-1\rangle - \|-1,2\rangle) + 0.1184\,(\|0,1\rangle - \|1,0\rangle)$
	1	2		$0.6250\,(\|2,-1\rangle + \|-1,2\rangle) - 0.3307\,(\|0,1\rangle + \|1,0\rangle)$
	1	3		$0.1184\,(\|2,-1\rangle - \|-1,2\rangle) + 0.6971\,(\|1,0\rangle - \|0,1\rangle)$
	1	4		$0.3307\,(\|2,-1\rangle + \|-1,2\rangle) + 0.6250\,(\|1,0\rangle + \|0,1\rangle)$
	2	2		$0.2810\,(\|2,0\rangle + \|0,2\rangle) - 0.9177\,\|1,1\rangle$
	2	3	b	$(\|2,0\rangle - \|0,2\rangle)/\sqrt{2}$
	2	4		$0.6489\,(\|2,0\rangle + \|0,2\rangle) + 0.3974\,\|1,1\rangle$
	3	3	b	$(\|1,2\rangle - \|2,1\rangle)/\sqrt{2}$
	3	4	b	$(\|1,2\rangle + \|2,1\rangle)/\sqrt{2}$
	4	4	b	$\|2,2\rangle$

Table 3.2: The eigenvectors of the $\hat{H}^{(5)}$ Hamiltonian in terms of the $|M_1, M_2\rangle$ Zeeman substates of the pair states, for the case where the interatomic axis is aligned with the z-axis. It is assumed that $L_1 = L_2$, $S_1 = S_2$ and $J_1 = J_2$. The eigenvectors listed in this table are the same as those given in Table 1 of Ref. [91]. Note a: $C_5 = 0$ for this state. Note b: The state specified in the right-hand column is an eigenstate of $\hat{J}_t^2$ as well as of $\hat{H}^{(5)}$.

different from the eigenstates of the dipole-dipole interaction. If we take

$$\hat{H}^{(5)} = H_0 + \sum_{i,j} \frac{\mathcal{C}_5^{(ij)}(\hat{R})}{R^5} |M_1^{(i)} M_2^{(i)}\rangle\langle M_1^{(j)} M_2^{(j)}|, \tag{3.21}$$

and

$$\hat{H}^{(6)} = H_0 + \sum_{i,j} \frac{\mathcal{C}_6^{(ij)}(\hat{R})}{R^6} |M_1^{(i)} M_2^{(i)}\rangle\langle M_1^{(j)} M_2^{(j)}|, \tag{3.22}$$

then the eigenstates of both $H^{(5)}$ and $H^{(6)}$ are the ones we characterize by the quantum numbers $\mathcal{J}$ and Ω. The eigenstates of $H^{(5)}$ do not depend on n nor on the atomic species with the same value of J, as only the angular parts of the matrix $\mathcal{C}_5$ affect these eigenstates (note that this is not true for the eigenstates of $H^{(6)}$).

The eigenvectors of $H^{(5)}$ for one- and two-electron atoms are given in tables 3.1 and 3.2 in terms of the values of M_1 and M_2 of the unperturbed eigenstates of H_0. The eigenvectors shown in table 3.1 have not been previously published in full (although some symmetries are presented in [8] for $H^{(6)}$); the eigenvectors in table 3.2 have been presented in [91] as the authors considered one-electron atoms while neglecting spin. The tables show that, for low values of J_1 and J_2, the symmetries are generally fairly simple superpositions of the different values of M_1 and M_2. When the superpositions are compared to those arising from the coupling of J_1 and J_2 (using Clebsch-Gordan coefficients), $\mathcal{J}$ and Ω are found to be good quantum numbers and provide a useful label of the states for values of $J = J_1 = J_2 \leq 1$. At higher values of J_1 and J_2, however, $\mathcal{J}$ becomes less good of a quantum number, and the label is only approximate.

The eigenstates of $H^{(6)}$ are more complicated, as they vary according to the contributions of the intermediate pair states that are summed over in (3.20). This leads to an n- and atom-dependent variation of the eigenvectors. For low values of J, however, similar symmetries are generally found as for the case of the eigenstates of $H^{(5)}$.

Finally, we note that if the quadrupole-quadrupole and dipole-dipole interactions are of similar magnitude for a certain range of values of R, the perturbation is $H' = H^{(5)} + H^{(6)}$ and both interactions must be diagonalized simultaneously.

3.4 Uncertainties

When determining the uncertainties in the calculated values for C_5 and C_6, there are three known sources of error. The first arises from the approximations made in the calculation, mainly from the truncation of the perturbative sum in (3.20) (the full sum over an infinite set of states is unfeasible, as well as unnecessary). The two other sources of error arise from the uncertainties of the atomic energy levels and the calculation of the dipole and quadrupole matrix elements. As the latter also depends on the energy levels, it is clear that the uncertainty in the measurements of the energy levels will play a large role in the total uncertainty.

When considering the truncation of the basis over which we sum in (3.20), it is important to see which states dominate in their contributions to this sum. The contribution of each intermediate pair state of $^1S_0$ symmetry is shown in figure 3.3 for the Sr 5s50p $^1P_1$ state, which are demonstrative of the $^1P_1$ states and has a C_6 of 7.02×10^{19} a.u. for the $\mathcal{J}=2$, $\Omega=0$ state. We see that the contribution to the C_6 coefficient rapidly decreases as the values of n_{1p} and n_{2p} move away from $n_1=n_2=50$. As such, the summation converges very rapidly, and taking a value of $\Delta n=|n_{1p}\pm n|=|n_{2p}\pm n|=10$ is enough to converge the sum to about seven or eight significant figures.

The uncertainty in the dipole and quadrupole matrix elements can be split into two: the uncertainty from the calculation (arising, for example, from the Coulomb approximation), and the uncertainty from the values of the effective principal quantum numbers (derived from energy levels) that are an input to the calculation. We first consider the uncertainty in the calculations of the matrix elements (the uncertainty arising from the energy level uncertainties will shortly be considered as a whole). Unfortunately, the uncertainty contribution from the calculation of the matrix elements is difficult to assess, and can only be estimated by comparing with values calculated using a different method or by comparing to experiment. Using a model potential of the form [22]

$$V_{\text{model}}=-\frac{1}{r}\left[1+(Z-1)e^{-\alpha r}+Bre^{-\beta r}\right], \tag{3.23}$$

where α, β and B are coefficients that are fitted to reproduce experimental

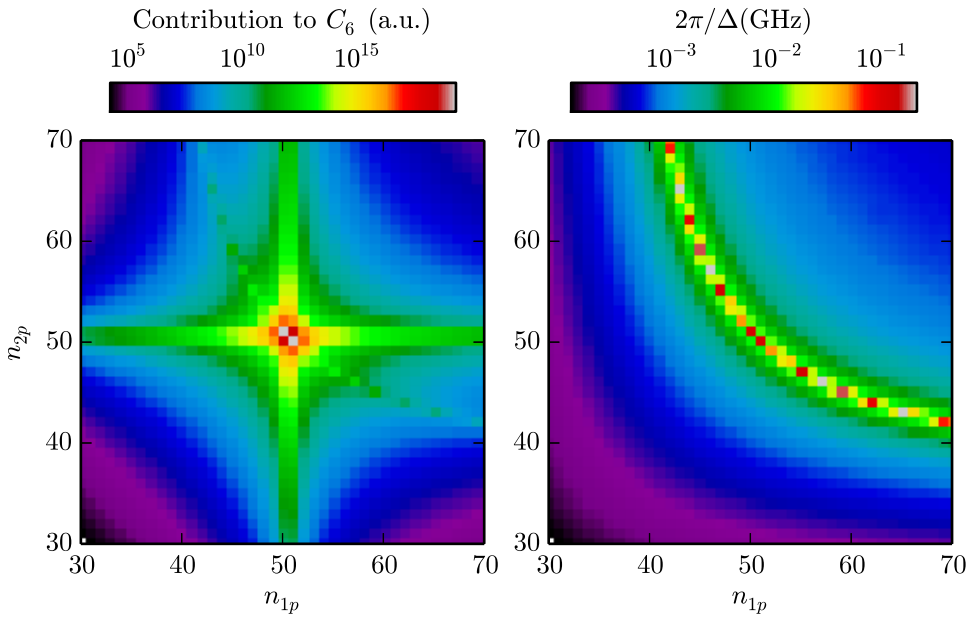

Figure 3.3: Contributions to the total value of C_6 for the Sr 5s50p $^1P_1$ state from individual $^1S_0$ states (left), with the corresponding values for the inverse of the Förster defect (right).

energy levels and Z is the atomic number, we find that the dipole matrix elements calculated using the semiclassical approximation method differ from the ones calculated using the model potential by up to 1% (using the same energy levels as input). The difference between the two calculations reduces with increasing n. The model potential does not include the effect of core polarization, and is therefore likely to be limited in its range of validity, thus contributing significantly to the uncertainty of the matrix elements calculated using this method. Nevertheless, the values of the dipole matrix elements output by the model potential have previously given good results in the calculation of Stark maps [22].

The semiclassical approximation will also have uncertainties from the Coulomb approximation and the WKB approximation, although the uncertainties from both will reduce with increasing n. To check the validity of the semiclassical method it is useful to compare with experimental values of other observables. Extracting the experimental value for the polarizability of the Sr 5s56d $^1D_2$ state from [22], the average value is found to be $\alpha_{\text{exp}} = (2.1 \pm 0.1) \times 10^{12}$ a.u. The average value for the same state calculated

using the semiclassical approximation is $\alpha_{\text{theory}} = 2.06 \times 10^{12}$ a.u. The error from the calculation of the dipole matrix elements can therefore not be more than a few percent for high-n $^1\text{D}_2$ states (the error includes both the error in the matrix elements and the error in the energy level values).

Finally, the error from the energy levels used in the calculation can be assessed more consistently. The uncertainty in the energy levels contributes both to the calculation of the dipole and quadrupole matrix elements, but also in the calculation of the C_6 when determining the Förster defect. The uncertainties in the C_5 and C_6 coefficients are evaluated using the functional method [55], whereby a function depending on a parameter x, $f(x)$, with an uncertainty in the parameter α_x, has an uncertainty in the value of that function given by

$$\alpha_f = |f(x + \alpha_x) - f(x)|. \tag{3.24}$$

For uncorrelated multiparameter functions, the contributions to the uncertainty from each parameter are added in quadrature. Thus, the uncertainties in the matrix elements (3.19) and (3.20) arising from the uncertainties in the energy levels are obtained by using (3.24), with the parameters given by the Rydberg-Ritz fits to the quantum defects (see chapter 1).

The advantages of using the fits to the Rydberg-Ritz equation in tables 2.3 and 2.4 are two-fold: firstly, the random scatter on the experimental energy values are smoothed out, and secondly a wide range of energy levels can be extrapolated from the fits. Concerning the scatter of experimental data points, the small variations in the values cause spurious cancellations in the Förster defects (which can be extremely sensitive to the accuracy of the energy levels). These cancellations lead to unphysical resonances in certain individual states; in general, real Förster resonances (which are resonances due to near-degeneracies of two pair states, usually associated with a change of sign in the C_6 coefficient) can be seen to affect a Rydberg series as a whole, rather than affecting isolated states.

The uncertainties in the C_6 coefficients mirror the uncertainties in the energy levels. Those states that are dipole-coupled to series where the energy levels are known by microwave spectroscopy have uncertainties much lower than 1%; in these cases, the uncertainties due to the dipole matrix elements can be

Atom	Available C_6 coefficients	Available C_5 coefficients
Strontium	$^1S_0$ $^3S_1$ $^1P_1$ $^3P_{0,1,2}$ $^1D_2$ $^3D_{1,2,3}$	$^1P_1$ $^3P_{1,2}$ $^1D_2$ $^3D_{1,2,3}$
Calcium	$^1S_0$ ($^1P_1$) $^3P_1$ ($^1D_2$)	$^1P_1$ $^3P_{1,2}$ ($^1D_2$) $^3D_{1,2}$
Ytterbium	$^1S_0$ $^1P_1$ ($^1D_2$)	$^1P_1$ $^1D_2$

Table 3.3: Index of the coefficients tabulated in the supplementary data of [96]. Results are normally given for $30 \leq n \leq 70$. However, only estimates for a reduced range of principal quantum numbers are given for the series indicated between brackets, due to either a lack of spectroscopic data or the questionability of a single active electron treatment for this calculation.

expected to dominate. In the cases where the dipole-coupled series' energy levels are known only by laser spectroscopy, the uncertainties rise sharply to around 3% to 4%, which is the case for many of the strontium C_6 coefficients. The uncertainties in the C_5 coefficients, however, are generally very low as (3.19) only contains an implicit dependence on a single energy level. The uncertainties in C_5 are thus dominated by the uncertainty in the quadrupole matrix elements calculations.

3.5 Long-Range Interactions

In this section, we discuss the results of the calculations detailed in section 3.2. The results for strontium, calcium and ytterbium are published as supplementary material in reference [96], including the values of C_5, C_6, $\mathcal{C}_5^{ij}$ and $\mathcal{C}_6^{ij}$ for the series listed in table 3.3. Due to high-lying doubly excited states that perturb certain Rydberg series, some of the coefficients (indicated with brackets in table 3.3) provide only an estimate of the interaction strength. In addition, some results for rubidium and caesium will also be presented for comparison. These results have never been published in full, although certain values of the C_6 are presented in [8]; coefficients calculated ignoring spin have been published [91], and other calculations ignoring degeneracies have also been presented [93].

In general, the C_6 coefficients dominate the long-range interactions in the regions where the energy shifts are appreciable. When these energy shifts

become small at large R, the quadrupole-quadrupole interaction begins to dominate. We define the long-range cross-over radius where the dipole-dipole interaction and the quadrupole-quadrupole interaction become equal as $R_{\text{long}} = |C_6/C_5|$.

Some exceptions to the domination of the C_6 over the C_5 coefficients, however, occur when the angular factors are such that one or more eigenstates have a small value of the C_6 coefficient. These eigenstates are known as Förster-zero states [8], and result in the quadrupole-quadrupole interaction dominating. An example of these Förster zero states is given in figure 3.4, where the energy shift at cross-over radius R_{long} is shown for different symmetries of the 5snp ^{1}P$_1$ $\mathcal{J} = 2$ states (the only states for which $C_5 \neq 0$ with ^{1}P$_1$ symmetry). The Förster zero state in figure 3.4 is the $\mathcal{J} = 2$, $\Omega = 1$ state, where the C_6 is small enough that R_{long} occurs at small distances. At these small distances the shift is quite large compared to states that do not have a Förster zero, as seen in figure 3.4.

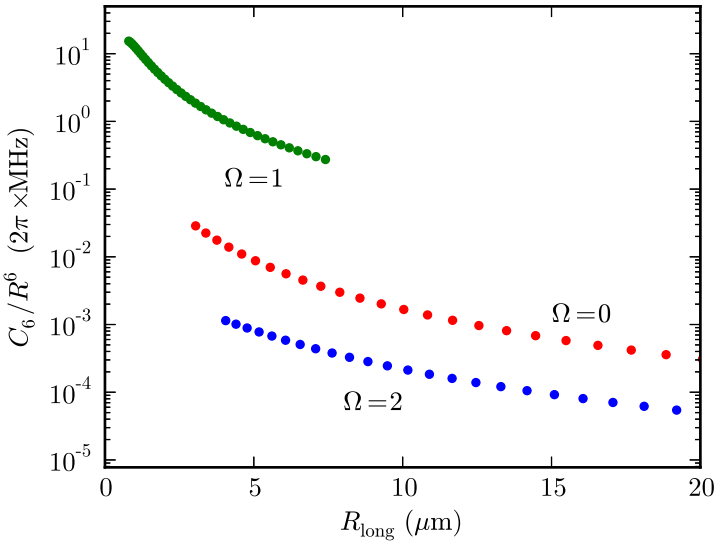

Figure 3.4: The energy shifts due to the dipole-dipole interactions at the radius where $|C_5/R^5| = |C_6/R^6|$, R_{long}, for the 5snp ^{1}P$_1$ $\mathcal{J} = 2$ state of strontium. The value of n runs from 30 to 70 from left to right in the figure.

In the long-range region, the limit of the region where the C_6 coefficient is dominant and applicable is thus given by R_{long}. In the short-range region, however, another limit is reached: the limit where the perturbative expan-

sion becomes invalid. This short-range limit occurs when the energy shift is comparable to the Förster defect of the nearest pair state, Δ_{np}, allowing us to define the short-range limit $R_{\mathrm{short}} = |C_6/\Delta_{\mathrm{np}}|^{1/6}$. Usually, $R_{\mathrm{short}} > R_{\mathrm{LR}}$ (where the LeRoy radius is defined in (3.12)) such that the multipole expansion is still valid.

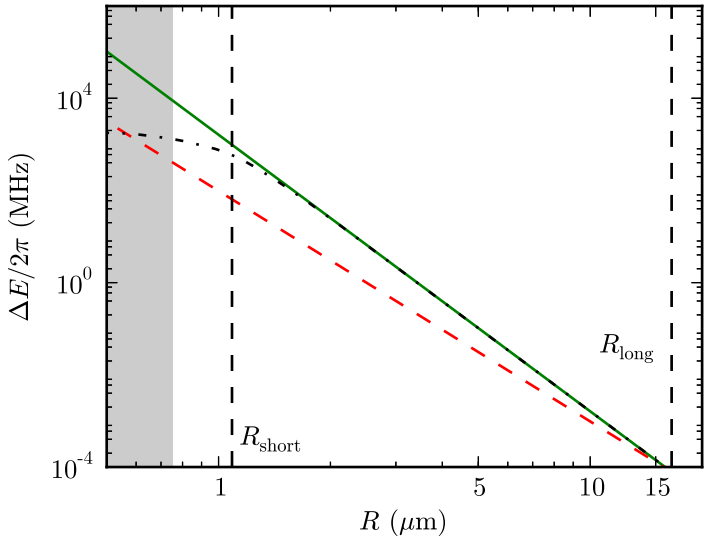

Figure 3.5: A comparison between the perturbative and non-perturbative regimes for the $5sn\mathrm{p}\ {}^1\mathrm{P}_1$ $\mathcal{J} = 2$ state of strontium, as well as the perturbative dipole-dipole and quadrupole-quadrupole calculations. The green solid line denotes C_6/R^6, the red dashed line is the C_5/R^5 and the black dash-dotted line shows the non-perturbative calculation of the dipole-dipole interaction. Vertical black dashed lines denote R_{short} and R_{long}, showing the limits of the validity of the C_6 coefficient. The grey region denotes the region below the LeRoy radius.

Figure 3.5 illustrates the various regimes discussed, with the short- and long-range limits to the validity of the C_6 coefficient marked. Around R_{short}, a clear departure is seen between the perturbative C_6/R^6 calculation and the non-perturbative calculation; in this region the interaction goes from being an R^{-6} form to an R^{-3} interaction [8]. This resonant form of the interaction for short distances constitutes a very small region, as the LeRoy radius is quickly reached below this.

In the rest of this section we discuss the behaviour of the C_5 and C_6 coefficients, and compare the different interactions between the various Rydberg series and atoms. We focus mainly on the behaviour of the C_6 coefficients, as

the C_5 coefficients show much less structure and are usually only valid where the energy shifts due to the interactions are too small to be of experimental interest.

3.5.1 C_5 coefficients

The expression for the C_5 coefficients in (3.19) depends only on the quadrupole matrix elements. The lack of explicit dependence on the energy means that the C_5 coefficients vary very little between Rydberg series, and even between atoms. The coefficients scale as n^8 [91], and the sign can change depending on the symmetry of the state.

The selection rules for the quadrupole matrix elements are [23]

$$\Delta J = 0, \pm 1, \pm 2 \qquad (J + J' \geq 2). \tag{3.25}$$

The result of this selection rule is that all C_5 coefficients for $J < 1$ are zero, regardless of the value of L, meaning that in the alkali metals the $^2\mathrm{S}_{1/2}$ and $^2\mathrm{P}_{1/2}$, and in the alkaline earth metals and ytterbium the $^1\mathrm{S}_0$ states, have no quadrupole-quadrupole interactions to first order. In addition, some symmetries of both the $^1\mathrm{P}_1$ states in the alkaline earth metals and ytterbium, and $^2\mathrm{P}_{3/2}$ states in the alkali metals also have $C_5 = 0$; these quadrupole zero states are marked in tables 3.1 and 3.2.

For states with $L > 1$, the values of the C_5 coefficients corresponding to different symmetries arrange themselves symmetrically about zero for each series. Differences between atoms arise mainly due to the differences in angular momentum quantum numbers, and the C_5 coefficients are otherwise broadly similar. A typical value of C_5 for a given n can be obtained using $C_5 \sim n^8$.

3.5.2 C_6 coefficients

The C_6 coefficients display a much greater variation in their values than the C_5 coefficients. The C_6 coefficients depend on the atomic species, on the value of the principal quantum number n and also on all the angular momentum and spin quantum numbers describing the state.

We begin the discussion of the C_6 coefficients by examining the simplest series, those with $L = 0$. Figure 3.6 shows the scaled C_6 coefficients, meaning the C_6 coefficients with the n^{11} scaling taken out [91, 93], for five different atoms. For rubidium and caesium, the stretched states ($J_1 = J_2 = M_1 = M_2$) are used, although the coefficients for the different symmetries are equal to within the error of the calculation.

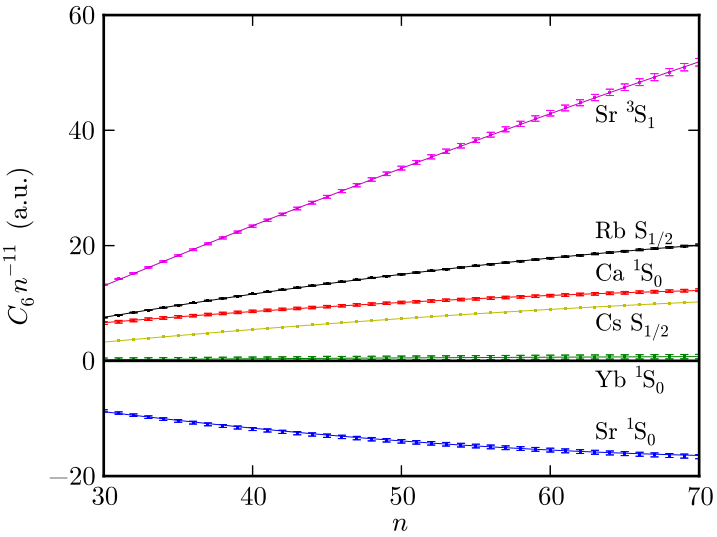

Figure 3.6: Scaled C_6 coefficients for the S states of rubidium, caesium, calcium, strontium and ytterbium. The error bars from the energy level uncertainties for calcium and ytterbium have been multiplied by 200, and those for rubidium by 2000.

The large variation of the coefficients for the $L = 0$ series is apparent in figure 3.6. For the monovalent atoms rubidium and caesium, the dipole-dipole interactions are repulsive for high n, with caesium having weaker interactions. Calcium and ytterbium also have repulsive interactions; however, the dipole-dipole interactions in ytterbium are weaker than the other repulsively interacting atoms by an order of magnitude. The small magnitude of the interactions in ytterbium may have a detrimental effect on the exploitation of the dipole-dipole interactions for various schemes, for example Rydberg dressing an optical lattice clock for the purpose of spin-squeezing [26], or for any schemes seeking to exploit the Rydberg blockade effect.

The most interesting feature of figure 3.6, though, is the attractive interac-

tions of the $^1S_0$ series of strontium. Some proposals such as the preparation of many-body entangled states [12] or non-linear self-focusing schemes [103] make use of attractive interactions. The strontium $^1S_0$ series, however, is the first to exhibit *isotropically* attractive interactions. Based on energy levels from [104–107], we have also estimated the interactions for the $^1S_0$ states of mercury, zinc and magnesium; only zinc was found to have attractive interactions. Figure 3.6 also shows that while the $^1S_0$ states are attractive in strontium, the $^3S_1$ states are strongly repulsive, providing the opportunity for the selection of nearly isotropic attractive or repulsive interactions, depending on the needs of the particular experiment.

Figure 3.7 shows a snapshot of the scaled C_6 coefficients for $n = 50$ (where available) in the divalent atoms. The figure shows a large variation of interactions, ranging from attractive to repulsive interactions. The $^3D_2$, $^3P_2$ and $^3P_1$ series of strontium all show very large interactions, which is due to the action of Förster resonances. Förster resonances are accidental degeneracies between two pair states, where the Förster defect becomes very small in the process of a sign change. The case of the Förster resonance in the $^3P_1$ of strontium is shown in figure 3.8.

As the Förster resonance occurs when the Förster defect is very small, the value of R_{short} will be correspondingly large. Accordingly, the C_6 is a much less useful measure of the dipole-dipole interactions near a Förster resonance as its range of applicability is very limited. In these situations, a non-perturbative calculation is more suited, and usually also reveal the presence of avoided crossings, which can modify the interactions substantially and even lead to the formation of long-range molecules [108]. Förster resonances can also lead to state transfer due to the strong coupling and small energy separation between pair states; this state transfer can also be observed in the absence of a natural Förster resonance by applying an electric or magnetic field [109, 110]. We will explore the uses of Förster resonances in more detail in chapter 5.

Figure 3.9 shows a snapshot of the C_6 coefficients at $n = 50$ for rubidium and caesium. Förster resonances are found in the $P_{3/2}$, $D_{3/2}$ and $D_{5/2}$ series of rubidium, and in the $P_{3/2}$ series of caesium.

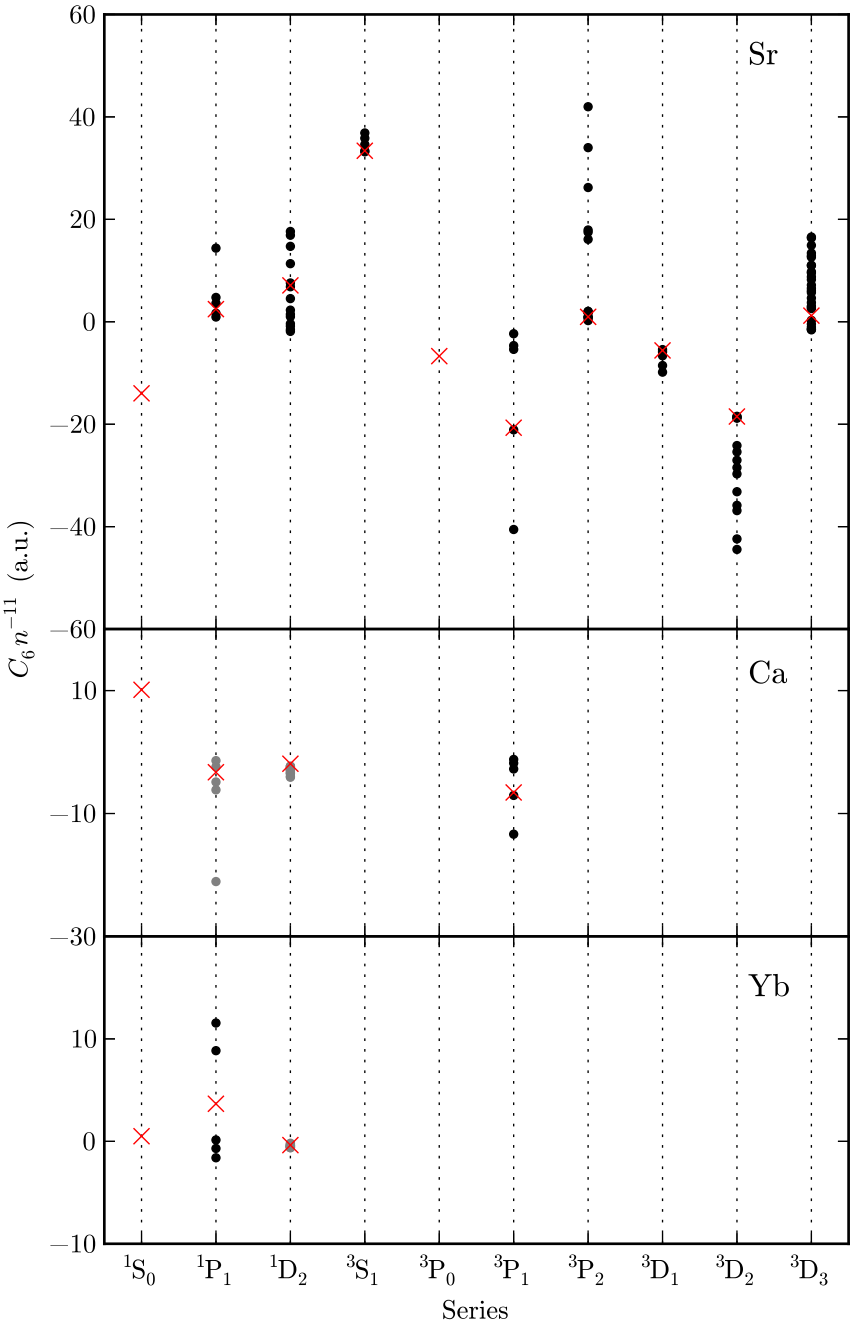

Figure 3.7: Scaled C_6 coefficients for different states of calcium, strontium and ytterbium at $n = 50$. Red crosses denote the stretched state, $J = M$, for the corresponding symmetry, and grey markers denote estimated scaled coefficients at $n = 40$ for states that do not have sufficient data for a full systematic calculation over the whole series.

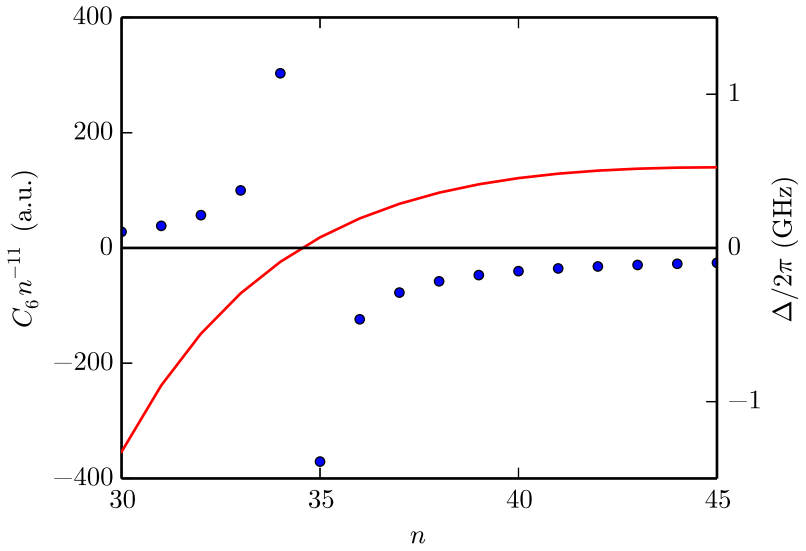

Figure 3.8: Scaled C_6 coefficients (blue circles) and the Förster defect (red line) as a function of n for the 5snp ^{3}P$_1$ $\mathcal{J} = 2$ $\Omega = 2$ state of strontium.

As very few experimental values of the C_6 coefficients have been published for Rydberg atoms, it is difficult to make comparisons. Some published values, however, have recently appeared for the $D_{3/2}$ states of rubidium [111]. The numerical comparisons between the various calculated and observed C_6 coefficients are shown in table 3.4. The theoretical values calculated in this work and in [111] agree very well with each other, but the experimental values lie below the theoretical values (this is not commented on in [111]). The experimental values are derived from fits to experimental data points, and the experimental data points of the measured shift as a function of R are seen to deviate for small values of R. One reason for this discrepancy is may be the measurements being performed at $R < R_{\text{short}}$ and modifying the potential to R^{-3} (the points shown in [111] show a departure from the R^{-6} dependence). The values for R_{short}, however, are much smaller than the values of R where the points in [111] were measured; the authors of the paper suggest mechanical effects may underly this discrepancy [112]. Other possible explanations for the discrepancies include the presence of stray electric or magnetic fields, or a slight ellipticity in the polarization of the excitation lasers. Both of these effects would mix in other eigenstates, such that the interactions would be an average over several values of C_6/R^6. As the points

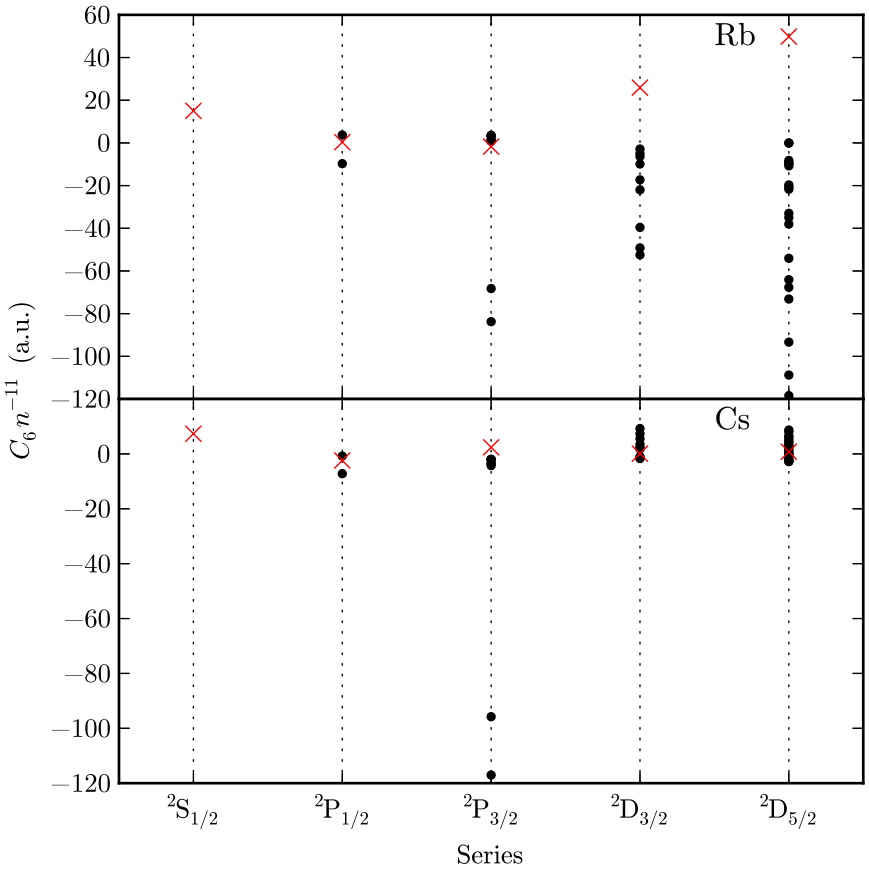

Figure 3.9: Scaled C_6 coefficients for different states of rubidium and caesium at $n = 50$. Red crosses denote the stretched state, $J = M$, for the corresponding symmetry.

showing the departure from the R^{-6} dependence were included in the fit for C_6, the experimental values of C_6 will be artificially lowered, resulting in the discrepancy seen in table 3.4. The uncertainties in the theoretical values of [111] are calculated by putting random perturbations in the dipole matrix elements leading to the numerically calculated energy shifts and refitting the C_6 coefficients. Uncertainties in the present values will be similar to those calculated in [111], as they are dominated by the uncertainties in the dipole matrix elements.

Finally, we note the relative magnitude of the error bars between the divalent atoms and the alkali metals are substantially different, as the energy levels of the alkali metals are usually known to much better precision and accuracy for a wider range of series. For these, the error contributed from the energy

n	Calculated [111]	Calculated (present work)	Observed [111]
53	16.9(1.7)	16.6	13.7(1.2)
62	766(15)	766	730(20)
82	8870(150)	8864	8500(300)

Table 3.4: Comparison between calculated and observed values of the C_6 coefficients for the stretched ($J = M_J$) $2 \times n^2\mathrm{D}_{3/2}$ states of rubidium. All values are in GHz μm^6, where 1 GHz μm$^6 = 1.4448 \times 10^{-19}$ a.u.

levels will be negligible compared to the error from the dipole matrix element calculations, which is not the case for strontium.

3.6 Angular Dependence

Thus far we have treated only the case where the angle between the internuclear axis and the z-axis, θ, is zero. In this section we discuss the effect of a finite value for this angle.

For $\theta \neq 0$, the C_6 for the eigenstates will remain the same (recall that a rotation is a unitary transformation). The eigenvectors, however, will vary as a function of θ, meaning that the superposition of the different values of M_1 and M_2 will change. If the polarization of the laser that initially excites the atoms to the Rydberg state is well controlled, then the process of exciting to a well defined value of M_1 and M_2 implies that a superposition of different eigenstates will be set up. As the different energy eigenstates are not degenerate for finite R, this means that the state of the atoms will oscillate between the different eigenstates. In order to describe this situation, we describe the variation of the interaction with angle θ in terms of the expectation value of the C_6 interaction, denoted as $\langle C_6 \rangle = \sum_i C_6^{(i)} |c_i(\theta)|^2$ where i is the eigenstate label, $C_6^{(i)}$ is the C_6 coefficient for a particular eigenstate of the full Hamiltonian in (3.1), and c_i is the state fraction for the eigenstate in the superposition.

The angular variation is determined not only by the angular momentum quantum numbers of the state, but also by the strength of the coupling to the intermediate states and the quantum numbers of the intermediate state.

Without needing to sum over the intermediate states, the angular variation would be determined by the Wigner rotation matrices [40]. Instead, we just vary θ in the angular matrix element of the multipole interaction (see appendix A), and sum over all intermediate states, not just states where $|\Omega|$ is conserved. Consequently, the angular variation of the interactions are state- and atom-dependent.

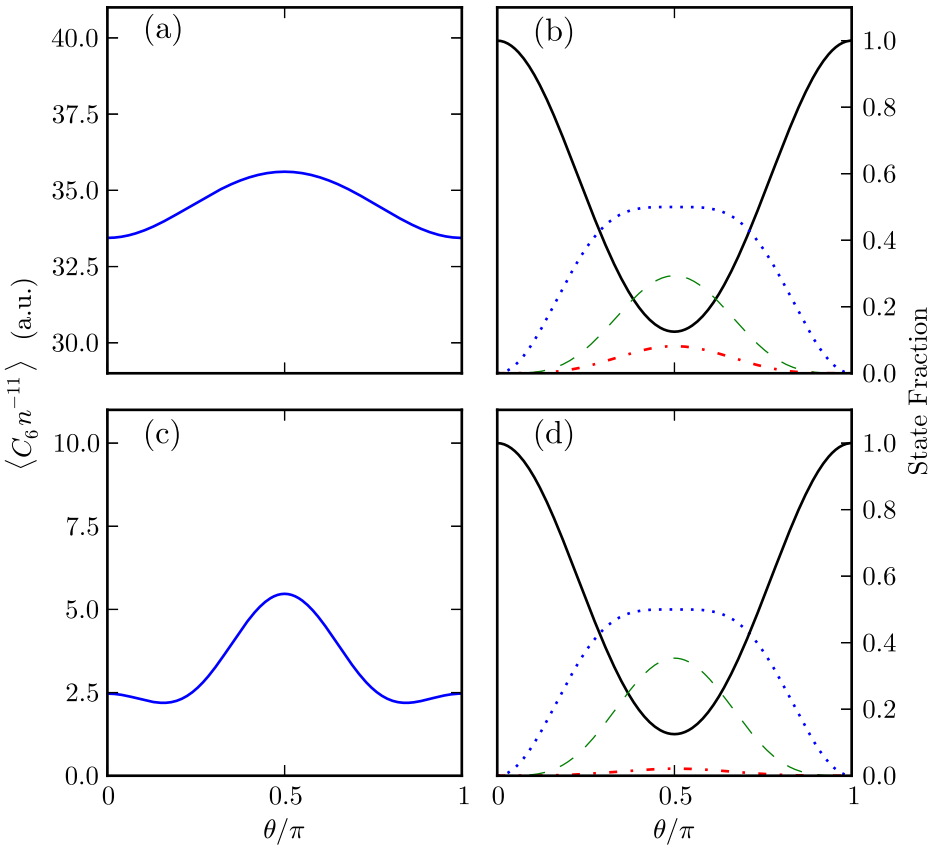

Figure 3.10: Angular variation of the expectation value of the scaled C_6 coefficient for the $^3S_1$ (a) and $^1P_1$ (c) of strontium. The state compositions in terms of energy eigenstates for the $M_1 = M_2 = 1$ states of the $^3S_1$ and $^1P_1$ are also shown in panels (b) and (d) respectively. The lines in (b) and (d) are: $\mathcal{J} = 0\ \Omega = 0$ (red dash-dotted), $\mathcal{J} = 2\ \Omega = 0$ (green dashed), $\mathcal{J} = 2\ \Omega = 1 + \mathcal{J} = 2\ \Omega = -1$ (blue dotted), and $\mathcal{J} = 2\ \Omega = 2 + \mathcal{J} = 2\ \Omega = -2$ (black solid).

Figure 3.10 shows the angular variation of the $^1P_1$ and $^3S_1$ of strontium. The cases of the $^1P_1$ and $^3S_1$ states are particularly interesting as all of the total angular momentum is contributed either from orbital angular momentum or spin angular momentum. The variation between the magnitude of C_6 for

different eigenstates leads to the angular dependence of the expectation value of C_6; as the $^1P_1$ states show a greater difference between the different values of C_6 compared to the $^3S_1$ states, the angular variation of the expectation value is correspondingly greater. This is to be expected, as the differences between the C_6 values in the $^3S_1$ states are due to spin-orbit coupling, which has been shown to be small for strontium Rydberg states [113]. The angular variation for the $^3S_1$ states arise entirely from the fine structure splittings of the ^3P states.

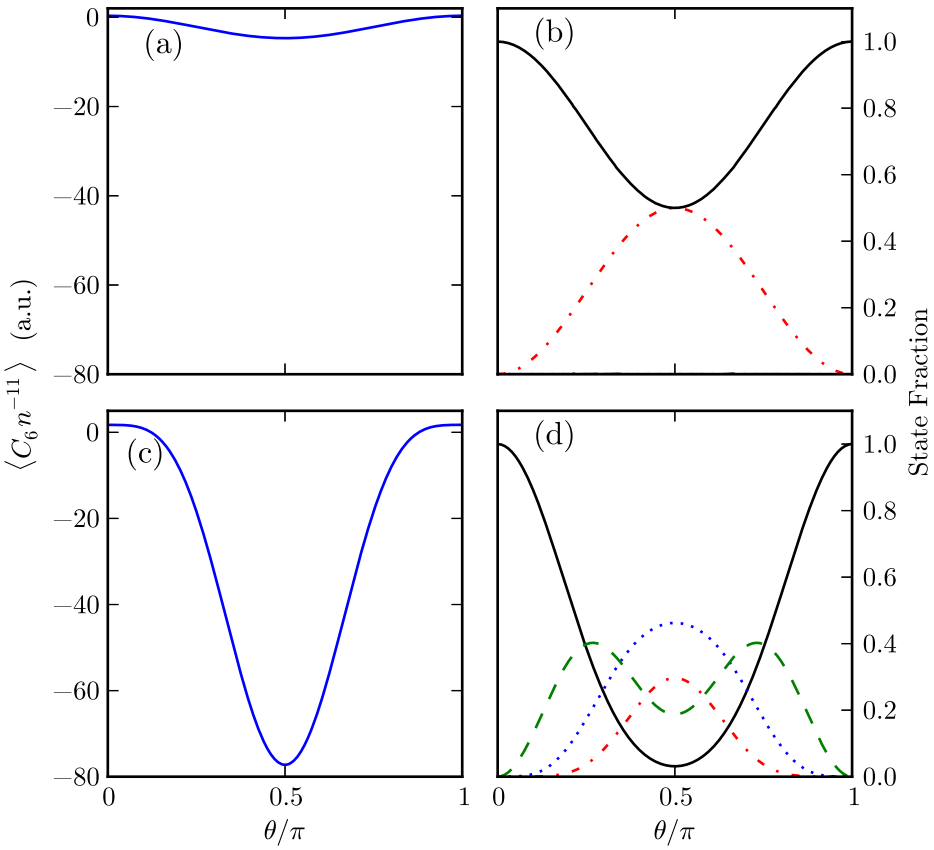

Figure 3.11: Angular variation of the expectation value of the scaled C_6 coefficient for the $^2P_{1/2}$ (a) and $^2P_{3/2}$ (c) of rubidium. The state compositions in terms of energy eigenstates for the stretched states of the $^2P_{1/2}$ (b) and $^2P_{3/2}$ (d) are also shown. The lines in (b) are: $\mathcal{J} = 1\ \Omega = 0$ (red dash-dotted), and $\mathcal{J} = 1\ \Omega = 1$ (black solid). The lines in (d) are: $\mathcal{J} = 3\ \Omega = 0$ (red dash-dotted), $\mathcal{J} = 3\ \Omega = 2 + \mathcal{J} = 3\ \Omega = -2$ (green dashed), $\mathcal{J} = 3\ \Omega = 1 + \mathcal{J} = 3\ \Omega = -1$ (blue dotted), and $\mathcal{J} = 3\ \Omega = 3 + \mathcal{J} = 3\ \Omega = -2$ (black solid). The admixture of the $\mathcal{J} \neq 3$ states is not shown in the bottom right hand plot, but is very small.

The angular variation in the strontium states can be compared to similar states in rubidium; the $^2P_{1/2}$ and $^2P_{3/2}$ states of rubidium are shown in figure 3.11 (the $^2S_{1/2}$ have no variation to within the error of the calculation). There are two notable features of the expectation values, the first being the zero crossings visible in both fine structure components of the P states. It should be noted that as these are expectation values, the zero-crossings do not imply zero interaction at the crossing. Instead, the wavefunction for each atom pair (which is a superposition of the eigenstates) will collapse to one value of the C_6 coefficient corresponding to a particular eigenstate. Over a statistical ensemble, however, the interaction would average to zero. The zero crossings occur because the different values of the C_6 coefficients have opposite signs for different eigenstates, therefore not every symmetry or atom will have a similar zero crossing. The second noteworthy feature of figure 3.11 is the very large angular variation of the $^2P_{3/2}$ states. This is due to the Förster resonance discussed in section 3.5.2.

The eigenvectors in figure 3.11 reflect the changing projection of the $\mathcal{J} = 3$ as the z-axis is rotated with respect to the internuclear axis. Some $\mathcal{J} = 1$ states (not shown in figure 3.11) also contribute very small amounts to the expectation value, which is due to the small mixing present between $\mathcal{J}$ states. The mixing between $\mathcal{J}$ states increases with increasing angular momenta J_1 and J_2, for all atoms.

In the absence of an external field, the angular variation has no impact on the C_6 as long as the initial states of the atoms are well controlled. If, however, the atoms are interacting during the excitation process, or if there is an external field applied, the angular variation will lead to a superposition of different eigenstates, implying that the different values of the C_6 will need to be averaged over the statistical ensemble of atoms. For some Rydberg states (such as those with $L = 0$), the angular variation can be ignored, however for others (particularly ones with Förster resonant intermediate states) the angular variation must be taken into account.

3.7 Conclusions

In this chapter we have given an overview of the theory of long-range interactions in Rydberg atoms. In so doing, we have given details of the interaction potential and derived the multipolar expansion used in the calculations presented. The energy shifts associated with the long-range interactions were treated with both perturbative and non-perturbative methods. We have seen that the non-perturbative methods give a more accurate view of the interaction, valid over a wider range of internuclear distances. The perturbative methods, however, allowed a comparison between many states and even between several atoms.

Focusing on the perturbative calculations, degenerate perturbation theory needed to be applied in the absence of an external field. We focused on the dipole-dipole and quadrupole-quadrupole interactions, deriving the corresponding C_6 and C_5 coefficients respectively, where C_5/R^5 and C_6/R^6 are the leading order interaction terms between two atoms initially in the same Rydberg state. We also discussed the uncertainties involved in these calculations, including mainly the uncertainties due to the energy levels, as well as the convergence of the calculations with the number of basis states included when calculating C_6 coefficients.

The eigenstates of the dipole-dipole and quadrupole-quadrupole interactions were also discussed, as these are in general linear combinations of the pair states that are degenerate in M_1 and M_2, the projections of the total angular momentum of each atom onto the z-axis, at infinite internuclear separation. We have shown that the eigenstates approximately correspond to states where the total angular momentum of each atom combine to form a total angular momentum of the atom pair, $\mathcal{J}$, with its projection onto the internuclear axis Ω.

The perturbative and non-perturbative calculations were compared for the dipole-dipole interaction, and the comparison used to put limits on the validity of the C_6 in the case of small internuclear separations. The limits on the validity of the C_6 coefficients were also obtained by comparing the dominance of the dipole-dipole interaction over the quadrupole-quadrupole interactions; the latter become dominant at very large internuclear separation.

A large number of C_6 coefficients were calculated and compared across different series and atoms. Particular attention was paid to the $L = 0$ states, where strontium was found to have isotropically attractive interactions that have applications in many-body entangled states [12] and linear self-focusing schemes [103]. In other series, several Förster resonances were found, which correspond to near degeneracies between the pair states of interest and energetically close-lying dipole-coupled pair states.

Finally, we investigated the effects of varying the angle between the z-axis and the internuclear axis. The main effect of the angular variation is to mix M_1 and M_2 states differently, or conversely, mixing Ω states if one starts in states with well defined values of M_1 and M_2.

The calculations of the dipole-dipole and quadrupole-quadrupole interactions in the divalent atoms presented here are published in [96]. The values of the C_5 and C_6 coefficients for rubidium and caesium have been partially discussed in [8, 91, 93] and others, but have not been presented in a unified treatment until now.

Chapter 4

Multichannel Quantum Defect Theory

4.1 Introduction

Thus far all the calculations presented have used a one-active electron model. This one-electron treatment has successfully been applied to calculations of strontium Rydberg properties in the past [22, 114]; however, the limitations of the application of such a one-electron model to two-electron atoms has never been investigated, to the best of our knowledge. To go beyond the simple one-electron description we must first take a step back and develop the theory of two-electron Rydberg atoms.

The main effect that arises in two-electron atoms that causes a departure from the typical one-electron Rydberg atom behaviour is the presence of doubly excited states [2]. The overwhelming majority of these doubly excited states are autoionizing, meaning that they are quasi-bound states over the ionization limit and hence ionize rapidly rather than decaying back to a lower excited state. A few of the lowest-lying doubly excited states, however, are below the ionization threshold; when these coincide in total angular momentum and parity with singly excited states nearby in energy, these doubly excited states can cause energy shifts known as perturbations [30]. Additionally, perturbations affect the wavefunctions of the bound states by mixing in some of the doubly excited state wavefunctions, causing large departures in

the expected behaviour of the Rydberg properties such as the radiative lifetimes [30]. A consequence of these perturbed wavefunctions is the presence of transitions that are normally dipole-disallowed; these intercombination lines find many uses, for example as clock transitions [115], or generating spin-squeezed states [26].

There are many ways to calculate two-electron effects, most of which involve *ab initio* calculations where correlations between the electrons are treated to various orders, using large basis sets and a variational procedure; examples include multiconfiguration Hartree-Fock (MCHF) calculations [116], R-matrix calculations [117] or density functional theory [118]. These methods, however, are extremely complex, often with computer codes that can be prohibitively complicated to use and adapt (see for example [119]). An alternative is an empirical method known as multichannel quantum defect theory (MQDT); this is an extension of the (single channel) quantum defect theory that has already been mentioned in chapter 2. This can, and has, been used extensively, both as an empirical method and in combination with R-matrix methods to produce an *ab initio* calculation [19, 30].

MQDT has been used extensively in the description of two-electron effects in the alkaline earth metals [19, 30, 120]. However, the empirical and *ab initio* methods present different advantages and disadvantages. In the empirical method, the required parameters are fitted to reproduce experimental energy levels, whereas the *ab initio* method calculates these parameters based on a model potential of the singly-ionized ion, combined with the R-matrix method. The empirical method allows a detailed analysis of the Rydberg spectrum of the atom, with the energy levels reproduced to within the accuracy of the measurements. The information gained from the empirical method, however, is incomplete and relies heavily on previous spectroscopic work. Additionally, the complexity of certain series (for example the D_2 series of strontium) requires a large number of parameters, which greatly complicates the fitting procedure when no previous models are available. Many of the issues present in the empirical method are resolved using *ab initio* methods, as the categorization of the perturbing states is unambiguous, and the parameters that are generated do not rely on previous data [30]. These *ab initio* methods, however, have never reached spectroscopic accuracy (at least

not in any published results). The discrepancies between experiment and *ab initio* values of energy levels are usually small compared to the binding energy; we note, however, that small deviations in the energy can occasionally result in large changes to MQDT predictions.

In this chapter, we build on previous empirical and *ab initio* models of strontium, and re-investigate the Rydberg series with the empirical method using data that has been measured to much higher accuracy and precision. As the new energy levels (published after the original empirical models [61, 120] of strontium) have much smaller uncertainties, the new MQDT models are much more tightly constrained, allowing us to update the view of the competing couplings between various two-electron configurations of the bound states of strontium. For certain series the data have not been updated; MQDT models developed to describe these data, however, have been of poor quality, with large deviations between the energy level values outputted by the MQDT models and those measured experimentally.

The detailed analysis of the two-electron effects also allow us to extend the calculation to investigate the radiative properties of the Rydberg states. Using numerical wavefunctions calculated using the methods described in section 2.4.1 in conjunction with the channel fractions (which are essentially the state coefficients in an expansion of the full wavefunction), two-electron effects can be included in the calculation of dipole matrix elements and hence in the calculation of radiative lifetimes and oscillator strengths. The calculations of the lifetimes allows the analysis of the effect of perturbers on the physical properties of Rydberg states, and will pave the way for calculations of long-range interactions in two-electron atoms.

This chapter begins with a review of MQDT, including the determination of bound state energies and their wavefunctions using the parameters derived from the theory. We go on to apply the theory to the Rydberg states of strontium, and systematically develop MQDT models for each Rydberg series where the energy levels are known; these models are found to agree very well with experiment and with previous *ab initio* work (with some notable exceptions). Finally, we use these models to numerically calculate radiative lifetimes of the Rydberg states, providing a firm foundation from which we

can go on to include two-electron effects in the calculation of long-range interactions.

4.2 MQDT Formulation

4.2.1 Reactance Matrix Approach

In MQDT, a single-active electron interacts with the atomic core through an effective interaction potential that depends on the state of the core. Different configurations of the combined system comprising of the core and the active electron are known as channels, and channels that coincide in parity and total angular momentum can couple together [30, 34, 121]. This coupling between channels is what gives rise to the admixture of doubly excited configurations in singly excited Rydberg states, hence the determination of the coupling strength of the channels is crucial to the description of two-electron effects in Rydberg states. The properties of Rydberg states are mostly determined by the Coulomb tail of the effective interaction potential between the active electron and the core. For large radial distances, r, the radial wavefunction of the active electron in a channel labelled i is given by $\phi_i(r)$, which satisfies the Coulomb equation [45]

$$\left[-\frac{d^2}{dr^2} + \frac{l_i(l_i+1)}{r^2} + \frac{2\mu}{r}\right]\phi_i = 2\mu\epsilon_i\phi_i, \tag{4.1}$$

where μ is the reduced mass of the system, l_i is the orbital angular momentum of the active electron in channel i and ϵ_i is the energy of the active electron in that channel. The total energy of the state, expressed in wave numbers, is given by

$$E = I_i + \frac{\epsilon_i}{hc}, \tag{4.2}$$

where I_i is the ionization threshold of channel i, h is Planck's constant and c is the speed of light.

The solution to (4.1) can be written as a linear combination of the regular and irregular Coulomb functions s and c [34, 45], such that

$$\phi_i(r) = \left[s(l_i, \epsilon_i, r)\cos\theta_i + c(l_i, \epsilon_i, r)\sin\theta_i\right], \quad r \gg a_0. \tag{4.3}$$

Here, $\theta_i = \pi\nu_i = \pi(n-\delta_i)$ is the admixture between the regular and irregular functions, and can be written in terms of an effective principal quantum number for channel i, ν_i. This in turn can be written in terms of a channel quantum defect, δ_i, which generally has a small energy dependence due to core polarization.

The atomic eigenfunction, Ψ, can be written as a general superposition of the channel wavefunctions, such that [34]

$$\Psi = \mathcal{A}\sum_i A_i\phi_i\chi_i, \tag{4.4}$$

where A_i are channel coefficients, χ_i contain angular and spin terms for the active electron and $\mathcal{A}$ signifies that the sum must be anti-symmetrized. We note that we refer to A_i^2 as channel fractions, and these coefficients determine the level of admixture of each channel in a bound state; the channel fractions depend on the total energy. The index i runs over the N channels included in the model.

While the bulk of the Rydberg wavefunction is determined by the Coulomb tail of the effective interaction potential, the phase-shift θ_i and the interchannel couplings entirely arise due to the short-range interactions between the active electron and the core electrons. It is therefore possible to write the total wavefunction Ψ in terms of the N uncoupled eigenfunctions of these short-range interactions (which we call short-range channels), ψ_α, where α is the index of the uncoupled eigenfunction, such that

$$\Psi = \sum_\alpha B_\alpha\psi_\alpha. \tag{4.5}$$

The B_α coefficients are similar to the A_i coefficients, but give the short-range channel admixtures. This uncoupled basis is related to the long-range channels in (4.3) by a unitary transformation, which, for sufficiently large r, should be almost energy independent. We can thus write

$$\psi_\alpha = \left(\mathcal{A}\sum_i U_{i\alpha}s(l_i,\epsilon_i,r)\chi_i\right)\cos(\pi\mu_\alpha) - \left(\mathcal{A}\sum_i U_{i\alpha}c(l_i,\epsilon_i,r)\chi_i\right)\sin(\pi\mu_\alpha), \tag{4.6}$$

where the $U_{i\alpha}$ are coefficients of a real unitary matrix, $\mathbf{U}$, describing the transformation between the long-range channels, ϕ_i, and the short range uncoupled channels, ψ_α.

We now combine equations (4.3), (4.4), (4.5) and (4.6), and equate the coefficients of $s(l_i, \epsilon_i, r)\chi_i$ and $c(l_i, \epsilon_i, r)\chi_i$ to obtain

$$A_i e^{-i\pi\nu_i} = \sum_\alpha U_{i\alpha} B_\alpha e^{i\pi\mu_\alpha} \tag{4.7a}$$

$$B_\alpha e^{i\pi\mu_\alpha} = \sum_i U_{i\alpha} A_i e^{-i\pi\nu_i}. \tag{4.7b}$$

We note that to obtain (4.7) we have split the sine and cosine terms into complex exponentials. By requiring the A_i and B_α coefficients to be real, 4.7b can be split into real and imaginary parts, leading to the condition

$$\sum_i U_{i\alpha} A_i \sin[\pi(\nu_i + \mu_\alpha)] = 0, \quad \alpha = 1, \ldots, N. \tag{4.8}$$

The condition (4.8) only has non-trivial solutions if

$$\det |U_{i\alpha} \sin[\pi(\nu_i + \mu_\alpha)]| = 0. \tag{4.9}$$

This determinant condition sets the basis for the MQDT calculation, as (4.9) places a constraint on the possible values of the effective principal quantum numbers. This form of the determinant equation has been widely used in empirical MQDT modelling of the alkaline earths [19, 61, 97, 120]. Typically, the **U** matrix is factorized into products of rotation matrices, which allows the parametrization of interchannel couplings using mixing angles [19]. We note, however, that the factorization of **U** is not unique, as the order of the rotations is important. Additionally, the presence of the sine function in (4.9) is less favourable for numerical algorithms. We can reformulate the condition (4.9) by rewriting the equation in the form

$$\cos(\pi\mu_\alpha) \sum_i [U_{i\alpha} \tan(\pi\nu_i) + \tan(\pi\mu_\alpha) U_{i\alpha}] \cos(\pi\nu_i) A_i = 0. \tag{4.10}$$

This can then be written as

$$\sum_i [K_{i\alpha} + \delta_{i\alpha} \tan(\pi\nu_i)]\, a_i = 0, \tag{4.11}$$

where $a_i = A_i \cos(\pi\nu_i)$ and $K_{i\alpha}$ are the elements of the reactance matrix, **K**, defined as

$$\mathbf{K} = \mathbf{U}^\dagger \mathrm{diag}[\tan(\pi\mu_\alpha)]\mathbf{U}, \tag{4.12}$$

where diag[tan($\pi\mu_\alpha$)] denotes a diagonal matrix with matrix elements $\delta_{i\alpha}\tan(\pi\mu_\alpha)$. The determinant condition for a non-trivial solution of (4.11) is given by

$$\det|K_{i\alpha} + \delta_{i\alpha}\tan(\pi\nu_i)| = 0. \tag{4.13}$$

Using the **K** matrix, the values of the effective principal quantum numbers, ν_i, are constrained. Until now, however, we have not imposed the final boundary condition that $\Psi \to 0$ as $r \to \infty$. Imposing this boundary condition introduces the additional constraint

$$E = I_i - \frac{\tilde{R}}{\nu_i^2}, \quad i = 1, \ldots, N, \tag{4.14}$$

where $\tilde{R} = \alpha^2 cMm_e[2h(m_e+M)]^{-1}$ (where m_e is the electron mass and M is the total atomic mass) is the mass-corrected Rydberg constant and I_i denotes the ionization threshold for channel i. A bound state is found at values of ν_i where both conditions (4.13) and (4.14) are simultaneously satisfied for a given **K** matrix.

Finally, the effect of core-polarization on the active electron causes energy dependences in the **K** matrix [34]. Often, these energy dependences are small enough that they can be ignored, although this is not true in general. In order to account for these energy dependences, we introduce a linear energy-dependent term to the diagonal elements of **K**,

$$K_{ii}(E) = K_{ii}^{(0)} + K_{ii}^{(1)}\frac{(I_s - E)}{I_s}. \tag{4.15}$$

This linear term is similar to the second term in a Rydberg-Ritz expansion of quantum defects; the introduction of this term produces linear energy dependences in the eigenquantum defects, μ_α, to the energy dependences of quantum defects in the single-channel quantum defect theory.

MQDT models can be developed in one of the two ways mentioned in section 4.1: empirically or *ab initio*. In *ab initio* models the **K** matrix is calculated using R-matrix methods in combination with a model potential for the singly ionized ion [30]. Empirical models, such as the ones presented in section 4.3, obtain the **K** matrix by fitting the matrix such that the bound state energies predicted by the MQDT model coincides with the experimentally measured bound state energies. In this work we develop empirical models for strontium Rydberg states.

4.2.2 Bound State Energies and Empirical K Matrices

Constructing and extracting channel fractions from an MQDT model requires the extraction of bound state energies for a given **K** matrix. Bound states occur at values of ν_i where equations (4.13) and (4.14) are simultaneously satisfied. We note that, for a given **K** matrix, at a bound state the effective principal quantum numbers of all channels are unique and coincide for equations (4.13) and (4.14); in between bound states, however, the two equations predict different combinations of ν_i values (for models with more than two channels). As such, it is important to ensure that the choice of ν_i values used when obtaining the **K** is consistent. The method detailed below ensures a self-consistent set of bound state energies for every value of **K**, allowing a fitting procedure to obtain empirical MQDT models.

We start by choosing the effective principal quantum number of two channels. The first, labelled ν_j, is used as the independent variable (related to the total energy). The second, labelled ν_k, we use as the channel in which we search for bound states. The choice of channels is arbitrary, and changing this choice gives the same results. Using this choice, we rewrite equation (4.14) such that other values of ν_i (excluding ν_k) can be formulated in terms of ν_j, leading to

$$F_i(\nu_j) = \left[\frac{I_i - I_j}{\tilde{R}} + \frac{1}{\nu_j^2}\right]^{-1/2}. \tag{4.16}$$

The values of ν_i are then

$$\nu_i = F_i(\nu_j), \qquad i \neq k. \tag{4.17}$$

Equations (4.16) and (4.17) ensure that all values of ν_i other than ν_k are unambiguously fixed before applying the determinant condition in (4.13).

In order to apply the determinant condition in (4.13), we define a function $G_k(\mathbf{K}; \nu_j)$ that is a rearrangement of (4.13) such that $\nu_k = G_k(\mathbf{K}; \nu_j)$. The specific form of $G_k(\mathbf{K}; \nu_j)$ depends on the number of channels and also on the choice of which matrix elements of $K_{i\alpha}$ to set to zero in order to reduce the number of fitting parameters (the zeros are usually chosen such that two perturbing channels do not couple). For example, a two-channel model with

a non-zero coupling parameter $K_{12} = K_{21}$ results in

$$\nu_1 = G(\nu_2) = \frac{1}{\pi}\tan^{-1}\left(\frac{K_{12}^2}{K_{22} + \tan \pi\nu_2}\right) - K_{11}. \tag{4.18}$$

As the bound state energy positions are determined when (4.13) and (4.14) coincide, we can write a function $\Xi(\nu_j)$ that depends only on ν_j (which itself can be written in terms of energy using (4.14)) such that

$$\Xi(\nu_j) = G_k([K_{i\alpha}]; \nu_j) - F_k(\nu_j). \tag{4.19}$$

The bound state energies are then determined by zero crossings of the function $\Xi(\nu_j)$. Numerically, we find it advantageous to find the minimum of the function $\Xi(\nu_j)^2$ instead of finding the roots of $\Xi(\nu_j)$, as the tangent functions in $\Xi(\nu_j)$ has repeating poles which can be interpreted by numerical root-finding algorithms as a zero-crossing. We use a Brent's method numerical algorithm to find the minima of the $\Xi(\nu_j)^2$ function [122], with the experimental value of ν_j used as an initial guess, with the upper and lower boundaries a suitable fixed value above and below the initial guess respectively. Initial guesses for n values greater than what is experimentally available can be extrapolated using the fits to the Rydberg-Ritz equation given in table 2.4.

A given **K** matrix will produce a series of energy levels that can be extracted using the above method. In order to find an empirical MQDT model, a least-squares fitting procedure can be used to minimize the difference between the energy levels predicted by a **K** matrix and the experimentally measured energy levels, while taking into account the uncertainties [55]. The cost function, χ^2, is given by

$$\chi^2 = \sum_n [(E_{\text{exp}}^{(n)} - E_{\text{MQDT}}^{(n)})/\alpha_{\text{exp}}^{(n)}]^2, \tag{4.20}$$

where $E_{\text{exp}}^{(n)}$ and $E_{\text{MQDT}}^{(n)}$ are the experimental and theoretical values of the total energy respectively (for a given value of the principal quantum number n), and $\alpha_{\text{exp}}^{(n)}$ is the uncertainty on the measured total energy. The standard criterion for defining the quality of a fit is the reduced χ^2, $\chi_\nu^2 = \chi^2/\nu$, where ν here is the number of degrees of freedom and should not be confused with an effective principal quantum number, ν_i. A table giving acceptable values of χ_ν^2 can be found on page 107 of [55] for different values of ν; a model is

generally said to fit the data well when $\chi^2_\nu \approx 1$. We use a Nelder-Mead simplex algorithm to find the optimal values for the $K_{i\alpha}$ matrix elements of the reactance matrix [122]. The uncertainties in the parameters are estimated by adding the error bar of each energy level measurement and re-optimizing. The estimate of the uncertainty for each parameter is then given by the difference between the original parameter and the re-optimized parameter. This procedure does not constitute a full calculation of the uncertainty, however, due to the highly correlated nature of the large number of parameters in the fit. A full determination of the uncertainties would be impractical.

4.2.3 Wave Functions and State Fractions

Once the bound state energy levels have been determined, an MQDT model allows the extraction of the composition of the wavefunction by calculating the A_i or B_α coefficients. Landé g_J-factors can be calculated directly from the knowledge of these channel fractions; other observables, however, require the full numerical wavefunction. These numerical wavefunctions are most easily constructed by using the A_i coefficients, as some of the $\phi_i(r)\chi_i$ functions can be calculated using Coulomb functions (see section 2.4.1). We note, however, that these Coulomb functions can only be calculated for $\nu_i > l_i$ [45]; in the case of non-autoionizing doubly excited states, this condition is rarely met for the cases of interest. The solution to this problem will be discussed in section 4.4, and involves fitting the unknown dipole matrix elements to lifetime and oscillator strength data.

When the **K** matrix is known, the A_i coefficients can be extracted by using equation (4.11). This equation on its own, however, has two problems: it does not unambiguously determine the A_i coefficients, and it does not specify the normalization, a normalization that has to be consistent with the definition of the $\phi_i(r)$ functions. Following the normalization of the wavefunctions constructed using Coulomb functions in section 2.4.1, the $\phi_i(r)$ functions are normalized such that

$$\int_0^\infty |\phi_i(r)|^2 dr = 1. \tag{4.21}$$

It has been shown in reference [123] that each individual channel should normalise to ν_i^3, so we adopt the normalization condition that $\sum_i A_i^2 \nu_i^3 = 1$.

By using this normalization condition together with (4.11), the values of the A_i coefficients can be uniquely determined. Finally, we define the normalized channel fractions to be $\tilde{A}_i = A_i \nu_i^{3/2}$. Taking our earlier example of the two-channel model in equation (4.18), the normalized channel fractions are given by

$$\tilde{A}_1 = \nu_1^{3/2} \left[\nu_1^3 + \frac{\nu_2^3 (K_{11} + \tan \pi\nu_1)^2}{K_{12}^2} \left(\frac{\cos \pi\nu_1}{\cos \pi\nu_2} \right)^2 \right]^{-1/2} \tag{4.22a}$$

$$\tilde{A}_2 = -\left(\frac{\nu_2}{\nu_1} \right)^{3/2} \frac{(K_{11} + \tan \pi\nu_1)}{K_{12}} \frac{\cos \pi\nu_1}{\cos \pi\nu_2} \tilde{A}_1. \tag{4.22b}$$

4.2.4 Spin-orbit effects

In certain Rydberg series, the experimental energy level data have small enough uncertainties to distinguish between fine structure components of certain channels. Although these cases are rare in strontium, the ability to fully separate out the different ionization limits allows the inclusion of spin-orbit effects in the MQDT models.

The ionization limits have two fine-structure components each (except, of course, for the $5s_{1/2}$ threshold). If these ionization limits are fully resolved in the MQDT models because the energy level data have small uncertainties, then the channels included in the model will converge to individual ionization limits where the value of the total angular momentum of the inner electron is well defined. This implies that each channel will be jj-coupled, as the orbital angular momentum of each electron will couple more strongly to the spin of that electron than to the orbital angular momentum of the other electron. By resolving all the fine structure components of the ionization limits, the spin-orbit effects can thus be included in the model. If the uncertainties in the experimental data are too large, however, the spin-orbit effects will be too small to be resolved by the model and the resulting MQDT model would be indistinguishable from a model where the spin-orbit effects are neglected. In general, the effects of spin-orbit coupling in the alkaline earth metals are small [113].

Once a jj-coupled MQDT model has been obtained, standard recoupling coefficients can be used to transform the jj-coupled $\tilde{A}_i^{jj}$ to the LS-coupled

$\tilde{A}_i^{LS}$ [40]. Using standard Racah algebra, we find that the transformation is given by

$$\begin{aligned}\bar{A}_i^{(LS)} = &\sum_{i'} \delta_{l_1^{(i')} l_1^{(i)}} \delta_{l_2^{(i')} l_2^{(i)}} \delta_{s_1^{(i')} s_1^{(i)}} \delta_{s_2^{(i')} s_2^{(i)}} \\ &\times \sqrt{(2j_1^{(i')}+1)(2j_2^{(i')}+1)(2L^{(i')}+1)(2S^{(i')}+1)} \\ &\times \begin{Bmatrix} l_1^{(i')} & s_1^{(i')} & j_1^{(i')} \\ l_2^{(i')} & s_2^{(i')} & j_2^{(i')} \\ L^{(i')} & S^{(i')} & J^{(i')} \end{Bmatrix} \bar{A}_{i'}^{(jj)}.\end{aligned} \tag{4.23}$$

4.3 Application to strontium: Bound state energies

In this section we present comprehensive MQDT models for all $L < 4$ Rydberg states of strontium below the first ionization limit (excluding certain low lying states). The presented models are all empirical models based on the most accurate measurements of the bound states available (a list of sources can be found in [124] and [96]). We also compare these models with previous empirical and *ab initio* work that has been done.

Before we delve into the specifics of each series, it is useful to take a step back and take a look at the wider context of the perturbations in each series. Figure 4.1 shows an overview of all the series and their interactions. Most perturbers exist as states which can be uniquely identified as having predominantly doubly excited character; there exist some states, however, that are entirely mixed into the perturbed series (for example, the 4d6s configuration in the $^1D_2$ and $^3D_2$ series), and thus do not appear as a single bound state.

The specific arrangement of the perturbers found in the various Rydberg series can be understood by considering the ionic orbitals that the doubly excited states are composed of. Strontium is a heavy alkaline earth metal, therefore the 5p state of the ion is higher in energy than the 4d state, as shown in figure 4.2. These two ionic states are the lowest in energy, therefore it can be expected that most perturbers below the 5s threshold will be composed of the 5p and 4d states (otherwise the doubly excited states are likely to be autoionizing). Figure 4.1 shows that most of the perturbers are

composed of various permutations of the three lowest lying ionic states, including the 6s state. Parity determines which series will be perturbed by specific configurations, and total angular momentum further decides which symmetries will perturb each series. The Pauli exclusion principle also plays a role, as only even values of $L + S$ are allowed when both valence electrons are in the same orbital [119]. It is found that perturbers with the same total angular momentum but different values of the orbital angular momentum to the perturbed series have a perturbation that is much less widespread than those where the term symbols of the perturber are identical to the perturbed series. The perturbers with the same term symbol as the series being perturbed, however, are found to have dramatic effects, often causing pronounced energy shifts over several states.

Spin-orbit effects are visible in series where the energy levels are highly accurate (such as the singlet S series), although for most series the effects are too small to be resolved; this is consistent with the calculations of [113]. In the broader context of the alkaline earth metals, the perturbations in strontium are stronger than those found in calcium (although similar perturbers exist for both elements), yet weaker than those found in barium [19, 120]. Barium, however, has many more perturbers, causing highly complicated perturbations requiring models that can contain up to nine channels [19, 125].

The rest of this section is devoted to the analysis of the MQDT models. The **K** matrices that were used to produce the results of this section are included in appendix B.

4.3.1 5sns $^1S_0$ States

The singlet S states are relatively well studied, with previous empirical [61, 120, 127] and *ab initio* [128, 129] models available. This series has proved somewhat controversial, as the classification of the perturber found at 37 160.234 cm^{-1} is highly ambiguous with some authors claiming the perturber is the $5p^2$ configuration [61, 124, 127] and others labelling the perturber as $4d^2$ [120, 128]. The reason for this was elucidated by [128, 130, 131], where the authors used *ab initio* models to show that the perturber had almost equal admixtures of both $5p^2$ and $4d^2$ configurations, with only slightly

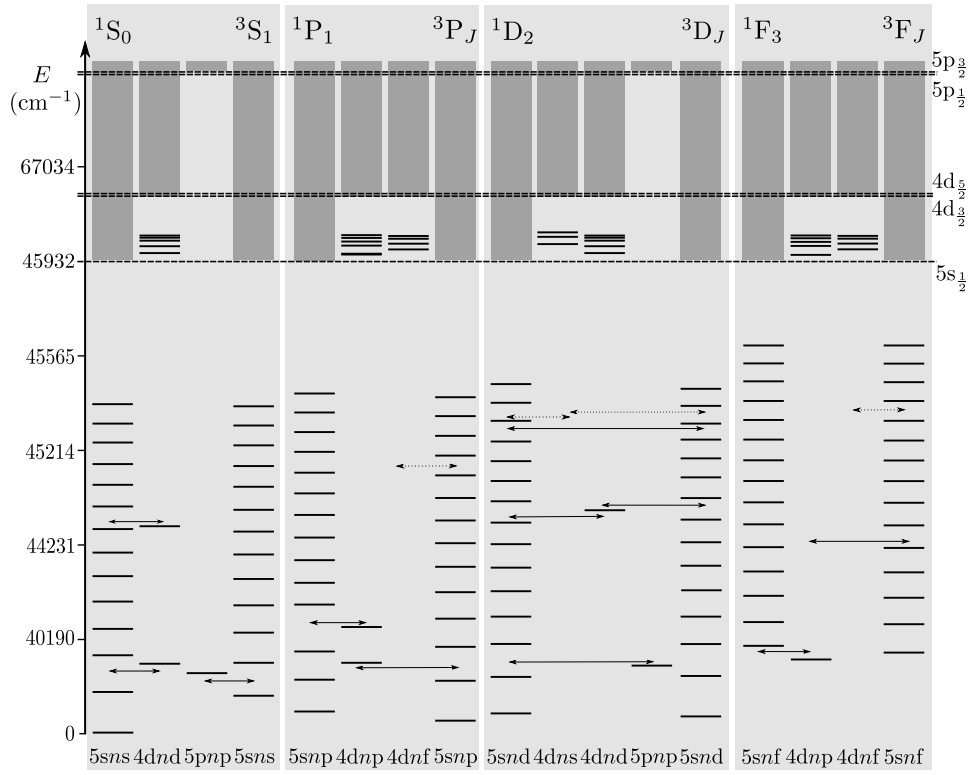

Figure 4.1: An overview of the different singly and doubly excited series in strontium, and the interactions between them. Solid bars denote energy levels in cm^{-1} (the energy scale is non-linear, roughly following an n^{-3} scaling), with dashed lines denoting the various ionization limits. Solid arrows denote a perturbation of a singly excited series by the action of a perturber that exists as a measured physical state, whereas dashed arrows denote a perturbation caused by a doubly excited configuration that is completely mixed into the perturbed singly excited Rydberg series. The darker grey columns denote continua.

more 4d^2 character.

More recently published data [62, 124] for the experimental energy levels of the $^1S_0$ have pushed the level of uncertainty on these energy levels to the 0.001 cm^{-1} level. Consequently, an additional perturbation can be seen around the state at 44525.838 cm^{-1}, labelled as the 4d^2 $^3P_0$ state. The effect of this perturber is very small, although the effect is enough to prevent a good fit when using a two-channel model that ignores fine structure. This was not the case in [61], where the uncertainties were much larger, thereby permitting an adequate description of the series with only two channels.

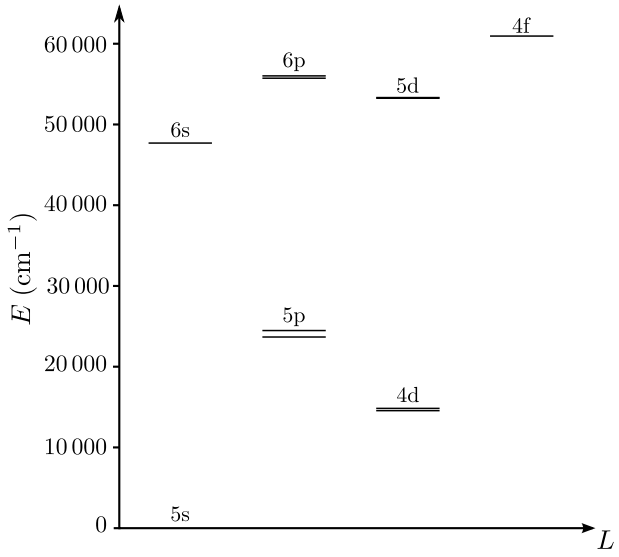

Figure 4.2: Energy levels for the Sr^+ ion, relative to the first ionization limit of strontium. Energies are to scale [126].

Based on the previous MQDT studies of the $^1S_0$ states and the improved energy level measurements, we develop a three channel model that describes the experimental data very well ($\chi^2_\nu = 0.38$). The three channels are the $5sns\ ^1S_0$, the $4d_{3/2}nd_{3/2}$ and the $4d_{5/2}nd_{5/2}$. The resulting LS-coupled channel fractions are shown in figure 4.3. Unfortunately, the perturber at 37 160.234 cm^{-1} could not be included, as the non-linear energy dependences in the **K** matrix cause large deviations at low energy. We include all energy levels for $7 \leq n \leq 30$ (substantial deviations in the single-channel quantum defects predicted by the Rydberg-Ritz formula are evident above $n = 30$, as discussed in [62, 96]); we also include the perturber at 44 525.838 cm^{-1}, but not the perturber at 37 160.234 cm^{-1} due to this perturber lying too low in energy.

The channel fractions show a clear perturbation at the low end of the series due to the action of the lowest lying perturber, and another smaller perturbation due to the perturber at 44 525.838 cm^{-1} (which is not included in the figure). The high-lying perturbation is small, yet non-negligible, especially when considering the radiative lifetimes of the states (as will be discussed in section 4.4).

Regarding the issue of the classification of the state at 37 160.234 cm^{-1}, we

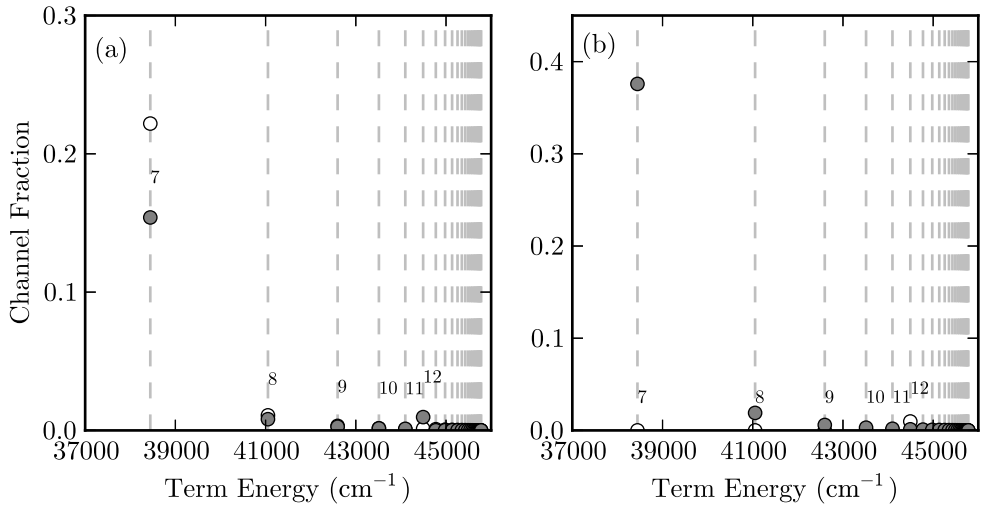

Figure 4.3: Channel fractions for the singlet S states in *LS*-coupling (shown in (a)) and *jj*-coupling (shown in (b)). In (a) the white circles denote the 4dnd ^{3}P$_0$ and the grey circles denote the 4dnd ^{3}P$_0$ channels, and in (b) the white and grey circles denote the 4d$_{5/2}n$d$_{5/2}$ and the 4d$_{3/2}n$d$_{3/2}$ channels respectively. The vertical dashed lines denote the experimental bound states.

cannot make any definite claims as the state is not reproduced by the model, although the lack of a channel with a 5pnp configuration heavily supports the conclusions of [128, 130, 131]. Another three-channel model was attempted, including the 5sns ^{1}S$_0$, 5pnp and 4dnd channels (the latter two channels being taken to converge to the average of the 5p and 4d ionization limits respectively). The resulting MQDT model reproduced the experimental energy levels to within error, but the two perturbers were found to have switched, with the lowest-lying perturber being described by the 4dnd channel and the 4d^2 ^{3}P$_0$ state being described by the 5pnp channel. Not only are these two labels at odds with the *ab initio* MCHF and MQDT calculations, but the lifetimes presented in section 4.4 were also found have large discrepancies when the alternative MQDT model was used.

One way to see the effect of perturbations in a series is by plotting a so-called Lu-Fano plot (named after their inventors). A Lu-Fano plot is a plot of one channel's effective principal quantum number against another channel's, usually modulo 1. The resulting plot effectively shows the energy variation of the effective principal quantum number for a particular channel. Resonance

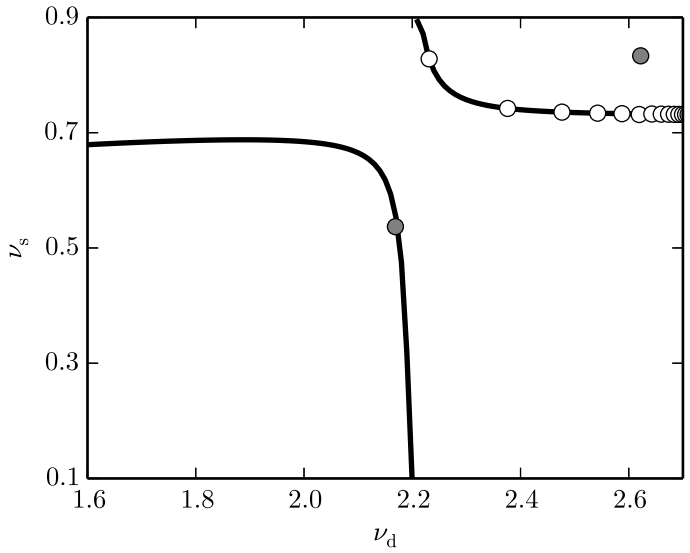

Figure 4.4: Lu-Fano plot for the $^1S_0$ states of strontium. Grey circles denote the two $4d^2$ perturbers ($^1S_0$ and $^3P_0$), while white circles denote the $5sns$ configurations. The black lines were produced using the MQDT given in appendix B. A small resonance feature is observed at $\nu_d \sim 2.6$ (where the perturber appears); this feature has been omitted in the figure for clarity.

features in Lu-Fano plots are typically associated with perturbers in the series; a flat line would indicate no perturbers, and a tilted line indicates an energy dependence in the quantum defect. The Lu-Fano plot for the $^1S_0$ states is shown in figure 4.4. Figure 4.4 contains two resonances (although the resonance associated with the $4d^2\ ^3P_0$ state is too small to be visible on the scale), as is expected with two perturbers in the series.

Finally, we note that the model predicts both perturbers as being better suited to a jj-coupling scheme classification, with the 37 160.234 cm^{-1} and 44 525.838 cm^{-1} states being labelled $4d_{3/2}nd_{3/2}$ and $4d_{5/2}nd_{5/2}$ respectively.

4.3.2 5sns $^3S_1$ States

Compared to the corresponding singlet states, the $5sns\ ^3S_1$ are very poorly known, both from an experimental point of view and from the point of view of the corresponding MQDT analyses. Only one previous *ab initio* study of the $^3S_1$ states has been carried out [128], and no empirical studies exist. The

ab initio study found no perturbers for the series.

As doubly excited states with both valence electrons in the same orbital are disallowed due to the Pauli exclusion principle [119], there exist two candidate perturbers for the triplet S series that have the same parity and total angular momentum: the $5p^2\ ^3P_1$ and the $4d^2\ ^3P_1$. We find no evidence of the $4d^2\ ^3P_1$ perturber, either in a three-channel or in a two-channel model. As such, we construct our MQDT model with the 5s*n*s $^3S_1$ and the 5p*n*p channels (we take an arithmetic average of the fine structure components for the latter channel, as the experimental uncertainties are too large to resolve fine structure; consequently, we do not include the overall term symbol for the second channel). We use energy levels for $7 \leq n \leq 23$, with no perturbers included; the data is sourced from [64, 124, 132].

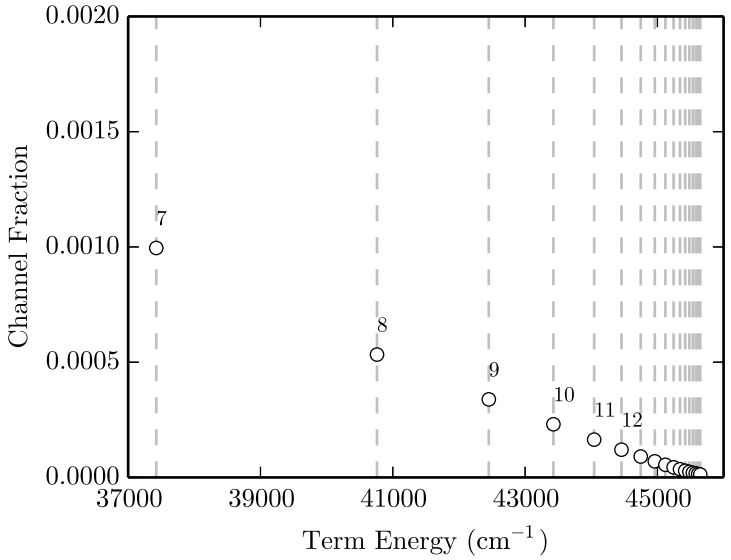

Figure 4.5: Channel fractions for the triplet S states. The white circles denote the 5p*n*p perturber (assumed to be the $^3P_1$ symmetry, as discussed in the text), and the vertical dashed lines denote the experimental bound states.

Figure 4.5 shows the channel fractions for the $^3S_1$. A very small admixture of the 5p*np* channel is found at the low end of the series, which is consistent with the position of the $5p^2\ ^3P_1$ (which is much lower in energy and cannot be reproduced by the model). Other than this small perturbation, the series is essentially unperturbed; this agrees well with the *ab initio* calculations [128].

The Lu-Fano plot for the $^3S_1$ states is given in figure 4.6, and shows a flat

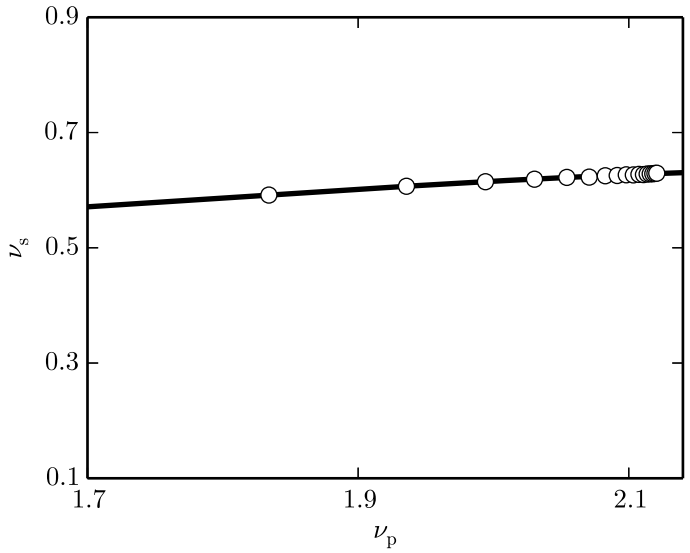

Figure 4.6: The Lu-Fano plot for the triplet S series of strontium. White circles denote experimental measurements of bound states.

line with slight energy dependences. The lack of resonance features in the plot is consistent with a lack of perturbers.

4.3.3 5snp $^1P_1$ States

The singlet P states of strontium are commonly used as an example of the success of MQDT. A lot of work has been done, and the series was the first to be analysed in strontium [61, 133]. The series contains a single perturber, the 4d5p $^1P_1$ state (although at very low energy the 4d5p $^3P_1$ also causes small perturbations [129]). There exist several empirical models [61, 133] and *ab initio* models [128, 129], all of which agree well with the experimental observations. The 5snp $^1P_1$ states are one of two series of states (the other being the 5snf $^1F_3$ states) where fine structure has been included in published *ab initio* models [129].

We construct our MQDT model for the $^1P_1$ states by choosing two channels, the 5snp $^1P_1$ channel and the 4dnp (choosing once again the arithmetic average of the fine structure components of the 4d ionization limits). We use data ranging from $n = 6$ to $n = 29$ (including the perturber at 41 172.054 cm^{-1}), obtained from various sources (choosing the energy levels with the lowest

uncertainty in the case of multiple measurements) [63, 124]. The model fits the data very well, with $\chi^2_\nu = 0.8$.

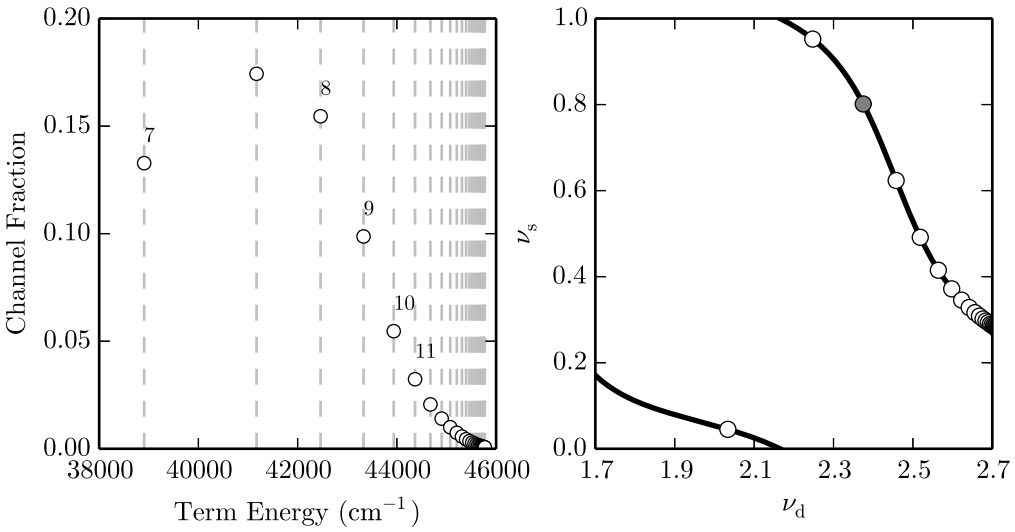

Figure 4.7: Channel fractions (left) and a Lu-Fano plot (right) for the 5snp ^{1}P$_1$. White circles on the left denote the 4dnp channel, with the state between the labelled $n = 7$ and $n = 8$ states corresponding to the 4d5p ^{1}P$_1$ state. On the right the white circles are experimental measurements, and the grey circle denotes the state labelled as 4d5p ^{1}P$_1$.

The channel fractions and the Lu-Fano plot are shown in figure 4.7. Both the channel fractions and the Lu-Fano plot show signs of a very wide perturbation caused by the 4d5p ^{1}P$_1$ state. As a result of this wide perturbation, the 4d5p ^{1}P$_1$ state is mixed into the 5snp ^{1}P$_1$ series over a wide range of n, with a maximum admixture of 18% found in the state labelled 4d5p ^{1}P$_1$, thus confirming the previous label. The new experimental data does not reveal any new information on the interactions between channels in this series, and only serves to narrow the uncertainties on the **K** matrix that is obtained.

4.3.4 5snp ^{3}P$_{0,1,2}$ States

The triplet P states are much less well studied than their singlet counterparts, due to the difficulty of accessing these states experimentally. The experimental values for the energy levels are scarce and have large uncertainties, with only one reference available for the high lying states [65] (although the

$n = 5, 6, 7$ have been measured more precisely [124]).

For the MQDT models, the triplet P states are analysed in the same reference that provides the experimental energy level values. The energy levels calculated using their MQDT models, however, show significant discrepancies with the measured data, often differing by several standard deviations [65]. An *ab initio* model also exists, although this model does not include the different fine structure components. Both the empirical and *ab initio* models include two channels, the 5snp ^{3}P channel and the 4dnp ^{3}P channel.

A two-channel MQDT model was attempted using the same channels as the previous studies, including data provided in [65] and [124] (the $^3P_2$ states above $n = 15$ show large discrepancies in the expected behaviour of the quantum defects and are excluded) for $6 \leq n \leq 15$ and including the corresponding symmetry of the 4d5p ^{3}P perturbers. The two channels were found to be insufficient to provide a good fit. We thus include a third channel converging to the 4d ionization limit (both channels that converge to the 4d ionization limits are taken to converge to the average of the fine structure components), and find that the data fits to $\chi^2_\nu = 1.8, 0.2$ and 0.2 for the $^3P_2$, $^3P_1$ and $^3P_0$ respectively if the $n = 13$ level is excluded for all three symmetries. Including the $n = 13$ level causes the χ^2_ν value to go to 5.6, 3.2 and 7.9 for the $^3P_2$, $^3P_1$ and $^3P_0$ symmetries.

The three-channel fit is adequate for this small number of data points; the deviation of the $n = 13$ level for all three symmetries, however, remains unexplained. A similar isolated discrepancy is not observed in [65], although very few data points in that reference fit to within the uncertainty of the experiment, therefore very little can be said about deviations.

Another difficulty is the labelling of the channels, two of which converge to the same ionization limit. There is therefore no way to distinguish *a priori* which channel is which, and the designation of one of the channels converging to the 4d ionization limit is currently unknown. Multiconfiguration Hartree-Fock calculations have shown that the low n singlet P states contained a small amount of 4d4f, and the triplet states were not analysed. Based on this, we hypothesize that the channels converging to the 4d limit are the 4dnp and 4dnf channel, the latter of which is too weak to be resolved in the

singlet series. Another possibility to explain the presence of the 4dnf channel is the presence of stray electric or magnetic fields, that can potentially cause significant shifts in Rydberg states.

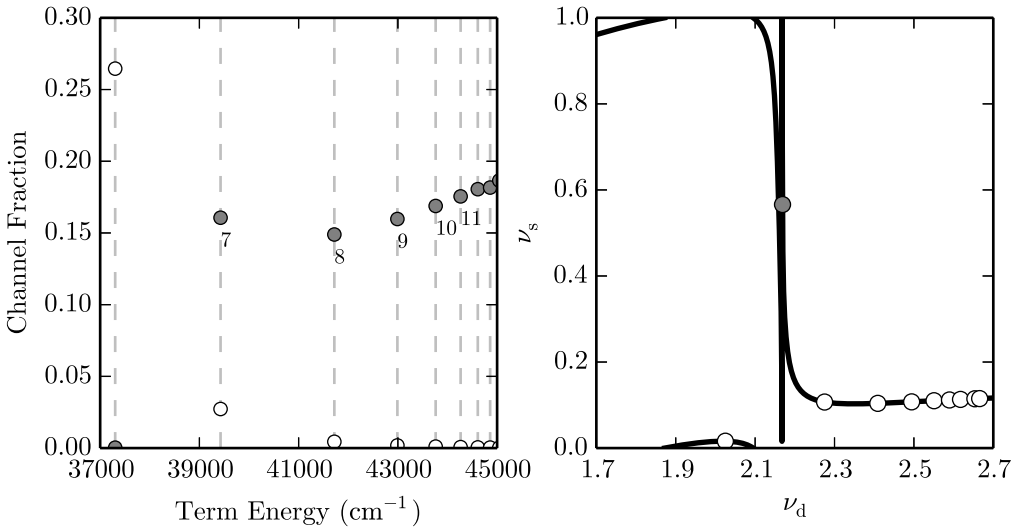

Figure 4.8: Channel fractions (left) and Lu-Fano plots (right) for the 5snp ^{3}P$_1$. On the left, white circles denote the (suggested) 4dnp channel and the grey circles denote the (suggested) 4dnf. On the right, the white circles show the experimental values, with the grey circle showing the perturber labelled as 4d5p ^{3}P$_1$.

The channel fractions and the Lu-Fano plot resulting from the ^{3}P$_1$ state MQDT model (this series is typical of the three symmetries) are shown in figure 4.8. The perturber at 37 302.731 cm^{-1} is well described by the model, showing the second channel to be dominant in that state. The dominance of the second channel allows us to identify the second channel as the 4d5p ^{3}P$_1$ channel and the third channel as the possible 4d4f ^{3}P$_1$. All three fine structure components have similar structure.

This empirical MQDT analysis of the triplet series remains inconclusive due to the large uncertainties in the data. More work, both on the experimental and on the theoretical side would be useful to resolve the issues present in the interpretation of the model. The input of an *ab initio* calculation would be particularly useful to confirm the presence of the 4d4f perturber in the three series.

4.3.5 5snd $^{1,3}D_2$ States

By far the most challenging couple of Rydberg series in strontium are the singlet and triplet D_2 states. These states exhibit a breakdown in LS-coupling around $n = 16$ due to the perturbing 4d6s configuration, and the singlet and triplet series swap their labels at this value of n [61]. The combined action of many perturbers in this series requires a large number of channels to fit the energy level data. This large number of channels leads to a large number of free parameters in the fitting procedure, which complicates the empirical description of this series.

While the $^1D_2$ and $^3D_2$ series (which are inextricably linked by the interaction with the perturbers) are highly complex, this complexity has stimulated a lot of research into these states. The first empirical model used five channels to describe the two series [61], including the $^1D_2$ and $^3D_2$ symmetries of the 5snd configuration, the $^1D_2$ and $^3D_2$ symmetries of the 4dns configuration, and the 5pnp configuration (to an arithmetic average of the fine structure components). The resulting model clearly showed the singlet-triplet switch at $n = 16$, and the model was later successfully applied to Landé g_J factors later on [134]. We note another empirical model exists which only includes three channels for the $^1D_2$ states and a separate two-channel model for the $^3D_2$ states [70], but very large discrepancies can be seen between the experimental and theoretical values. No *ab initio* models exist that include the singlet-triplet mixing, although a four-channel model exists for the $^1D_2$ states and a two-channel model for the $^3D_2$ states [128]. The channels that are included are the 5snd, 4dns, 5pnp and 4dnd channels for the $^1D_2$, and the 5snd and 4dns for the $^3D_2$ states.

We follow the original empirical model of these states; by using more precise energy levels, however, we find that the perturbation of the $4d^2\ ^3P_2$ level has an effect that is resolvable in the experimental data, preventing a good fit for five channels. We thus include six channels, which are detailed in table 4.1.

The resulting MQDT model for the $^{1,3}D_2$ states fits with $\chi^2 = 11.1$ for $7 \leq n \leq 30$. While this is not to within the experimental error, the fit is still a large improvement over previous models (for comparison, the previous

i	LS	jj	Ionization Limit (cm^{-1})	Channel fractions
1	5snd ^{1}D$_2$	5s$_{1/2}n$d$_{3/2}$	45932.1982	$-\sqrt{\frac{2}{5}}A_1^{(jj)} + \sqrt{\frac{3}{5}}A_2^{(jj)}$
2	5snd ^{3}D$_2$	5s$_{1/2}n$d$_{5/2}$	45932.1982	$\sqrt{\frac{3}{5}}A_1^{(jj)} + \sqrt{\frac{2}{5}}A_2^{(jj)}$
3	4dns ^{1}D$_2$	4d$_{5/2}n$s$_{1/2}$	60768.43	$-\sqrt{\frac{2}{5}}A_3^{(jj)} + \sqrt{\frac{3}{5}}A_4^{(jj)}$
4	4dns ^{3}D$_2$	4d$_{3/2}n$s$_{1/2}$	60488.09	$\sqrt{\frac{3}{5}}A_3^{(jj)} + \sqrt{\frac{2}{5}}A_4^{(jj)}$
5	5pnp	5pnp	70048.11	$A_5^{(jj)}$
6	4dnd	4dnd	60628.26	$A_6^{(jj)}$

Table 4.1: Summary of channels used in the six channel ^{1,3}D$_2$ model. The first column shows the channel number, the second and third columns show the channel labellings in LS and in jj-coupling respectively. The last column shows the conversion from jj-coupling to LS-coupling for the channel fractions.

model fits with a $\chi^2 = 36$ to the older data [61], whereas refitting our model to the same data produces $\chi^2 = 1.4$).

The difficulty in obtaining a good fit is as yet unexplained, although there are multiple possibilities. Firstly, it is likely that the uncertainties quoted in [62] are underestimated. The authors claim error bars of 0.001 cm^{-1}; their attempts to fit the series using a seven parameter fit to the Langer formula, however, results in theoretical energy levels that often deviate from the experimental levels by an order of magnitude larger than the experimental uncertainties. Additionally, the energy levels above $n = 34$ show deviations from the systematic trends expected in a Rydberg series, deviations attributed to pressure broadening [62]. Such effects may still affect states with lower n without being visible on the scale of the series of energy levels. Secondly, there is a large discrepancy between the uncertainties in the singlet states and the uncertainties in the triplet states, with differences of up to two orders of magnitude. The discrepancy between the uncertainties of the two series (which are fitted simultaneously) means that much greater weight is given to the singlet states than the triplet, thereby complicating the fitting procedure and possibly preventing a good fit to the same level of accuracy as the singlet states.

Despite the lack of a fit to within the experimental uncertainty, the channel fractions shown in figure 4.9 agree well with the previous empirical model.

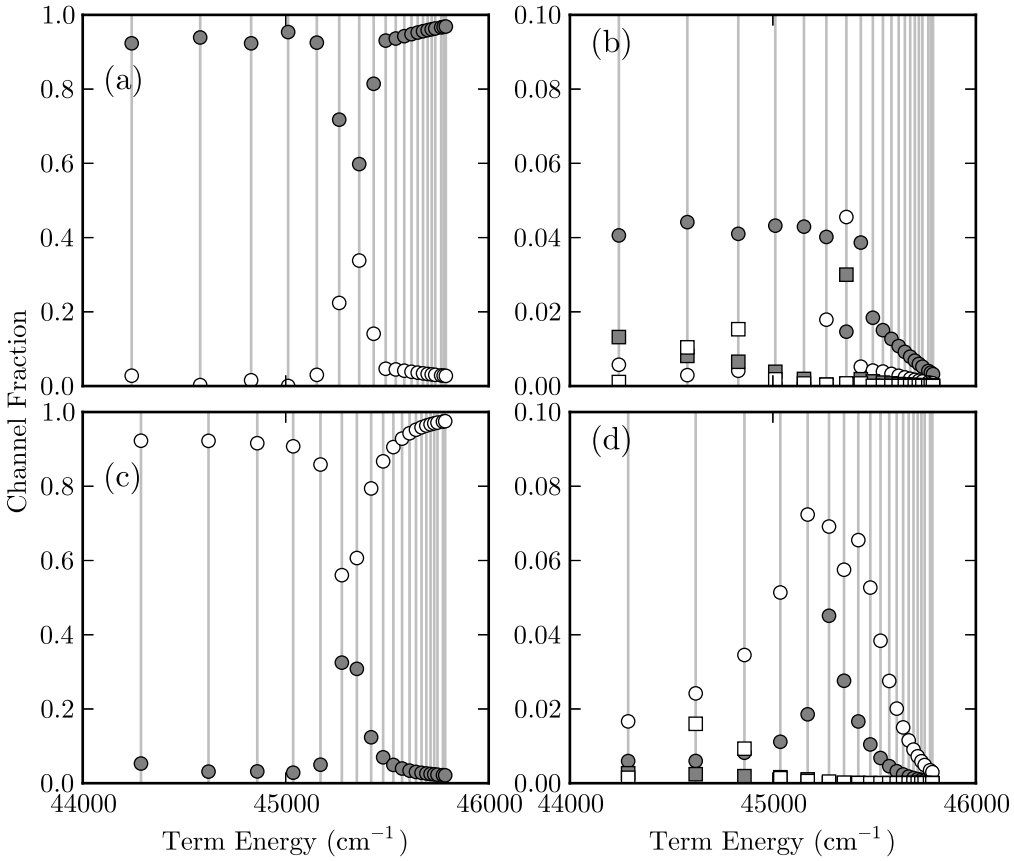

Figure 4.9: Channel fractions for the $^{1,3}D_2$ states. Panels (a) and (c) show the 5snd configurations, with the $^1D_2$ states denoted by grey circles and the $^3D_2$ denoted by white circles. Panels (b) and (d) show the perturber channel fractions. The symbols are: 4dns $^1D_2$ (grey circles); 4dns $^3D_2$ (white circles); 5pnp $^1D_2$ (grey squared; these have been multiplied by 10 for clarity); 4dnd $^3P_2$ (white squares). Panels (a) and (b) show the $^1D_2$ series, and panels (c) and (d) shows the $^3D_2$ series.

The only new feature that was previously unresolved is the perturbation from the $4d^2$ $^3P_2$ state (which is included in the fit). The state contains 92% of the $4d^2$ channel (not shown in figure 4.9), confirming the labelling of this configuration.

A comparison with the *ab initio* is impossible, as spin-orbit effects play a very large role in this series, whereas these effects were neglected in the *ab initio* study [128]. The more recently published results of the *ab initio* calculations including spin-orbit effects make no mention of the $^{1,3}D_2$ states [129, 135].

The inclusion of the 5pnp channel may be a matter of some contention. While this channel is included in the empirical model of [61], the labelling of the perturber at 36 960.842 cm^{-1} (which is labelled as the 5p^2 ^{1}D$_2$ states in [61]) has been debated. Results from various MCHF calculations [130, 131] and the *ab initio* MQDT models [128, 129] have all determined that the dominant configuration of the state found at 36 960.842 cm^{-1} to be the 4d^2 ^{1}D$_2$ state, with a lower admixture of the 5p^2 ^{1}D$_2$ also found. The inclusion of this channel in the empirical fitting, however, would require resolving the fine structure of the 4d ionization limits for the 4d^2 states, meaning that two ionization limits would have two channels converging to them each due to the 4d6s states. This would cause great difficulties due to the labelling ambiguities that would arise. Additionally, the inclusion of such channels would imply more free parameters to be fitted, which would be impossible with the number of energy levels currently available. We thus only retain the 5pnp channel in this model; the combined efforts of an *ab initio* and an empirical model may be required to obtain a model that fully describes the ^{1,3}D$_2$ states.

Before we move on from this series, we take a first look into some of the other physical properties of the ^{1,3}D$_2$ that can be calculated using MQDT; notably, we can calculate Landé g_J-factors just from the knowledge of channel fractions. As mentioned above, the ^{1,3}D$_2$ states of strontium have received particular attention due to their complexity; as such, many different parallel investigations looked into the problem of the singlet-triplet mixing in this series. After the first empirical model was established [61], the same group made an experimental investigation of the response to magnetic fields of the states and made a comparison with the predictions of their MQDT model [120]. The predictions were very successful, demonstrating the predictive power of their MQDT model. We also note that it is possible to incorporate Landé g_J-factors into the fitting procedure; this has been done previously to aid in the fitting of particularly difficult series [19].

Landé g_J-factors can be calculated based solely on the knowledge of the quantum numbers of the state and the channel fractions [23]. Specifically,

the Landé formula, given by [23]

$$g_J^{(i)} = 1 + \frac{J(J+1) + S(S+1) - L(L+1)}{2J(J+1)}. \tag{4.24}$$

gives the g_J-factor for channel i. The total g_J-factor is therefore given by the sum over these channels weighted by the channel fractions,

$$g_J = \sum_i \tilde{A}_i^2 g_J^{(i)}. \tag{4.25}$$

An initial analysis of the Landé g_J-factors showed a large discrepancy with the experimental g_J-factors in [134]. This discrepancy was traced to a particular difficulty in the calculation of the channel fractions: the ionization limits of the two 4d6s and the $4d^2$ channel are so close in energy that the label of the particular channels can switch. At certain energies, several channels can have avoided crossings in the Lu-Fano plot; this is a similar situation to degeneracies in the eigenstates of an effective Hamiltonian. At these points, the eigenvectors of the eigenstates are not uniquely defined, and become particularly difficult to treat. In MQDT, this is equivalent to the label of certain channels becoming arbitrary at certain energies, allowing the calculated channel fractions to swap places. When the normalization is also imposed, the channel fractions become particularly difficult to disentangle. For this reason, using the g_J-factors in the fitting procedure was found to be impossible, as the switching of channel labels in the numerical fitting procedure could not be accounted for.

Despite the difficulties inherent in describing channels converging to near-degenerate ionization limits, a combination of channel labels was found that allowed the experimental g_J-factors from [134] to be reproduced. The resulting g_J-factors are shown in figure 4.10. We note that the experimental data from [134] was normalized to the $n = 12$ point; as this point is subject to an additional perturbation that was not included in the study of [61] and [134], we renormalize the experimental data such that the $n = 11$ has a g_J-factor of unity.

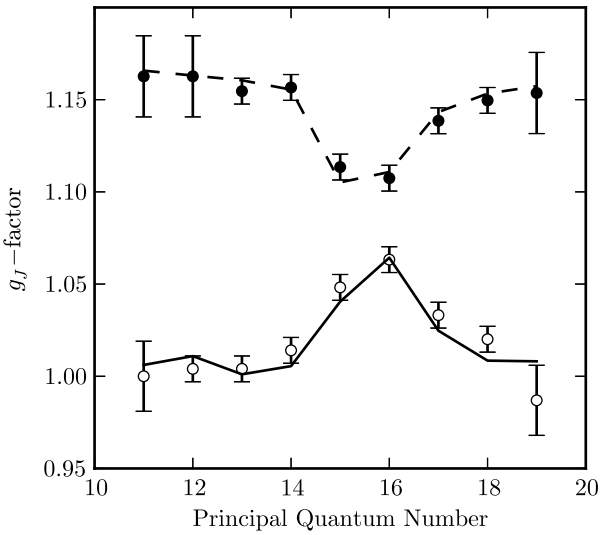

Figure 4.10: Landé g_J-factors for the $^{1,3}D_2$ states. Circles with error bars are experimental data points from [134] (after renormalization; see text for further explanation), with white circles denoting triplet states and black circles denoting singlet states. The solid and dashed lines are the prediction from our MQDT model for the triplet and singlet states respectively.

4.3.6 5snd $^3D_{1,3}$ States

In contrast to the $^{1,3}D_2$ states, the $^3D_{1,3}$ states are much less well studied. Once again, the triplet series are difficult to access, which means that the available energy level data have very large uncertainties. The experimentally measured values of the $^3D_{1,3}$ all come from a single source [64], which also provides an empirical MQDT model of the $^3D_{1,3}$ states. This empirical model once again shows significant discrepancies between the theory and experiment, often differing by as many as seven standard deviations.

The *ab initio* model did investigate the $^3D_{1,3}$ states with a two channel model [128], including the 5snd and 4dns configurations (recall that this model does not distinguish between fine structure components). Similar results to the empirical model of [64] were found in the *ab initio* model.

The discrepancies between the theoretical and experimental values of the $^3D_{1,3}$ states in [64] motivated a reanalysis of the series. A two-channel model containing the 5snd and 4dns configurations were found to be insufficient to describe the series, therefore a three-channel model was used that con-

tained an additional 4dnl channel (with the two perturbing channels taken to converge to the arithmetic average of the two fine-structure components of the 4d ionization limits). This unidentified 4dnl channel is most likely a different symmetry of the $4d^2$ configuration that has not been experimentally measured, based on the parity of the states and the arrangement of energy levels of the Sr^+ ion (see figure 4.2).

The MQDT models for the $^3D_1$ and $^3D_1$ states fit to $\chi^2_\nu = 0.5$ and $\chi^2_\nu = 0.6$ respectively, provided two outliers, the 5s16d $^3D_1$ and the 5s22d $^3D_3$, are excluded. When including these outliers, the $^3D_1$ and $^3D_1$ models fit to $\chi^2_\nu = 26.1$ and $\chi^2_\nu = 2.0$ respectively. The reason for this discrepancy is unknown.

Concerning the identification of the two perturbing channels: as both channels converge to the same ionization limit, the labelling of these channels is implicitly ambiguous. Based on previous work [64, 128], however, the 4dns configuration is expected to have a large impact on the two series. This implies that the largest perturber in these channels is likely to be the 4d6s state, motivating the choice of the 4dns label for the white circles in figure 4.11.

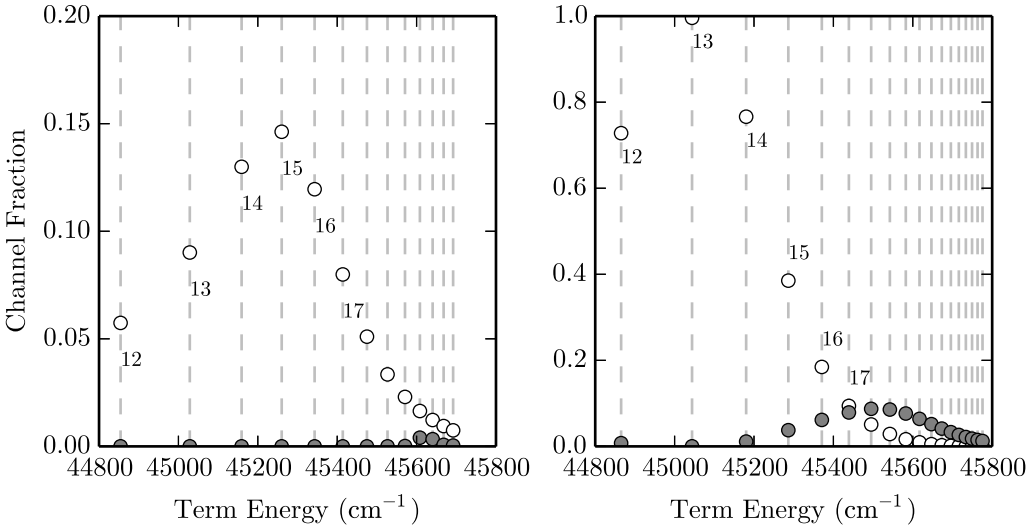

Figure 4.11: Channel fractions for the $^3D_1$ (left) and $^3D_1$ (right) states. White circles are likely to denote 4dns channel fractions and the grey circles are thought to denote 4dnd channel fractions (see the text for a discussion).

The uncertainties on the energy levels measured in [64] are very large. The

unexpected appearance of a third channel converging to the 4d limit could be due to the poor quality of the data. It is also possible, however, that a third perturber was not found in the *ab initio* model due to the lack of fine-structure in this model. More work, both experimental and theoretical, would be required to improve the understanding of these two series.

Before concluding the D states, we note that the third channel (currently thought to be due to the $4d^2$ perturber) can also be taken to converge to the average of the 5p ionization limits. Such models give similar fits. We choose the model presented here due to the high n values where the third channel shows peaks in the channel fractions. Based on other series, the $5p^2$ perturbers tend to be either low-lying or autoionizing, whereas different symmetries of the $4d^2$ perturbers are generally more spread out in energy [124].

4.3.7 5snf ^{1,3}F States

Very little work has been done on the singlet and triplet F states. A single *ab initio* investigation is all that has been carried out in terms of MQDT models [135] (although the focus in this study is the autoionizing states, a small investigation of the bound states is presented). No empirical model exists to our knowledge, although MCHF calculations supplement the calculations of low-n states of the singlet F series [136, 137].

For the singlet F series we construct a similar two-channel model to the $^1P_1$ states, including the 5snf $^1F_3$ and 4dnp $^1F_3$ channels (with the latter converging to the average of the fine structure components of the 4d limits). We include experimental data for $4 \leq n \leq 20$ (including the 4d5p $^1F_3$ state at 38 007.742 cm^{-1}) from [124] and the less precise values from [63] for $20 \leq n \leq 29$. The experimental energy level data for the $^1F_3$ states are somewhat well known in that the uncertainties are much smaller and more states are measured compared to many of the triplet states of other L symmetry. The quality of the experimental data, however, is not comparable to either the $^1S_0$ or the $^1D_2$ states.

The resulting model (with $\chi^2_\nu = 0.8$) produces the channel fractions shown in 4.12. Compared to the *ab initio* predictions, the channel fractions in 4.12

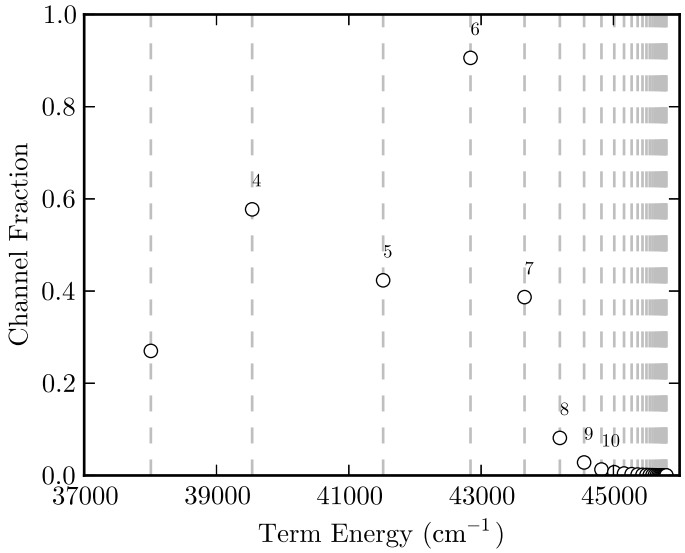

Figure 4.12: Channel fractions for the $^1F_3$ states. White circles denote the 4dnp $^1F_3$ channel.

predict a higher admixture of the 4d5p $^1F_3$ in the 5s4f $^1F_3$, yet a lower admixture in the state labelled 4d5p $^1F_3$. The maximum admixture, contrary to the *ab initio* models, is found in the state labelled 5s6f $^1F_3$. The discrepancies between our empirical model and that of the *ab initio* models remains unexplained. It is possible that the discrepancies arise due to imprecise knowledge of the energy levels; the single-channel quantum defects for the $^1F_3$ are of the order of 0.08, which is very small. These small quantum defects may imply that the series is particularly sensitive to uncertainties in the experimental measurements.

The *ab initio* model of [135] predicts that the 4d5p $^1F_3$ and the 4d5p $^3F_3$ both perturb the $^1F_3$ series. This implies singlet-triplet mixing in the low-n states of the F_3, although this is not visible in our model. The lack of a visible triplet perturbation is probably due to the effect being rather small and being more important at lower energies where the empirical model is not valid. While it may be reasonable to interpret the double-peaked feature of the 4dnp configuration in figure 4.12 as being the two symmetries of the 4d5p perturbers, the state that is conventionally labelled as the 4d5p $^3F_3$ is much lower in energy and thus unlikely to have much effect on the 5s4f $^1F_3$ state.

Turning instead to the $^3F_{2,3,4}$ states, no previous work (either empirical or *ab initio*) exists to guide the study. A two-channel model was attempted including the same configurations as in the $^1F_3$ states; no satisfactory fit was found. A third channel, the 4dnl, was therefore included, converging to the same limit as the 4dnp; this three-channel model produces a fit with $\chi^2 = 0.62$, 0.79 and 0.79 for the $^3F_2$, $^3F_3$ and $^3F_4$ states respectively. All available energy levels between $4 \leq n \leq 24$ are used, with more accurate levels from [124] for $n < 19$ and from [63] for the rest. The uncertainties in the triplet F state energy level measurements are similar to those found for the singlet F series.

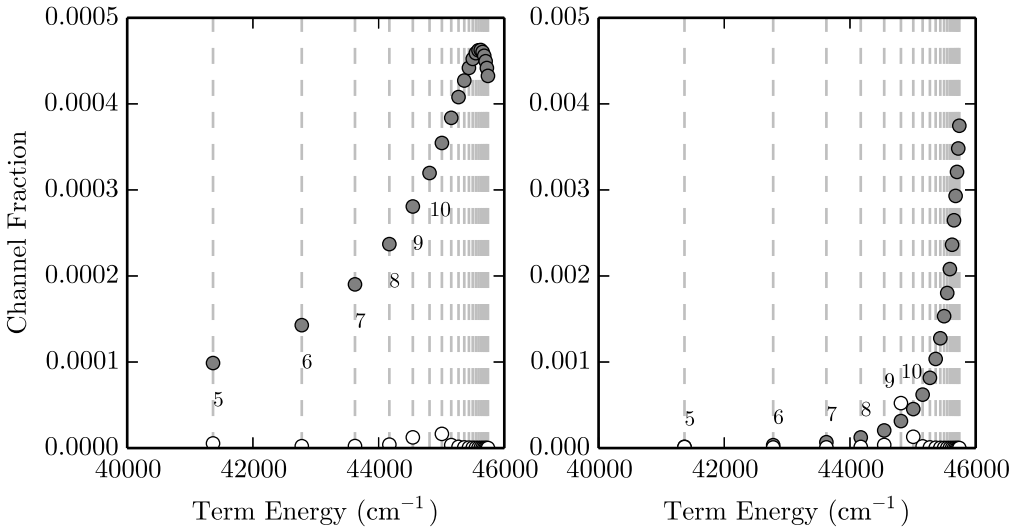

Figure 4.13: Channel fractions for the $^3F_3$ (left) states and the $^3F_4$ (right) states. White circles denote the 4dnp $^1F_3$ channel, and the grey circles denote the channel tentatively assigned to the 4dnf configuration.

The two 4dnl channels are shown in figure 4.13, with the grey circles mainly perturbing the series at high n and the white circles being larger at low n (not shown in figure 4.13). The grey circles are consistent with what we might expect from a 4d4f perturber as the 4f orbital is quite high in energy. The 4d4f perturber was found to have some effect on the $^1F_3$ states by MCHF calculations [137], although the effect is too small to be resolved in the singlet series. The white circles are consistent with the low-lying 4d5p perturber.

While it may be expected that the additional perturbation from the 4dnl channel may be a spurious effect arising from poorly known data, the Lu-Fano

plot in figure 4.14 for the $^3F_{3,4}$ reveals that this may not be the case. A sharp turn in the experimental points around $\nu_d \approx 2.7$ for both series indicates the possible start of a resonance feature, consistent with a perturbation. No non-autoionizing doubly excited states have ever been measured above 45 000 cm^{-1} in strontium to our knowledge. The sharp turn in the two Lu-Fano plots may also be due to stray fields.

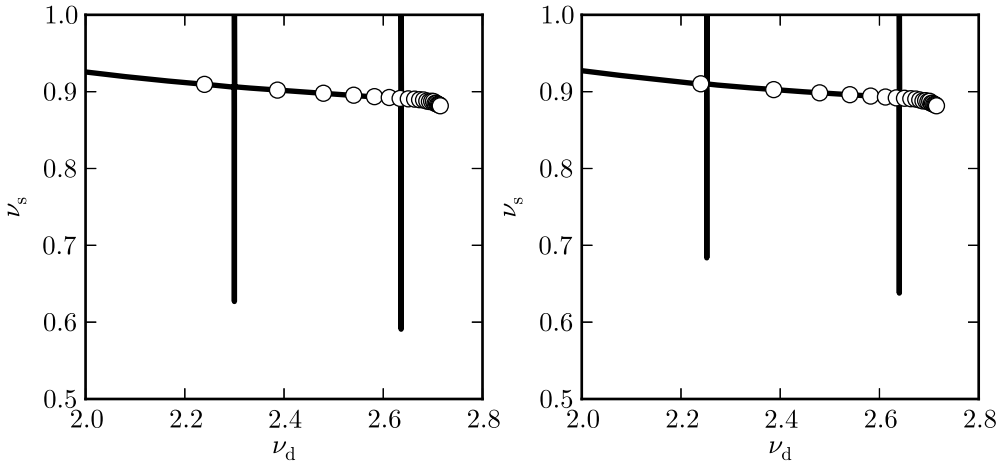

Figure 4.14: Lu-Fano plot for the $^3F_3$ (left) and $^3F_4$ (right) states. White circles are experimental bound states from [63, 124]. Here, ν_d is relative to the average 4d ionization limit, $I_d = 60\,628.26$ cm^{-1}. The thick, black vertical lines are narrow resonance features.

Two very narrow resonance features are also visible in figure 4.14. The feature at higher energy for both the $^3F_3$ and $^3F_4$ series correspond to the peak in the channel fractions shown with white circles. These features may be artefacts of the poor quality of the energy levels.

4.4 Lifetimes and Oscillator Strengths

In principle, once the channel fractions for a specific series are known it is possible to calculate wavefunctions numerically using these channel fractions in combination with the techniques discussed in section 2.4.1. This has never been done to our knowledge, and the main reason is because the doubly excited states occur at low energy. A condition for applying Coulomb

functions to calculate wavefunctions is that $\nu > l$, which is rarely met for perturbers at low energy. Other factors, such as the uncertainties in the channel fractions determined using experimental data with large uncertainties, can contribute to erroneous calculations [138]. The discussion of the lifetimes calculation presented in [138] focus mainly on low energy bound states, where the Coulomb approximation becomes more dubious. Our aim is to calculate Rydberg properties, and as such the Coulomb approximation is much better motivated (see for example the lifetime calculations in rubidium from section 2.6). The uncertainties in our channel fractions may still be problematic; the use of much more accurate energy level data, however, should have partially mitigated this for high n.

In order to avoid the problems outlined above, previous efforts for lifetimes calculations have tackled the issue by factoring out the ν_i^{-3} dependence of each channel's width (or the ν_i^3 dependence of the lifetime). Using this dependence, the widths of each state a, Γ_a, can be found by using

$$\Gamma_a = \sum_i \tilde{A}_i^2 \Gamma_i \nu_i^{-3}, \tag{4.26}$$

where Γ_i is the scaled channel width. The scaled channel widths can then be fitted to a series of lifetimes, and the lifetimes of higher states can then be extrapolated.

This technique was first applied to barium [139], although only one author has investigated the lifetimes in strontium [70, 127]. The MQDT models used in the strontium lifetimes investigation of [70, 127], however, were highly flawed and large discrepancies are observed between the theoretical and experimental values of the energy levels. Additionally, the author has missed a few measurements of the lifetimes, and the resulting fit does not extend very high in n before a discrepancy is observed between experimental lifetime measurements not included in the studies of [70, 127] and the theoretical predictions.

Other efforts to calculate lifetimes used *ab initio* methods; in particular, the R-matrix method was applied to low-n states of strontium with great success [31]. Unfortunately, these authors go no higher than $n = 10$ in their investigation.

In our approach, we attempt to combine various aspects of several of the above studies. For the wavefunctions of the singly excited Rydberg states (where the Coulomb approximation is valid) we use the QDT technique in section 2.4.1. This technique is not generally applicable to the perturbers, however, as the low-energy doubly excited states are too tightly bound to be described by Coulomb functions. Instead, we use experimentally determined values for the lifetimes and oscillator strengths of various series and transitions to fit the required matrix elements of the doubly excited states. To do this we assume that the doubly excited configurations have approximately the same radial wavefunctions, regardless of symmetry (and ignoring possible energy dependences); the variations due to symmetry are accounted for in the calculation of angular matrix elements, which can be separated from the radial calculations and determined using standard angular momentum algebra (see appendix A).

As discussed in chapter 1, the natural width of a state a, Γ_a, is given by

$$\Gamma_a = \frac{4\alpha^2}{3c} \sum_b \omega_{ba}^3 |\langle n_b L_b S_b J_b | \underline{r} | n_a L_a S_a J_a \rangle|^2, \tag{4.27}$$

where the sum over b is over dipole-coupled atomic states below a in energy, and $\omega_{ba} = E_b - E_a$. To apply this to two-electron atoms, we first introduce channels into the summation in (4.27), such that

$$\Gamma_a = \frac{4\alpha^2}{3c} \sum_b \omega_{ba}^3 \left[\sum_{i,j} \tilde{A}_i \tilde{A}_j \langle n_b^{(j)} L_b^{(j)} S_b^{(j)} J_b^{(j)} | \underline{r} | n_a^{(i)} L_a^{(i)} S_a^{(i)} J_a^{(i)} \rangle \right]^2 . \tag{4.28}$$

To calculate the dipole matrix elements, we first label the inner electron as electron 1 and the active electron (meaning the electron that undergoes the transition) as electron 2. Equation (4.28) then becomes (using the results from appendix A)

$$\begin{aligned} \Gamma_a = \frac{4\alpha^2}{3c} \sum_b \omega_{ab}^3 \Bigg[& \sum_{i,j} (-1)^{l_{1,a}^{(i)} + l_{2,\max} + S_a^{(i)}} \tilde{A}_i \tilde{A}_j \\ & \times \sqrt{l_{2,\max}^{(i,j)} (2L_b^{(j)} + 1)(2J_b^{(j)} + 1)(2L_a^{(i)} + 1)} \\ & \times \begin{Bmatrix} J_b^{(j)} & 1 & J_a^{(i)} \\ L_a^{(i)} & S_a^{(i)} & L_b^{(j)} \end{Bmatrix} \begin{Bmatrix} L_b^{(j)} & 1 & L_a^{(i)} \\ l_{2a}^{(i)} & l_{1a}^{(i)} & l_{2b}^{(j)} \end{Bmatrix} R_{ba}^{(ij)} \Bigg]^2 , \end{aligned} \tag{4.29}$$

where the curly brackets denote Wigner $6j$ symbols and

$$R_{ba} = \int_0^\infty \phi_b^{(j)}(r)\phi_a^{(i)}(r)rdr \tag{4.30}$$

denotes a radial matrix element. The width can then be converted to an oscillator strength using [140]

$$f_{ab} = \frac{2J_b+1}{2J_a+1}\frac{\Gamma_{ba}}{2\omega_{ba}^2\alpha^3}. \tag{4.31}$$

As discussed above, the radial matrix elements for singly excited Rydberg states are calculated using Coulomb functions (see section 2.4.1), and the radial matrix elements for doubly excited states are left as free parameters to be fitted to experimental lifetimes and oscillator strengths.

Finally, to take into account the effect of thermal radiation which couples nearby Rydberg levels and thus modifies the lifetimes, we use equations (2.40) and (2.41) as discussed in section 2.6. In the summation over states coupled by the vacuum (denoted as states c in (2.41)), we include all dipole-coupled states such that $n_c \leq n_a+5$. Changing this to $n_c \leq n_a+10$ changes the third significant figure, which is within the error of both the experimental uncertainty and the uncertainty on the calculation from the Coulomb functions.

Experimental values for Rydberg state lifetimes and oscillator strengths in strontium are scant. Most lifetime measurements do not extend above $n = 22$ for any series, and when multiple measurements of the same level are available the measurements are often in disagreement (see, for example, [31], where many experimental values are quoted from different sources). For the $^1S_0$ series, we use lifetime measurements from [141–143], and for the $^1D_2$ series the measurements used are from [141, 142, 144]; high-n lifetimes are also included from [20, 145]. When calculating the various lifetimes, we include all states for which there are experimental data points above $n = 10$; this is to avoid errors from the numerical QDT radial wavefunction calculations, which were found to have significant errors in rubidium for $n \leq 8$ (see section 2.6).

The oscillator strength data used is also obtained from few sources, although those sources cover a large number of Rydberg states. For the $5s^2\ ^1S_0 \rightarrow 5sn\text{p}\ ^1P_1$ and $5\text{p}5\text{p}\ ^1P_1 \rightarrow 5snd\ ^1D_2$ states we use data from [146–149]; we

Transition	Radial dipole matrix element
$\langle 4d6s\|r\|4d5p\rangle$	6.48(5)
$\langle 5p^2\|r\|4d5p\rangle$	-3.10(8)
$\langle 5p^2\|r\|5s5p\rangle$	-32(2)
$\langle 4d^2\|r\|4d5p\rangle$	-12.7(4)
$\langle 4d^2\|r\|4d4f\rangle$	28(3)

Table 4.2: Radial matrix elements (in atomic units) of the doubly excited states, as obtained by fitting to the experimental lifetimes. Parameter sensitivities to the uncertainties in the experimental data are shown in brackets, and are obtained by reoptimizing the fitted parameters to the experimental data with their uncertainties added.

note that reference [149] has measured gf-values (i.e. oscillator strengths multiplied by the degeneracy factor, $g = 2J + 1$), and therefore need to be divided by $2J+1$ to match our definition of the oscillator strength in (4.31).

As the channel fractions obtained from the MQDT models do not extend to low n, the description of lifetimes and oscillator strengths would be very poor if using only the channel fractions derived from MQDT alone. We therefore include the eigenvectors of MCHF calculations to supplement our own MQDT channel fractions, taking these eigenvectors for the lowest lying states of each series (for $n = 4, 5$) [137].

The resulting radial matrix elements from the fitting to lifetimes and oscillator strengths are shown in table 4.2. The fit gives a value of $\chi^2_\nu = 3.8$; however, the calculated value for the 5s15d $^1D_2$ state is many standard deviations from the experimental value, and when this is excluded the fit results in $\chi^2_\nu = 1.5$. The discrepancy for the 5s15d $^1D_2$ level is most likely due to the channel fractions, which may have a large error due to the extremely complicated interplay between the many perturbers affecting the levels around this energy.

The resulting lifetimes, calculated using the radial matrix elements shown in table 4.2, are shown in figure 4.15 for the $^1S_0$ and $^1D_2$ states. The general trend is well reproduced for both the $^1S_0$ and $^1D_2$ states, and can be seen to have very good agreement over a large range of n, especially for the $^1D_2$

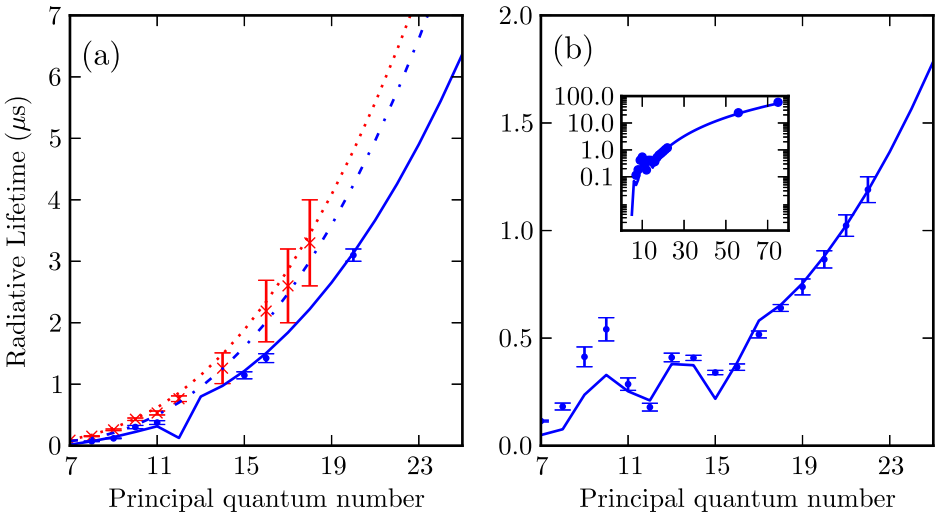

Figure 4.15: Panel (a): Lifetimes for the $^1S_0$ states of strontium (blue lines and circles) compared to the $^2S_{1/2}$ states of rubidium (red dotted line and crosses). Results of the calculation of the lifetimes based on a one-electron model are shown as the dash-dotted blue line. Panel (b): Lifetimes for the $^1D_2$ states of strontium, with the theoretical values shown by the blue solid line and the experimental points shown by blue circles. The inset shows the same as the rest of panel (b) on a logarithmic plot, and extended to higher n.

states.

The lifetimes of the Rydberg states of two-electron atoms depend heavily on the presence of perturbers [31, 144]. Comparing the lifetimes of strontium (figure 4.15) and rubidium (figure 2.3), the lifetimes for strontium can be seen to be about an order of magnitude smaller than the lifetimes of rubidium for the same values of n. In order to understand the contributions that the perturbers can have on the Rydberg series as a whole, it is useful to break up the full natural width into the various contributions from each state's channel. We thus define the channel partial width of state a for channel i, $\gamma_a^{(i)}$, to be

$$\gamma_a^{(i)} = \frac{4\alpha^3 \bar{A}_i^2}{3} \sum_b \omega_{ab}^3 |\langle \psi_b | \underline{\hat{d}} | \psi_a \rangle|^2. \tag{4.32}$$

These channel partial widths are shown in figure 4.16. Figure 4.16 clearly demonstrates the large effect of the perturbers on the Rydberg lifetimes. In fact, the sum of the channel partial widths for the perturbing states are

seen to dominate the total width for the $^1D_2$ states. This explains the large difference between the Rydberg state lifetimes of strontium and rubidium, as the doubly excited perturbers are very short lived and quench the total lifetime of each Rydberg state.

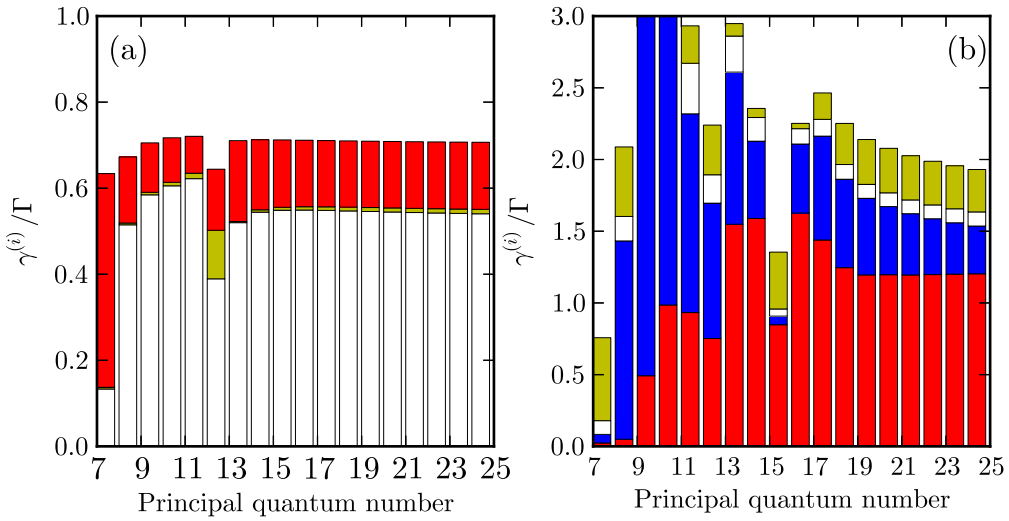

Figure 4.16: Channel partial widths of the $^1S_0$ (a) and $^1D_2$ (b) Rydberg states. For the $^1S_0$ states in panel (a), the white bars denote the 5sns channel, the red bars denote the 4dnd $^3P_0$ channel and the yellow bars denote the 4dnd $^1S_0$ channel's partial widths. For the $^1D_2$ states in panel (b), the white bars denote the 5snd $^1D_2$, the red bars denote the 4dns $^1D_2$, the blue bars denote the 5pnp $^1D_2$ and the yellow bars denote the sum of the three other channel partial widths, 5snd $^3D_2$, 4dns $^3D_2$, and 4dnd $^3P_2$.

While the effect of the perturbers may not be so large that all the physical properties of Rydberg states are clearly affected, for certain properties, like the lifetimes, the effect is crucial to the description of the Rydberg states. In the case of the lifetimes, the ω_{ab}^3 term in equation (4.27) is the term that causes the perturbers to dominate; as most perturbers are found at low-n, the perturbers couple very strongly between themselves. For states with a small admixture of the perturbers, the ω_{ab}^3 term ensures a strong coupling to the low-lying perturbers of opposite parity in the decay channels, giving rise to the quenching of the total Rydberg lifetimes. Thus, the sensitivity of the physical property to the presence of perturbers depends mostly on the energy dependence of this physical property. In the next chapter, the multichannel

dipole matrix elements derived above will be used to investigate the effect of perturbers on the long-range interaction between atoms in Rydberg states, which is expected to be less influenced by perturbers due to the inverse dependence on the Förster defect.

4.5 Conclusions

This chapter was dedicated to investigating the effects of the second electron on the physical properties of Rydberg states of strontium. In particular, the admixture of doubly excited states of the same energy, parity and total angular momentum into the singly excited Rydberg states was studied for all series of strontium with $L \leq 3$.

In order to investigate two-electron effects, we have developed MQDT models for the $^1\mathrm{S}_0$, $^3\mathrm{S}_1$, $^1\mathrm{P}^\mathrm{o}_1$, $^3\mathrm{P}^\mathrm{o}_{0,1,2}$, $^{1,3}\mathrm{D}_2$, $^3\mathrm{D}_{1,3}$, $^1\mathrm{F}^\mathrm{o}_3$ and $^3\mathrm{F}^\mathrm{o}_{2,3,4}$ series of strontium. We began by reviewing and elaborating on the specific procedures involved in obtaining MQDT models, choosing the specific formalism of the reactance matrix, $\mathbf{K}$, to describe the interactions between the different channels in each series. Using the reactance matrix, we reviewed the process of extracting bound state energy levels and channel fractions.

A review of the available empirical (models which have been fitted to reproduce experimental energy levels) and *ab initio* (models where the reactance matrices are calculated with no input from experiment) models is presented for each series before detailing the results obtained from our own analysis. Most models agree well with the models obtained previously; modern experimental data, however, has allowed a more rigorous analysis of certain series. For example, for the $^1\mathrm{S}_0$ states we are able to resolve the fine structure components of the $4\mathrm{d}^2$ configuration, allowing us to investigate the effect of the very small perturbation of the $4\mathrm{d}^2\ ^3\mathrm{P}_0$ state on the $^1\mathrm{S}_0$ Rydberg states. The data for some series, for example the $^3\mathrm{P}^\mathrm{o}_{0,1,2}$ or the $^3\mathrm{F}^\mathrm{o}_{2,3,4}$ states, were found to be sparse and have large uncertainties. In these series, three channels are required to describe the data to within error, although the third channel (tentatively labelled as the $4\mathrm{d}n\mathrm{f}$ configuration) has yet to be confirmed. This channel could be an artefact of the poor quality of the data. More experi-

mental data would be useful to draw more meaningful conclusions from the data.

The effect of perturbers on the Rydberg state lifetimes was investigated by expanding the expression for the natural widths of atomic states in terms of channels. By splitting up dipole matrix elements into radial and angular matrix elements, and calculating the angular part using standard Racah algebra, we find that the singly excited state Rydberg wavefunctions can be calculated using Coulomb functions. doubly excited state wavefunctions, however, were much more complicated, and the radial dipole matrix elements for these were left as parameters to be fitted to experimental values of the lifetimes and oscillator strengths of Rydberg states.

The development of MQDT descriptions of two-electron effects allows us to extend the formalism presented in chapter 3 to include multiple channels, as will be presented in chapter 5.

Chapter 5

Spin-forbidden dipole-dipole interactions in strontium Rydberg atoms

5.1 Introduction

In chapter 4 we developed the necessary tools to describe the impact of two-electron effects on the physical properties of Rydberg states. The one-electron approximation was seen to break down in low-n Rydberg states containing substantial configuration interaction, arising from the presence of doubly excited perturbers. We now extend the discussion of Rydberg-state long-range interactions presented in chapter 3 to include the effect of the second valence electron in strontium.

The reasons for investigating the impact of two-electron effects on the long-range interactions are two-fold. Firstly, this type of investigation is a useful benchmark for determining the applicability of the one-electron model when calculating Rydberg state properties of two-electron atoms, which has been used in a range of calculations [22, 114]. For very high values of n, the one-electron model is known to satisfactorily reproduce the experimental data when calculating Stark maps [22, 114]. However, it is unclear under what conditions it becomes important to take the second electron into account.

The second reason for investigating these two-electron effects is more practical. Spin-orbit effects and the presence of perturbers leads to the weak admixture of certain series, notably in the $^{1,3}D_2$ states (as shown in the previous chapter). The weakly-allowed transitions between series with different spins have already proved a key feature of many experiments such as optical clocks [25, 26], and are at the heart of some proposals for simulating quantum many-body physics [12, 24]. So far, however, the focus of these investigations has remained on the $5s^2\ ^1S_0 \rightarrow 5s5p\ ^3P_{0,1}$ transitions, where both the initial and final states have very weak interactions. Rydberg dressing may enhance the weak interactions [26]; however, the Rydberg dressing technique has yet to be demonstrated. We propose to use the interactions between Rydberg atoms of different spin states that are allowed via the singlet-triplet mixing mechanism demonstrated in the previous chapter.

In this chapter we explore the effects of perturbers on the long-range interactions. We apply the MQDT dipole matrix elements of chapter 4 and the calculation of the C_6 coefficients presented in chapter 3 to the exploration of the impact of two-electron effects. We then proceed to explore the dynamics of spin-forbidden transitions induced by the dipole-dipole interactions between atoms, examining specifically the case of atoms in a one-dimensional lattice. Finally, we suggest possible links between these spin-forbidden transitions and systems such as Fermi liquids [32] or molecular imaging techniques known as Förster resonant energy transfer [150].

5.2 Theory of Dipole-Dipole Interactions in Two-Electron Atoms

In chapter 3, we derived the interaction Hamiltonian for two one-electron atoms separated by a distance R. We found that the two-electron version of this Hamiltonian in (3.10) reduced to the one-electron case when terms involving the inner orbital were neglected. The resulting one-electron two-atom Hamiltonian could be expanded in terms of the multipolar expansion given in (3.11). Here we will only consider the dipole-dipole interaction term,

where the Hamiltonian is given by [90]

$$H_{\text{int}} = -\frac{4\pi}{3R^3} r_1 r_2 \left(Y_{1,1}(\hat{r}_1)Y_{1,-1}(\hat{r}_2) + Y_{1,-1}(\hat{r}_1)Y_{1,1}(\hat{r}_2) + 2Y_{1,0}(\hat{r}_1)Y_{1,0}(\hat{r}_2)\right), \tag{5.1}$$

where all the symbols are have the same meaning as those in chapter 3.

To calculate the matrix elements of (5.1), we must take into account the multichannel nature of the wavefunctions. As such, we cannot use the same formalism as in chapter 3, as we must factorize out certain angular parts to perform the sum over channels. We therefore write the matrix elements as

$$V_{ij}(R) = \sum_{q} \sum_{q_1} \sum_{q_2} \frac{\Omega_{12}^{(ij)}(q, q_1, q_2)}{R^3} \Omega_1^{(ij)} \Omega_2^{(ij)} P_1^{(ij)} P_2^{(ij)}, \tag{5.2}$$

where Ω_1 and Ω_2 are the corresponding single-atom angular dipole matrix elements, and $\Omega_{12}^{(ij)}$ is a coupling matrix element that depends on the total angular momentum quantum numbers of each atom, J_1 and J_2, and their projections on the z-axis, M_1 and M_2. The quantities P_1 and P_2 are single-atom radial dipole matrix elements for atoms 1 and 2 transitioning from pair state i to pair state j. The interaction between the two atoms can thus be written in terms of single atom transitions and a simple coupling factor, thereby simplifying the computational procedure.

So far, we have not applied any of the multichannel formalism. As discussed in chapter 4, the presence of doubly excited states in the Rydberg series requires the inclusion of multiple channels that couple together. Using the MQDT formalism, the wavefunction of a state at a certain energy is given as an expansion in terms of long-range scattering channels,

$$|\psi\rangle = \sum_{k} \tilde{A}_k |\phi^{(k)}\rangle, \tag{5.3}$$

where k is a channel index, $|\phi^{(k)}\rangle$ is the state vector of the long-range channels (for electrons far from the core, these are given by Coulomb wavefunctions) and $\tilde{A}_k$ is the normalized admixture coefficient of that channel in the total state $|\psi\rangle$ (following the normalization procedure of section 4.2.3).

Taking into account the existence of cross-terms between channels, we see that we cannot just sum expression (5.2) over the different channels. To correctly describe these channels, we must include the sum over channels in

the calculation of the dipole matrix elements. Recall from chapter 4 that we write the multichannel dipole matrix element as

$$\langle\psi_i|\underline{r}|\psi_j\rangle = \sum_{k,l} \tilde{A}_k \tilde{A}_l \langle\phi^{(k)}|\underline{r}|\phi^{(l)}\rangle, \tag{5.4}$$

where l is the channel index for state j. We thus rewrite the dipole-dipole interaction matrix element in (5.2) as

$$\begin{aligned} V_{ij}(R) = &\sum_{q} \sum_{q_1,q_2} \sum_{k_1,l_1} \sum_{k_2,l_2} \frac{\Omega_{12}^{(ij)}(q,q_1,q_2)}{R^3} \\ &\times \tilde{A}_{k_1} \tilde{A}_{k_2} \tilde{A}_{l_1} \tilde{A}_{l_2} \Omega_1^{(k_1 l_1)} \Omega_2^{(k_2 l_2)} P_1^{(k_1 l_1)} P_2^{(k_2 l_2)}. \end{aligned} \tag{5.5}$$

Examining first the angular factors, for two electron atoms with the possibility of doubly excited states we consider the case where the electron a (active) makes a dipole transition and electron p (passive) remains in the same state. For a single-atom transition of atom α in the pair state i to the pair state j, the angular dipole matrix element is given by [151]

$$\begin{aligned} \Omega_\alpha^{(ij)} = &(-1)^{S_\alpha^{(i)} + l_{\alpha,\mathrm{p}}^{(i)} + l_{\alpha,\mathrm{a}}^{(i)} + J_\alpha^{(j)}} C^{l_{\alpha,\mathrm{a}}^{(j)}}_{l_{\alpha,\mathrm{a}}^{(i)} 010} \\ &\times \sqrt{(2l_{\alpha,\mathrm{a}}^{(i)}+1)(2L_\alpha^{(i)}+1)(2L_\alpha^{(j)}+1)(2J_\alpha^{(i)}+1)} \\ &\times \begin{Bmatrix} J_\alpha^{(j)} & 1 & J_\alpha^{(i)} \\ L_\alpha^{(i)} & S_\alpha^{(i)} & L_\alpha^{(j)} \end{Bmatrix} \begin{Bmatrix} L_\alpha^{(j)} & 1 & L_\alpha^{(i)} \\ l_{\alpha,\mathrm{a}}^{(i)} & l_{\alpha,\mathrm{p}}^{(i)} & l_{\alpha,\mathrm{a}}^{(j)} \end{Bmatrix}, \end{aligned} \tag{5.6}$$

as derived in appendix A. The coupling matrix element for the full two-atom transition is then given by

$$\begin{aligned} \Omega_{12}^{(ij)} = &(-1)^{1+q_1+q_2} \sqrt{\frac{24\pi}{5}} C^{2,q}_{1,q_1,1,q_2} \\ &\times C^{J_1^{(j)},M_1^{(j)}}_{1,q_1,J_1^{(i)},M_1^{(i)}} C^{J_2^{(j)},M_2^{(j)}}_{1,q_2,J_2^{(i)},M_2^{(i)}} Y_{2,q}(\hat{R}). \end{aligned} \tag{5.7}$$

As in the previous chapters, $C^{JM_J}_{j_1 m_1, j_2 m_2}$ denotes a Clebsch-Gordan coefficient and $Y_{2,q}$ is a spherical harmonic. It should be noted that the $C^{J^{(j)},M^{(j)}}_{1,q,J^{(i)},M^{(i)}}$ Clebsch-Gordan coefficient is part of the single-atom angular dipole matrix element in appendix A, although we place the coefficients in the definition of the coupling matrix element as these must be included in the sums over the polarizations, q_1 and q_2.

For the radial dipole matrix elements $P_1^{(k_1 l_1)}$ and $P_2^{(k_2 l_2)}$, their calculation depends on whether the states are singly or doubly excited. We follow the same

procedure as in chapter 4 for the calculation of these radial dipole matrix elements: the singly excited states are calculated using Coulomb functions, and the doubly excited states matrix elements are taken from table 4.2.

5.2.1 Connection with Two-Electron Interaction Hamiltonian

In chapter 3, the full interaction Hamiltonian between a pair of two-electron atoms was given by equation (3.10). We briefly draw the link between the multichannel formalism presented in the preceding section and the terms in (3.10).

Were we to apply the multipolar expansion in (3.11) to (3.10) we would find four different multipolar expansions, corresponding to the interactions between the two pairs of valence electrons. Note that these would also cancel all the nuclear polarization and nuclear-nuclear interaction terms, as discussed in section 3.3. Considering only the dipole-dipole interactions, we write the radial coordinate of the outer orbital for atom a as $r_a^{(\mathrm{o})}$, and the equivalent for the inner orbital as $r_a^{(\mathrm{i})}$. For clarity, we also collect together all other terms (including the sum over spherical harmonics) into the factor β (with the superscripts i and o denoting the inner and outer orbital respectively). The full two-electron interaction Hamiltonian therefore simplifies to

$$H_{\mathrm{int}}^{(2e)} = \beta^{(\mathrm{ii})} r_1^{(\mathrm{i})} r_2^{(\mathrm{i})} + \beta^{(\mathrm{io})} r_1^{(\mathrm{i})} r_2^{(\mathrm{o})} + \beta^{(\mathrm{oi})} r_1^{(\mathrm{o})} r_2^{(\mathrm{i})} + \beta^{(\mathrm{oo})} r_1^{(\mathrm{o})} r_2^{(\mathrm{o})}. \tag{5.8}$$

Equation (5.1) thus corresponds to taking the final term in (5.8).

The terms involving $r_1^{(\mathrm{i})}$ and $r_2^{(\mathrm{i})}$ cause transitions for the inner electron, leaving the core in an excited state. For singly excited Rydberg states, an excitation of the inner core would leave the atom in an autoionizing state. The radial dipole matrix elements for these transitions (given in table 4.2) are much smaller than the Rydberg-Rydberg transitions that dominate. Additionally, the autoionizing states are very far in energy compared to nearby dipole-coupled Rydberg states. The total coupling to autoionizing states will thus be very small, and can be safely ignored.

For doubly excited states, the transitions induced by $r_1^{(\mathrm{i})}$ and $r_2^{(\mathrm{i})}$ are equivalent to taking the inner electron as the active electron in the transition, just

as we have done in chapter 4. Therefore, by applying the MQDT formalism, we take into account the effect of $r_1^{(\mathrm{i})}$ and $r_2^{(\mathrm{i})}$ in (5.8) while neglecting the coupling to states above the ionization threshold.

5.2.2 Effect of Interactions on Wavefunction

To obtain the energy shifts due to the dipole-dipole interactions we can use the same perturbative and non-perturbative methods as in chapter 3, using the multichannel calculations mentioned in the preceding section to obtain the matrix elements of the dipole-dipole interaction. The effects of dipole-dipole interactions, however, are not limited to the energy level shifts; in this section we briefly examine the effect of interactions on the wavefunctions.

We once again turn to perturbation theory to determine the change in the wavefunctions due to the dipole-dipole interaction. For clarity, we have omitted the discussion of the effect of Zeeman degeneracies, however in practice these degeneracies must be taken into account. Writing the initial state vector as a perturbative series, we have

$$|\psi\rangle = |\psi^{(0)}\rangle + |\psi^{(1)}\rangle + |\psi^{(2)}\rangle + \dots \tag{5.9}$$

To find the new perturbed wavefunction, $|\psi'\rangle$, we can write the expansion in (5.3) in terms of a new expansion with the same channels, but different admixture coefficients,

$$|\psi'\rangle = \sum_k \tilde{A}'_k |\phi^{(k)}\rangle, \tag{5.10}$$

where the perturbed admixture coefficients are given by

$$\begin{aligned} \tilde{A}'_k &= \langle\phi^{(k)}|\psi\rangle \\ &= \langle\phi^{(k)}|\psi^{(0)}\rangle + \langle\phi^{(k)}|\psi^{(1)}\rangle + \langle\phi^{(k)}|\psi^{(2)}\rangle + \dots \end{aligned} \tag{5.11}$$

We thus define the zeroth, first and second order perturbative admixture coefficients as

$$\tilde{A}_k^{(0)} = \langle\phi^{(k)}|\psi^{(0)}\rangle \tag{5.12a}$$

$$\tilde{A}_k^{(1)} = \langle\phi^{(k)}|\psi^{(1)}\rangle \tag{5.12b}$$

$$\tilde{A}_k^{(2)} = \langle\phi^{(k)}|\psi^{(2)}\rangle. \tag{5.12c}$$

The first order term in (5.9) is given by

$$|\psi^{(1)}\rangle = \sum_{j\neq\psi} \frac{\langle j^{(0)}|V|\psi^{(0)}\rangle}{E^{(0)} - E_j^{(0)}} |j^{(0)}\rangle, \tag{5.13}$$

where $E^{(0)}$ and $E_j^{(0)}$ are the zeroth-order energies of the $|\psi^{(0)}\rangle$ and the (unperturbed) intermediate $|j^{(0)}\rangle$ states. Note that the sum over the intermediate states is only over those states that are dipole-coupled to the $|\psi^{(0)}\rangle$ state. The sum over the intermediate states also includes an implicit sum over the relevant MQDT channels for those states. The first-order admixture coefficient is then given by [152]

$$\begin{aligned} \tilde{A}_k^{(1)} &= \sum_{j\neq\psi} \frac{\langle j^{(0)}|V|\psi^{(0)}\rangle}{E^{(0)} - E_j^{(0)}} \langle \phi^{(k)}|j^{(0)}\rangle \\ &= 0, \end{aligned} \tag{5.14}$$

as $|\phi^{(k)}\rangle$ and $|j^{(0)}\rangle$ are orthogonal. Similarly, for the second order admixture coefficient we find that only one term is non-zero, giving [152]

$$\tilde{A}_k^{(2)} = -\frac{\tilde{A}_k^{(0)}}{2} \sum_j \frac{V_{ij}(R)^2}{\Delta_{ij}^2}. \tag{5.15}$$

There are two important points to note about equation (5.15): the second order term is directly proportional to the unperturbed channel fractions, and the term is negative. The combination of these two points implies that the admixture of a channel will decrease in the perturbative region, in proportion to the amount of admixture of that channel at infinite separation.

The reason that the admixture of the channels always reduces is because the coupling to other pair states causes the eigenstates to gain some admixture of these intermediate dipole-coupled pair states. This is true of all atoms, of course, however the result in (5.15) shows that the individual channels have couplings with different R-variations. The different R-dependences of the different channels implies that the admixture of doubly excited perturbers in the Rydberg states is likely to become more prominent relative to the dominant channel for smaller values of R (although both will decrease). This in turn will affect the properties of the Rydberg states, for example the natural radiative lifetimes.

Despite the possible dramatic effects of the changing channel fractions with R, the actual difference to the wavefunctions induced by the dipole-dipole interactions is very small. Taking the example of the 16 ^{1}D$_2$ state where the state is composed of nearly equal parts singlet and triplet D character [61, 96] (and including the effect of Zeeman degeneracies), we find that in the region where the perturbative treatment just starts to break down ($R \sim 2000$ a.u.) the largest second order admixture coefficient is $A^{(2)} \sim 0.01$ in both the 5snd ^{1}D$_2$ and 5snd ^{3}D$_2$ channels; the other coefficients are an order of magnitude smaller. Thus the maximum change in the admixture of channels due to the dipole-dipole interactions in the perturbative regime is less then 10% of the overall admixture coefficient. The ratio $V_{ij}(R)/\Delta_{ij}$ will scale considerably with n: the $V_{ij}(R)$ coefficients scale as n^4 (as this is the product of two dipole matrix elements), and Δ_{ij} scales as n^{-3}. Bearing in mind the typical scaling of the admixture coefficients being $\sim n^{-3}$ (for series that are not too highly perturbed by many perturbers), the second-order admixture coefficients will scale as n^{11} (exactly like the C_6 coefficients).

5.2.3 C_6 Coefficients in Strontium D States

Due to the ^{1,3}D$_2$ states being the most highly perturbed Rydberg series in strontium, the series is likely to show the largest effect on the dipole-dipole interactions from the presence of perturbers and configuration mixing. We thus calculate the C_6 coefficients for these states, both to determine the validity of the one-electron model used in chapter 3 and to see what impact singlet-triplet transitions are likely to have on the interactions. For simplicity, we restrict ourselves to the stretched states, such that $J = M_J = 2$.

The results of the C_6 calculations for the ^{1}D$_2$ states are compared in figure 5.1 between the single-channel QDT and the MQDT methods. In the heavily perturbed regions the difference between the two calculations can be quite large, especially for states with heavy admixtures of perturbers. The largest effect is seen in the $n = 10$ and $n = 12$ levels, however several states around $n = 16$ also show significant differences between the calculations. The $n = 10$ level was found to have a larger natural width predicted by the MQDT calculation than the experimental values (as seen in chapter 4), so it is possible

that this state may be predicted to have too large an admixture of perturbers by the MQDT model. For the $n = 12$ level, the perturbers have a significant effect on the dipole matrix elements, causing the cancellations between levels to result in very different values when comparing the two calculations. The same intermediate pair states, however, contribute to the $n = 12$ state C_6 in both calculations. For the states around $n = 16$ the singlet-triplet mixing has a large effect, and the differences in the C_6 values for these states are due to different intermediate pair states contributing to the total C_6.

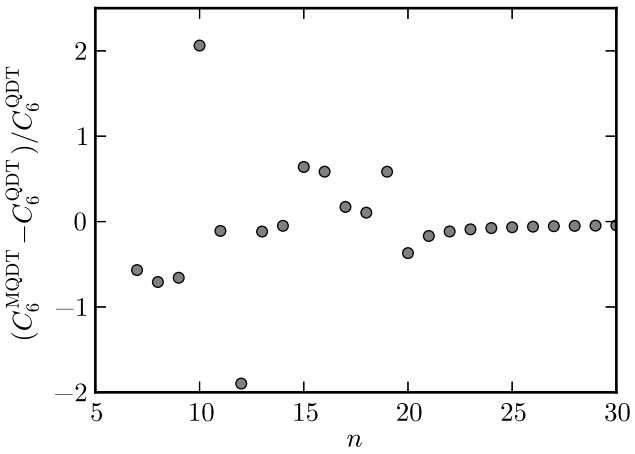

Figure 5.1: Fractional difference between the C_6 calculated using MQDT, C_6^{MQDT}, and the C_6 coefficient calculated using a single-channel quantum defect theory model, C_6^{QDT}, for the $^1\mathrm{D}_2$ states of strontium.

For higher values of n, the reduction of the perturber channel fractions ensures a convergence between the two calculations. For $n \geq 30$, the differences between the single-channel QDT and MQDT calculations are of the order of 2% and reduce with n. This difference is within the uncertainties of the C_6 coefficients calculated in chapter 4.3.

It is also useful to examine the contributions of the different intermediate pair states that make up the total C_6. Figure 5.2 shows the contributions from intermediate pair states of singlet-singlet, singlet-triplet and triplet-triplet symmetries for each value of C_6, which gives a good representation of the impact of singlet-triplet mixing on the dipole-dipole interactions. As expected, the heavily perturbed regions of the $^1\mathrm{D}_2$ and $^3\mathrm{D}_2$ states around $n = 16$ show the largest degree of singlet-triplet mixing, with significant

contributions from pair states of the opposite symmetry.

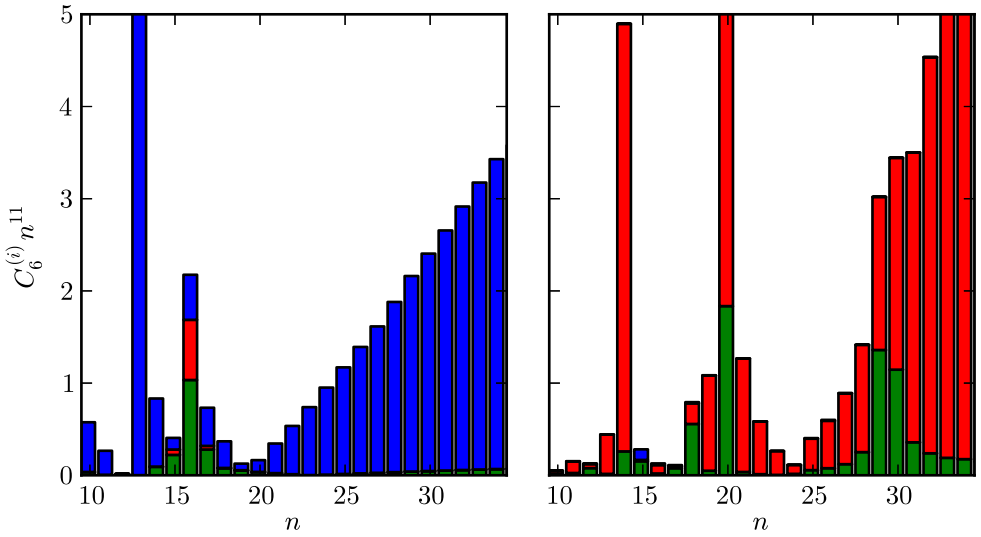

Figure 5.2: Scaled C_6 coefficients for the stretched states of the $^1D_2$ (left) and $^3D_2$ (right) states of strontium. Blue bars denote the contributions from the singlet-singlet intermediate pair states, green bars denote the contributions from the singlet-triplet states and red bars denote the contributions for the triplet-triplet states.

Figure 5.2 shows an additional feature of interest: a resonance feature can be seen in the singlet-triplet pair states contributing to the C_6 around the 30 $^3D_2$ state. Investigating this more closely, we find a Förster resonance (a near degeneracy between two pair states) in the $2\times n\,^3D_2 \rightarrow (n-2)\,^1F_3 + (n-3)\,^3F_2$ reaction channel. The Förster defect, $\Delta = E_i - E_j$, is shown in figure 5.3, demonstrating the zero-crossing on the denominator and hence the cause of the Förster resonance.

The resonance is, to the best of our knowledge, a unique feature of the strontium Rydberg states. While there exist many spin-changing Förster resonances in systems with strong spin-orbit coupling (for example quantum dots [153]), this is the first spin-changing resonance found in Rydberg atoms. At avoided crossings, it is possible to diabatically transfer states from one potential curve to another (for example in collisions), hence the Förster resonance in this case would allow significant transfer between pair states. Such state transfer has been previously observed around Förster res-

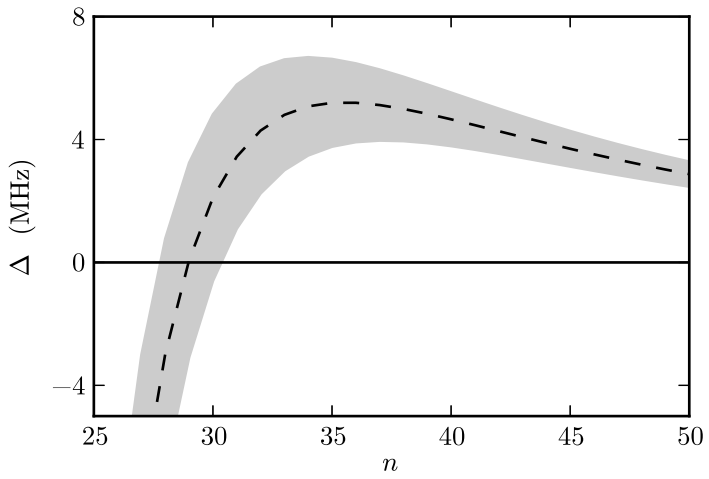

Figure 5.3: Förster defect, $\Delta = E_i - E_j$, between pair states for the $2 \times n\,^3\mathrm{D}_2 \rightarrow (n-2)\,^1\mathrm{F}_3 + (n-3)\,^3\mathrm{F}_3$ reaction channel. The shaded region denotes the uncertainties.

onances induced with electric fields [109]. The Förster resonance found in the 30 $^3\mathrm{D}_2$ state is thus a route to an electronic "spin-flip" induced by the the combined action of configuration mixing and dipole-dipole interactions. In the next section we apply this "spin-flip" to a study of spin excitations in a one-dimensional optical lattice.

5.3 Application of Spin Transfer to Optical Lattices

In condensed matter physics, the dynamics of one-dimensional chains of atoms is of critical importance to a large number of systems. In particular, Luttinger liquids have garnered a lot of interest [32, 154]; Luttinger liquids are a phenomenological model of low-energy one-dimensional excitations in fermions. The Luttinger liquid model condenses all of the relevant physics of one-dimensional excitations near a Fermi surface into two parameters, thereby greatly simplifying the understanding of one-dimensional systems. One of the key predictions of the one-dimensional Luttinger liquid model is the possibility of exciting different modes of the liquid corresponding to separate charge and spin modes [32, 154]. These different modes have different

dynamics (due to their different interactions), hence effectively separating out the spin and the charge excitations. Phrased differently, despite there being only one carrier for both charge and spin (either an electron or a hole), new quasiparticles arise in the system that appear distinct from the original charge and spin carrier. While we do not employ the Luttinger liquid model in this work, we show that the Förster resonance found in section 5.2.3 can lead to similar dynamics.

Cold atoms are increasingly being used to simulate condensed matter physics, due to the increasing experimental precision and the ability to control many degrees of freedom in cold atoms that cannot be manipulated in real crystals [155]. In particular, optical lattices are increasingly popular methods of investigating many-body dynamics in ultracold gases [156]. In this section, we investigate the dynamics of state transfer induced by dipole-dipole interactions. We focus on the spin-changing Förster resonance found in section 5.2.3, where we investigate the dynamics of Rydberg atoms prepared in a one-dimensional lattice. We begin with a general discussion of the dynamics induced by dipole-dipole interactions, before investigating the case of the lattice.

5.3.1 State Transfer Induced by Dipole-Dipole Interactions

When a Rydberg state is prepared and brought into the vicinity of another Rydberg atom, the interaction between the two atoms causes a shift in the energy levels. The eigenstate of the Hamiltonian of the atoms at infinite separation, however, is not the eigenstate of the Hamiltonian of the atoms interacting with a fixed, finite separation. The presence of dipole-dipole interactions will cause a small mixture of other pair states nearby in energy to the initial pair state, which in turn will cause oscillations between the states. As the dipole-dipole interaction is not time-dependent, the dynamics of the two interacting atoms is simply described by unitary time evolution.

We consider the Förster resonance in the $2 \times 30\,^3\mathrm{D}_2$ pair state. Figure 5.4 shows a non-perturbative calculation of the relevant energy levels and their

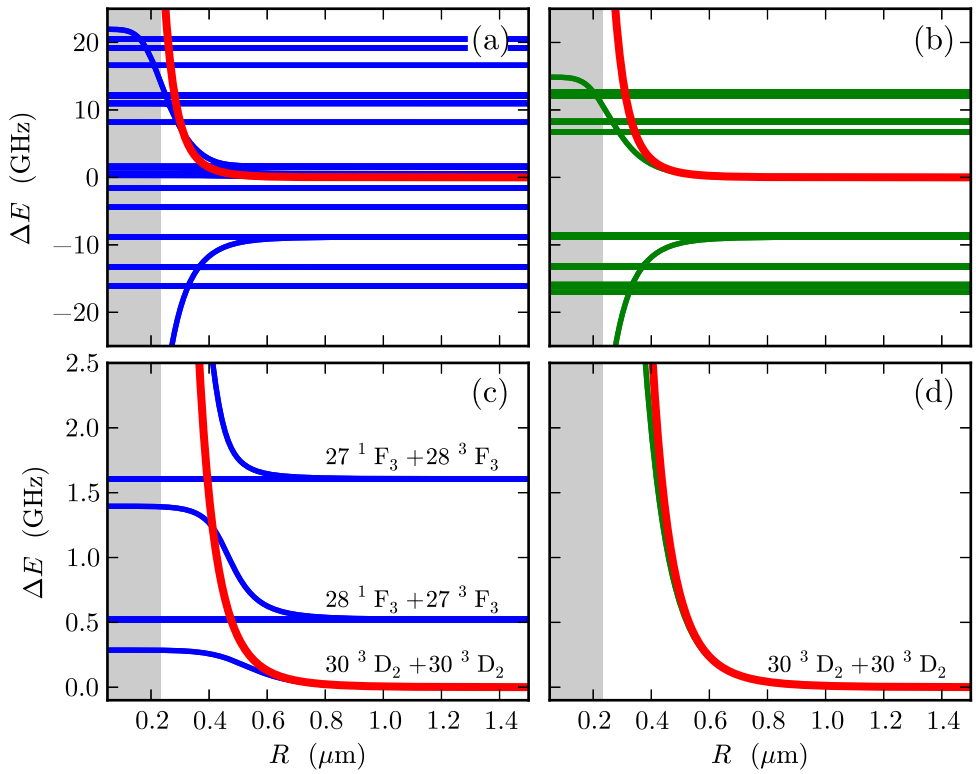

Figure 5.4: Energy levels in the vicinity of the $2 \times 30\,^3\mathrm{D}_2$ pair state of strontium with $\Omega = 4$ (corresponding to taking the values of $M_J = 2$ for the $30\,^3\mathrm{D}_2$ states), showing the avoided crossing with the Förster resonant state, $28\,^1\mathrm{F}_3 + 27\,^3\mathrm{F}_3$. The panels (a) and (c) show the multichannel calculation with the singlet-triplet pair states included, and panels (b) and (d) show the single channel calculation. Panels (a) and (b) are an overview of the energy levels, whereas (c) and (d) are zoomed in to show the avoided crossings. The red line overlaid on all the curves shows the C_6 perturbative result. The shaded areas denote the regions within the LeRoy radius.

avoided crossings as a function of the interatomic distance. The difference between the multichannel and the single channel calculations are also shown, reinforcing the importance of including the multichannel formalism when dealing with configuration-mixed states. The C_6 calculation is also shown to have a more limited range of applicability in the presence of avoided crossings, which occur at relatively large distances in the case of Förster resonances compared to other states in the $^3\mathrm{D}_2$ series (without going to much higher n). The second-order shift induced by the dipole-dipole interaction arises mostly

due to the coupling of the $2 \times 30\,^3\mathrm{D}_2$ with the $27\ ^3\mathrm{F}_3 + 28\ ^3\mathrm{F}_3$, visible in panels (a) and (b) of figure 5.4 as the downward curving state.

To describe the time evolution of the two interacting Rydberg atoms at a fixed distance R, it is a relatively simple matter to numerically evolve the states, as will be shown below. It is useful, however, to begin with a toy model to gain physical insight into the behaviour of the dynamics.

Toy Model

The simplest case we can consider for two interacting atoms is the two-level case. We consider two atoms initially prepared in one pair state with the dipole-dipole interactions induced by a nearby dipole-coupled pair state. We use the time-dependent Schrödinger equation,

$$i\frac{d}{dt}|\Psi\rangle = H|\Psi\rangle, \tag{5.16}$$

and we take $H = H_0 + V$, where H_0 denotes the Hamiltonian describing the atom pair states at infinite separation. Expanding the state vector in (5.16) in terms of the eigenstates of H_0,

$$|\Psi\rangle = \sum_i c_i(R,t)e^{-iE_it}|\psi_i\rangle, \tag{5.17}$$

we find the standard expression for the Schrödinger equation in the interaction picture,

$$\frac{dc_i}{dt} = -ic_j(R,t)V_{ij}(R)e^{-i\Delta_{ij}t}, \tag{5.18}$$

where $\Delta_{ij} = E_i - E_j$ is the Förster defect, and $V_{ij}(R)$ is given in (5.2). Considering two atoms fixed in space, and simplifying to a two level system we find

$$\frac{dc_1}{dt} = -ic_2(R,t)V_{12}(R)e^{-i\Delta_{12}t} \tag{5.19a}$$

$$\frac{dc_2}{dt} = -ic_1(R,t)V_{12}(R)e^{i\Delta_{12}t}. \tag{5.19b}$$

By differentiating with respect to time and substituting, we find the second order equation

$$\frac{d^2c_1}{dt^2} + i\Delta_{12}\frac{dc_1}{dt} + c_1(R,t)V_{12}(R) = 0. \tag{5.20}$$

The solution for this differential equation (assuming the boundary conditions $c_1(R,0) = 1$, $c_2(R,0) = 0$) is

$$c_1(R,t) = \frac{\Omega - \Delta_{12}}{2\Omega} e^{-i(\Delta_{12}+\Omega)t/2} + \frac{\Omega + \Delta_{12}}{2\Omega} e^{-i(\Delta_{12}-\Omega)t/2}, \tag{5.21}$$

where $\Omega^2 = \Delta_{12}^2 + 4V_{12}(R)^2$. This leads to an analogue of Rabi oscillations [157], where the probability of finding an atom in a dipole-coupled pair state at time t is given by

$$|c_2|^2 = \frac{4V_{12}(R)^2}{\Omega^2} \sin^2\left(\frac{\Omega t}{2}\right). \tag{5.22}$$

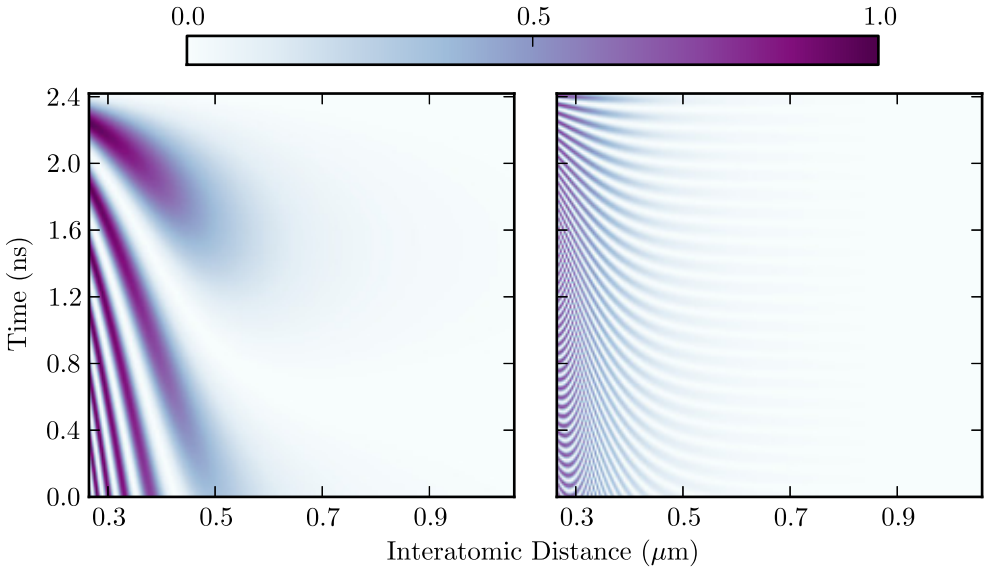

Figure 5.5: Probability of state transfer for a two-level pair state system due to dipole-dipole interactions, calculated using equation (5.22) with parameters for the $2 \times 30\,^3\mathrm{D}_2 \rightarrow 28\,^1\mathrm{F}_3 + 27\,^3\mathrm{F}_3$ reaction (left) and the $2 \times 30\,^3\mathrm{D}_2 \rightarrow 28\,^3\mathrm{F}_3 + 27\,^3\mathrm{F}_3$ (right).

The results of (5.22) are shown in figure 5.5 for the Förster resonant case and the case of the largest contributing pair state to the C_6 for the $30\,^3\mathrm{D}_2$ state. The values of the C_3 coefficients used to calculate $V_{12}(R)$ are given in appendix C. Despite the larger value of $V_{12}(R)$ for the $28\,^3\mathrm{F}_3 + 27\,^3\mathrm{F}_3$ shown in the right-hand plot, the probability of transferring from the $2 \times 30\,^3\mathrm{D}_2$ pair state to the $28\,^1\mathrm{F}_3 + 27\,^3\mathrm{F}_3$ pair state is much higher. The Förster defect is

shown to be much more important than the coupling strength in determining the probability of state transfer. The spin-forbidden reaction, $2 \times 30\,^3\mathrm{D}_2 \rightarrow 28\,^1\mathrm{F}_3 + 27\,^3\mathrm{F}_3$, is thus dominant over the $2 \times 30\,^3\mathrm{D}_2 \rightarrow 28\,^3\mathrm{F}_3 + 27\,^3\mathrm{F}_3$ transfer, despite the stronger coupling to the latter state.

Numerical Model

Despite the usefulness of equation (5.22) to gain physical insight into the state transfer mechanism, there remain several flaws. The first issue is that we have thus far ignored symmetrization; the off-diagonal couplings in the Hamiltonian mean that we should consider the linear combination of the $28\,^1\mathrm{F}_3 + 27\,^3\mathrm{F}_3$ and $27\,^3\mathrm{F}_3 + 28\,^1\mathrm{F}_3$ states. The second issue is that a two-level approximation will not necessarily be valid here, as the interference between the $28\,^1\mathrm{F}_3 + 27\,^3\mathrm{F}_3$ and $28\,^3\mathrm{F}_3 + 27\,^3\mathrm{F}_3$ channels may substantially alter the picture.

To resolve these issues, we change the expansion of the wavefunction in (5.16) to eigenstates of the full Hamiltonian, H. To do this, we diagonalize the matrix $H_{ij} = \langle\phi_j|H|\phi_i\rangle$, such that $\mathbf{D} = \mathbf{U} \cdot \mathbf{H} \cdot \mathbf{U}^T$, where $\mathbf{D}$ is a diagonal matrix of eigenvalues, $\mathbf{H}$ is the matrix with H_{ij} matrix elements, and $\mathbf{U}$ is a unitary matrix containing the eigenvectors. The initial state vector, $\underline{c}$ (where the vector is composed of the c_i coefficients in (5.17)) can then be projected into the eigenbasis, $\underline{C}$, using $\underline{C} = \mathbf{U} \cdot \underline{c}$, and the state evolved in time using

$$|\Psi\rangle = \sum_i C_i(R,t)|\phi_i\rangle = \sum_i e^{-i\epsilon_i t} C_i(R,0)|\phi_i\rangle, \tag{5.23}$$

where $|\phi_i\rangle$ are eigenstates of the full Hamiltonian and the ϵ_i are the corresponding eigenenergies. The expression for the time evolution in (5.23) is valid only because V is time independent. As such, the time evolution of the eigenstates is completely determined by the exponential factor, $e^{-i\epsilon_i t}$, thus simplifying the procedure of solving equation (5.18). Instead, the difficulty now lies in finding the eigenstates, ϕ_i, and their eigenvectors. After the time evolution, the state vectors are projected back into the original basis by applying $\underline{c} = \mathbf{U}^T\underline{C}$.

Numerically, the diagonalization of large matrices can be done with relative ease, using packages such as the LAPACK and ATLAS libraries [158, 159].

The computing time of these algorithms allow for much faster processing than directly solving (5.18). The drawback of these algorithms, however, is that the ordering of the eigenvalues and eigenvectors is not preserved as the independent variable (in this case, R) is varied. As such, the states often switch at true crossings of the potential curves (note that true crossings only occur between states of different symmetry [160]). To overcome this, it is necessary to track the eigenvectors and ensure their ordering is preserved. The ordering can be checked by ensuring the eigenvectors, $\underline{C}_i(R)$, are orthogonal, such that $\underline{C}_i(R) \cdot \underline{C}_j(R+dR) = \delta_{ij}$. For small enough values of the step size, dR, this is sufficient to give accurate tracking of the eigenvectors, with the caveat that the algorithm must be started for large enough values of R to ensure the correct eigenvector is chosen as the starting state.

We note that the state tracking procedure detailed above depends crucially on the knowledge of the calculated eigenvectors. Unfortunately, many of the eigenvalues of the Hamiltonian are degenerate when using double precision arithmetic. The eigenvectors resulting from degenerate eigenvalues are in general not uniquely defined, hence the orthogonality condition of the numerical eigenvectors for different values of R is not met. We therefore use quadruple precision arithmetic to enable the accurate tracking of the eigenstates.

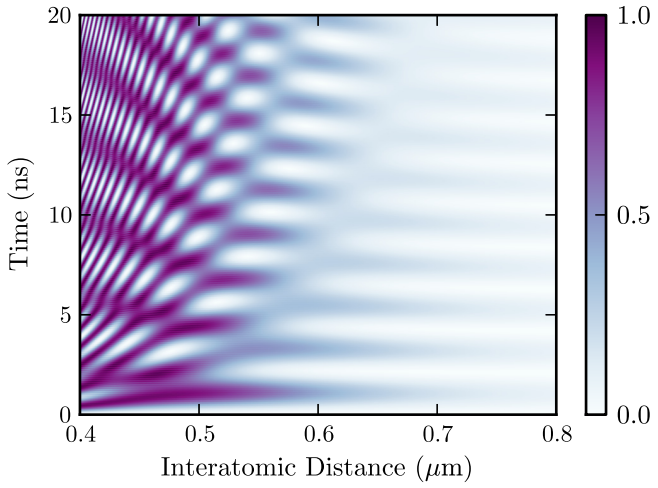

Figure 5.6: Probability of transferring to the 28 ^{1}F$_3$+27 ^{3}F$_3$ state for a two atom system with four levels per atom, calculated by time-evolution of the eigenstate basis using (5.23).

Figure 5.6 shows the results of the time evolution of the eigenstates from (5.23). In the simulation we have included the 30 $^3D_2$, 28 $^1F_3$, 27 $^3F_3$ and 28 $^3F_3$ states. We have ignored the M_J sublevels, choosing the $M_J = 2$ for all states included (which corresponds to taking the largest value of $V_{12}(R)$). The different M_J sublevels would make very little difference to the results in figure 5.6, in principle, as the potential energy curves are unlikely to split by large amounts between the different symmetries (which would only be seen in the F states, as we initially chose the stretched states of the 30 $^3D_2$ atoms). We also ignore the 27 $^1F_3$ state; despite the potentially large effect of the 27 $^1F_3$ + 28 $^3F_3$ pair state (as seen in figure 5.4), the dynamics in terms of the spin angular momentum will largely be the same, and it is these dynamics that we are interested in. The potential curves resulting from the inclusion of these four levels are shown in figure 5.7. Comparing the curves in figures 5.4 and 5.7, we see that the main behaviour of the eigenstates is reproduced despite only including four energy levels per atom. While the inclusion of more states would be interesting, the calculation times become quickly prohibitive when adding states due to the increasing basis size when considering more than two atoms, as will be seen in section 5.3.2.

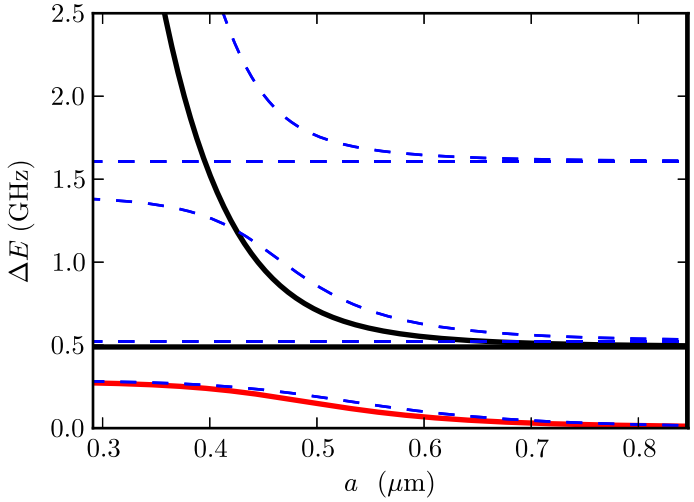

Figure 5.7: Potential curves around the 2×30 $^3D_2$ pair state (red line), including only the $M_J = 2$ sub-levels of the 30 $^3D_2$, 28 $^1F_3$, 27 $^3F_3$ and 28 $^3F_3$ states. Black solid lines denote the 28 $^1F_3$ + 27 $^3F_3$ pair state in the four-level calculation, and the blue dashed lines are the results of the full non-perturbative calculation shown in figure 5.4.

The results in figure 5.6 confirm the conclusions of the toy model, namely that the dynamics of the $2 \times 30\,^3\mathrm{D}_2 \rightarrow 28\,^1\mathrm{F}_3 + 27\,^3\mathrm{F}_3$ reaction dominates over the $2 \times 30\,^3\mathrm{D}_2 \rightarrow 28\,^3\mathrm{F}_3 + 27\,^3\mathrm{F}_3$ reaction. Interference effects, however, are visible.

5.3.2 Spin Transport in Strontium Rydberg Lattices

In the preceding section, we demonstrated that two strontium atoms in the $30\,^3\mathrm{D}_2$ state interacting via the dipole-dipole interaction can change state to a spin-forbidden state, a transition enhanced by the near degeneracy of the $28\,^1\mathrm{F}_3 + 27\,^3\mathrm{F}_3$ pair state to the original $2 \times 30\,^3\mathrm{D}_2$ state. This "ringing" effect, however, would be difficult to measure experimentally, due to the difficulty of preparing the initial states in the eigenstates of H_0 and not of the full Hamiltonian H (using the same definitions of H_0 and H as chapter 3, equation (3.1)).

A more interesting situation would be to investigate the propagation of a spin excitation along a chain of atoms, where the atoms trapped in a Mott insulator state [161] (i.e. a deep enough lattice trap that there would be a single atom per lattice site, making the statistics of the atoms unimportant). An interface between $^1\mathrm{F}_3$ states and $^3\mathrm{D}_2$ states would allow resonant hopping of the states, leading to dynamics that are analogous to spin-hopping in condensed matter systems [161].

The formalism used to calculate figure 5.6 can be generalized to N atoms. The number of basis states required to describe N atoms with four levels each is 4^N, and as the time taken to diagonalize square matrices scales as the cube of the number of basis states, adding a single atom means the procedure takes 64 times the amount of time. Due to this severe exponential scaling, we are limited in the number of atoms we can simulate, with $N = 5$ being enough to take several days to calculate.

For a spin chain of atoms, the Hamiltonian can be written as

$$H = \sum_p H_0^{(p)} + \sum_{p<q} \sum_{i,j} V_{pq}^{ij}(R_{pq}) \left[|\phi_{pi}\phi_{qi}\rangle\langle\phi_{pj}\phi_{qj}| + |\phi_{qi}\phi_{pi}\rangle\langle\phi_{qj}\phi_{pj}| \right], \quad (5.24)$$

where $|\phi_{pi}\phi_{qi}\rangle$ is the state vector of the pair of atoms at lattice sites p and

q in the pair state i, $R_{pq} = a|p-q|$ (with a being the spacing between the lattice sites), $H_0^{(p)}$ is the single atom Hamiltonian such that $H_0^{(p)}|\phi_{pi}\rangle = E_i|\phi_{pi}\rangle$ (where $|\phi_{pi}\rangle$ is a single-atom state vector, with $|\phi_{pi}\phi_{qi}\rangle \equiv |\phi_{pi}\rangle|\phi_{qi}\rangle$), and V_{pq}^{ij} is the dipole-dipole interaction between pair states i and j given in (5.2), with $R = R_{pq}$. The values for V_{pq}^{ij} can all be found in appendix C. The (unsymmetrized) wavefunction in (5.18), $|\Psi\rangle$, can then be written as a product of the N atom wavefunctions,

$$|\Psi\rangle = \sum_i c_i(a,t) \prod_{p=1}^{N} |\phi_{pi}\rangle. \tag{5.25}$$

As before, this is projected onto the basis of eigenstates of H where the time evolution is simple, before being projected back into the original basis. To simplify the discussion, we introduce the following short-hand: $30\ ^3\mathrm{D}_2 \equiv |0\rangle$, $28\ ^1\mathrm{F}_3 \equiv |1\rangle$, $27\ ^3\mathrm{F}_3 \equiv |2\rangle$ and $28\ ^3\mathrm{F}_3 \equiv |3\rangle$. We then define the expectation value of the spin and total angular momentum quantum numbers as being, respectively,

$$\langle S\rangle = \sum_i S_i |c_i(a,t)|^2, \tag{5.26a}$$

$$\langle J\rangle = \sum_i J_i |c_i(a,t)|^2, \tag{5.26b}$$

where S_i and J_i are the spin and total angular momentum quantum numbers for state i respectively.

The expectation value of the spin quantum number is shown in figure 5.8 for an initial state of $|1000\rangle$, with a lattice spacing of 775 nm (the spacing given when employing a commonly used telecommunications laser at 1550 nm; see for example [162]). The propagation of the spin singlet state is clearly visible along the chain, with a reflection from the final atom. The spin wave is not absolutely perfect along the lattice as all the interactions between the atoms are taken into account, not just the nearest-neighbours; additionally, the second-order couplings (those that give rise to the C_6/R^6 energy shifts) also induce state oscillations. The waves are seen to propagate on short timescales; adding more atoms to the chain would lengthen the travel time to reach the final atom, or alternatively the lattice spacing could be increased.

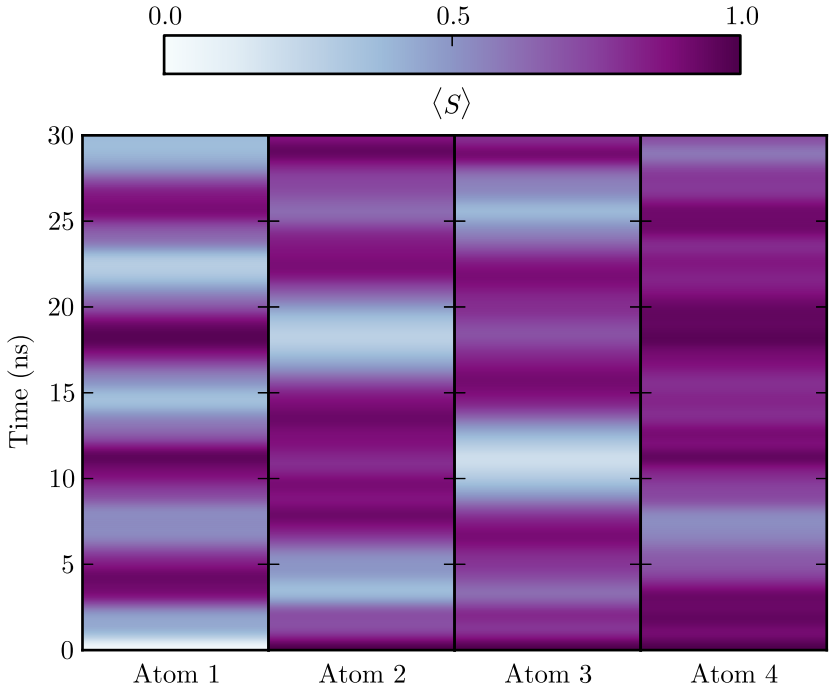

Figure 5.8: Expectation value of the spin in a four-atom spin chain, initially prepared in the $|1000\rangle$ state (see the text for an explanation of the short-hand notation) with lattice spacing of $a = 775$ nm.

We note that neither the spin nor the total angular momentum are good quantum numbers. In the case of the spin, the coupling with the orbital angular momentum and configuration mixing both contribute to the lack of conservation. For the total angular momentum, it is the mixing between pair states that are close in energy that transfers angular momentum to energy; this is particularly true near avoided crossings. Neither the sum of the values of S nor the sum of the values of J are constant in time.

Spin-Charge Separation

When calculating the potential curves for the N-atom case, the energy levels can be seen to arrange themselves in bands. The minimum energy separation between two energy levels for infinite lattice spacings is given by the Förster defect of the Förster resonant states, which in this case is 513 MHz. The calculated potential curves are shown in figure 5.9, where an avoided crossing can be seen between the $|1000\rangle$ state and the $|1120\rangle$ state. The avoided

crossing happens for $N > 4$, where the 4-atom case constitutes the minimum number of atoms required.

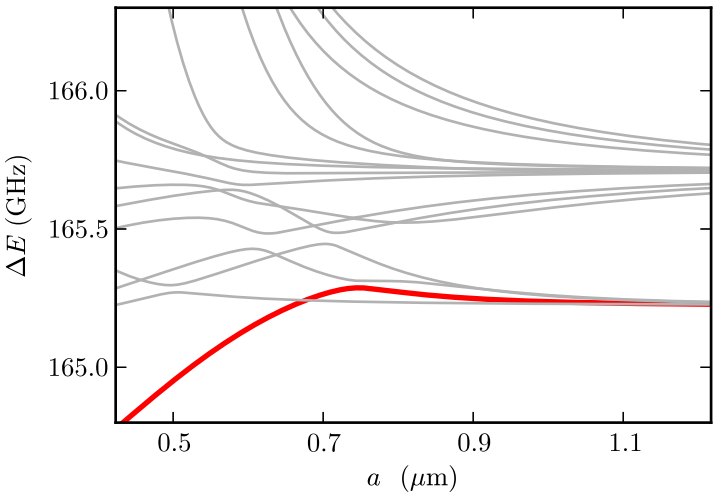

Figure 5.9: Potential curves for four atoms in a lattice, centred around the $|1000\rangle$ state (shown in red).

The avoided crossing seen in figure 5.9 modifies the dynamics in that region dramatically. When two states have an avoided crossing, the resulting eigenstate is a superposition of the two bare states; in the case depicted in figure 5.9, this leads to an admixture of $^3\mathrm{F}_3$ character into the resonant dynamics. The result is that the spin and total angular momentum decouple, and an analogy of spin-charge separation is observed (we use "charge" as an analogy for total angular momentum, in a similar way to [163]). The separation of the spin and angular momentum is shown in figure 5.10, where the probability of being in a singlet state and the probability of being in a $J = 3$ state are no longer the same, despite starting from a $^1\mathrm{F}_3$ spin defect. The effect is a maximum around the avoided crossing.

The system is reminiscent of one-dimensional Luttinger liquids, where the onset of spin-charge separation arises from the different couplings of the spin and charge modes. The simulation of spin-charge separation has previously been proposed in a cold atom system by mapping spin and charge onto internal atomic states and atomic mass density respectively, and then driving transitions in the atoms using laser light [163]. The system in strontium, however, does not need to be driven; the phenomenon of spin-charge beating

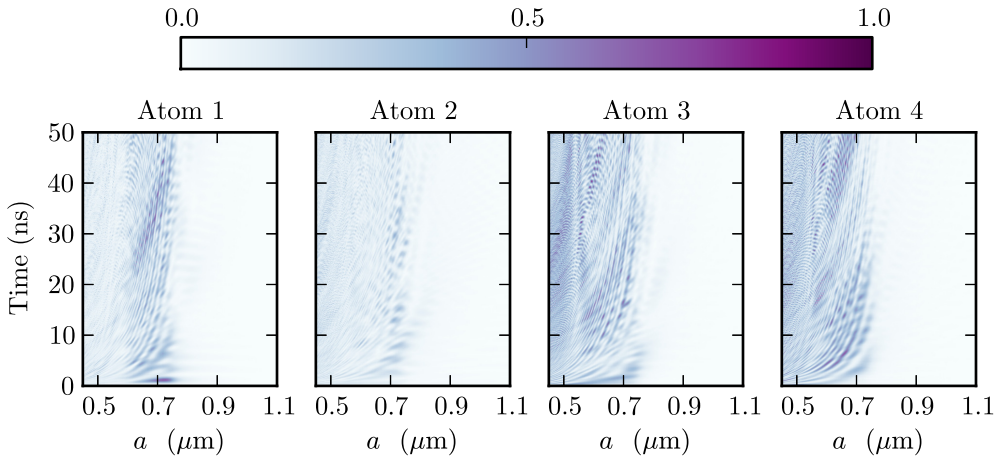

Figure 5.10: Absolute difference between the probability of each atom being in a singlet state and the probability of each atom being in a $J = 3$ state, $|P(S = 0) - P(J = 3)|$, as functions of time and lattice spacing, a. Each subplot represents an atom in a chain of four atoms, initially prepared in a $|1000\rangle$ state.

should arise "simply" by preparing a one-dimensional lattice of strontium Rydberg atoms.

External Field Control

Currently, the major disadvantage of the spin-charge separation observed in the previous section is that the period of the oscillations is very small, making the observation of the spin-charge separation experimentally challenging. The period of the oscillations is set by the energy separation between the $|1000\rangle$ and $|1120\rangle$ states, although other states can play a complicated role in determining these oscillations. It is possible, however, to slow these oscillations down by judicious application of magnetic and electric fields to shift the energy of the states. The resulting smaller energy separations would thus lead to longer oscillation periods. The ability to tune these energies would also be a significant advantage for the experimental realization of the lattice, as the lattice spacing is much more difficult to tune than an external field.

In order to tune the energy levels, three different types of fields could be applied: a magnetic field, a static electric field or an AC electric field applied in the form of microwaves. As mentioned above, the presence of the avoided

crossing is entirely set by the Förster defect of the $2\times30\,^3\mathrm{D}_2 \rightarrow 28\,^1\mathrm{F}_3+27\,^3\mathrm{F}_3$ reaction. By tuning this Förster defect, the avoided crossing can thus be shifted in and out of resonance for a fixed value of the lattice spacing.

For the magnetic and static electric fields we assume the shifts will arise from the linear Zeeman ($\Delta E_B = g_J\mu_\mathrm{B}M_J B$, where ΔE_B is the Zeeman shift, g_J is the Landé factor, B is the magnetic field and μ_B is the Bohr magneton [23]) and quadratic Stark shifts ($\Delta E_\mathcal{E} = -\alpha\mathcal{E}^2/2$, where $\Delta E_\mathcal{E}$ is the Stark shift, α is the static polarizability of the state and $\mathcal{E}$ is the electric field [23]) respectively. Writing the difference between the shifts of the $2\times30\,^3\mathrm{D}_2$ and the $28\,^1\mathrm{F}_3+27\,^3\mathrm{F}_3$ as $\Delta_{B,\mathcal{E}} = 2\Delta E_{B,\mathcal{E}}(30\,^3\mathrm{D}_2) - \Delta E_{B,\mathcal{E}}(28\,^1\mathrm{F}_3) - \Delta E_{B,\mathcal{E}}(27\,^3\mathrm{F}_3)$, we determine that the magnetic field required to compensate the Förster defect is about 730 G. The static polarizabilities, calculated using the semiclassical method of section 2.4.1, mean that electric fields shift the energy levels in the opposite directions, hence the static electric fields can only increase the Förster defect. The Landé g_J-factors and the static polarizabilities of the relevant states are shown in table 5.1.

State	Landé g_J-factor	Static Polarizability
$30\,^3\mathrm{D}_2$	7/6	-7.31×10^9 a.u.
$28\,^1\mathrm{F}_3$	1	2.00×10^{10} a.u.
$27\,^3\mathrm{F}_3$	13/12	7.18×10^{10} a.u.

Table 5.1: Landé g_J factors and static polarizabilities for the $2\times30\,^3\mathrm{D}_2 \rightarrow 28\,^1\mathrm{F}_3+27\,^3\mathrm{F}_3$ resonance. The g_J-factors are determined using the Landé formula in (4.24), and the polarizabilities are calculated using the semiclassical approximation of section 2.4.1.

A magnetic field of 730 G can be achieved, however this would be experimentally very challenging in a cold atom experiment. By driving a transition with microwaves off-resonantly, the light shift can be engineered to shift just the $30\,^3\mathrm{D}_2$ level while introducing a minimum amount of additional admixture of another atomic state.

For a single microwave transition where the states are far apart in energy, a two-level description is sufficient to describe the effect of the coupling; we also use the rotating-wave approximation, which we have checked is valid in

this case [23, 157]. For a transition with frequency ω_0, with detuning Δ_{mw}, and a Rabi frequency Ω, the light shift for large detuning is given by [157]

$$\Delta E_{\text{light}} \approx \frac{\Omega^2}{4\Delta_{\text{mw}}}. \tag{5.27}$$

The response of a two-level system irradiated with a monochromatic light field is to oscillate between the two levels. The amplitude of these oscillations is given by [157]

$$P_{\text{max}} = \frac{\Omega^2}{\Omega^2 + \Delta_{\text{mw}}^2}. \tag{5.28}$$

If we require that P_{max} never go above a certain fraction, a_{max}, in order to not significantly populate unwanted states, then we can combine equations (5.27) and (5.28) to obtain

$$\Omega = 4\Delta E_{\text{mw}} \sqrt{\frac{|a_{\text{max}} - 1|}{a_{\text{max}}}}, \tag{5.29a}$$

$$\Delta_{\text{mw}} = 4\Delta E_{\text{mw}} \frac{|a_{\text{max}} - 1|}{a_{\text{max}}}. \tag{5.29b}$$

The conditions in (5.29) therefore enables the creation of any light shift (provided the detuning is large but not comparable to the transition frequency) without admixture of another state that could destroy the dynamics of the spin transport experiment. The specific transitions chosen for engineering these light shifts will depend on the apparatus available to experimenters, however we note the presence of the 30 ^{1}P$_1$ state 34 GHz away from the 30 ^{3}D$_2$ that could be suitable (the dipole moment of this transition is calculated to be -132 a.u.).

By targeted shifting of the 30 ^{3}D$_2$ state, we find that the position of the avoided crossing can be tuned. The resulting dynamics are shown in figure 5.11 as a function of time and light shift, and in figure 5.12 as a function of time for a light shift of $\Delta E_{\text{light}} = 200$MHz. The spin-charge separation is shown to occur on time scales that are about an order of magnitude slower than those in figure 5.10. The dynamics can be slowed down further by increasing the lattice spacing, although the time scales will start to reach a fixed limit and the contrast of the spin-charge separation is likely to decrease. Unfortunately the spin-charge separation becomes weaker from atom to atom as the lattice spacing is increased, so it may be preferable to work at

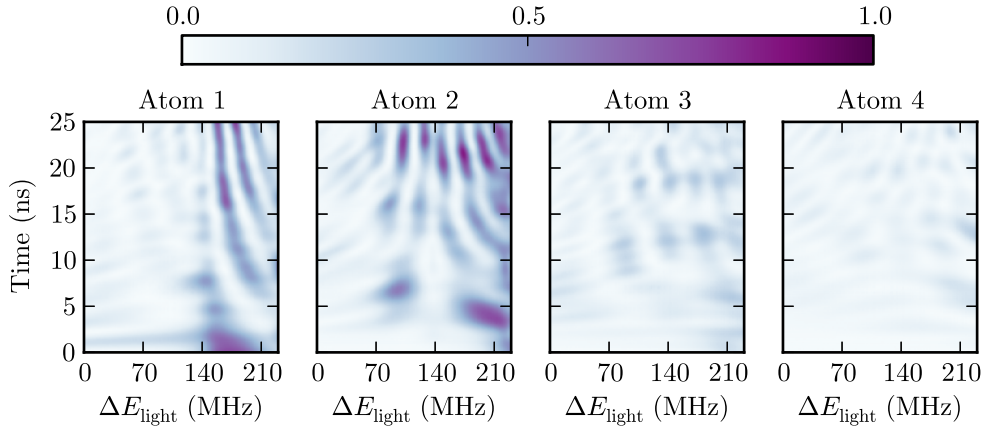

Figure 5.11: Difference between the probability of each atom being in a singlet state and the probability of each atom being in a $J = 3$ state, $|P(S = 0) - P(J = 3)|$, as functions of time and light shift due to the applied microwave field. Each subplot represents an atom in a chain of four atoms, initially prepared in a $|1000\rangle$ state with a lattice spacing of $a = 775$ nm.

smaller lattice spacings for the experimental observation of the spin-charge separation dynamics.

5.3.3 Outlook

In the preceding section we have elucidated some of the internal state dynamics of four atoms in a spin chain. These Rydberg lattice dynamics are interesting, but a concrete link to other physical systems remains to be drawn. Here we briefly discuss the potential implications of the work discussed in this chapter, highlighting possible future directions for the research.

In condensed matter systems, a spin excitation (where the electromagnetic field from the crystal splits the spin states, allowing well defined spin-up and spin-down states) can propagate along a lattice, causing decoherence in ferromagnets [161]. The quantized spin waves are known as magnons, and their control has large implications in applied fields of physics such as spintronics [164]. Luttinger liquids can also be linked to spin excitations, as the Luttinger liquid paradigm can be applied to the case of interacting spins in a chain [32]. Magnons are thus found to be a specific case of Luttinger

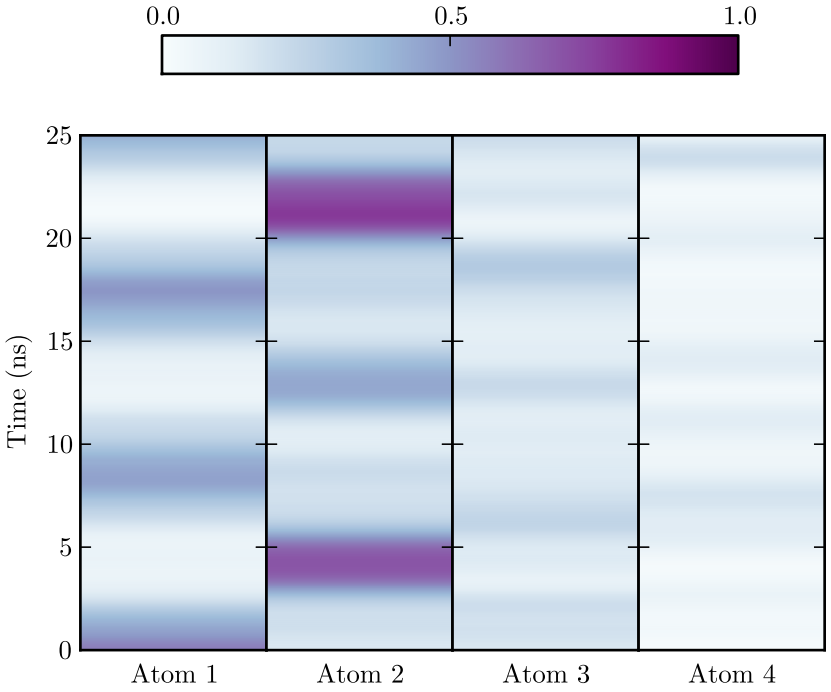

Figure 5.12: Difference between the probability of each atom being in a singlet state and the probability of each atom being in a $J = 3$ state, $|P(S = 0) - P(J = 3)|$, as functions of time with an applied microwave field causing a light shift of 200 MHz. Each subplot represents an atom in a chain of four atoms, initially prepared in a $|1000\rangle$ state with a lattice spacing of $a = 775$ nm.

liquid theory, which is still a very active research field [154].

In our system, the crystal field could be thought of as arising from the inner electron (giving rise to the splitting between singlet and triplet states), and the propagation of spin could potentially provide a direct simulation of spin waves in a cold atom system (where most cold atom spin wave simulations involve mapping the spin onto other internal degrees of freedom). The ability to tune the energy levels using microwaves also leads to the possibility of linking the one-dimensional Rydberg lattice to Luttinger liquid formalism, which could yield new insights into one-dimensional Fermi liquids. In order to make the link with Luttinger liquids, the Hamiltonian of the four-atom spin chain must be either mapped onto a similar system that has already been solved, or the Hamiltonian must be solved analytically.

Other possible directions for the research include the study of Förster reso-

nant systems. Förster resonances are commonly used in techniques such as Förster resonant energy transfer (FRET), as used in quantum dot technology [153] and in molecular imaging technology [150]. The understanding of the dynamics of Förster resonances are crucial to experiments making use of FRET, and the possibility of configuration-mixing in the internal states of molecules could be detrimental to experiments when applying the FRET technique. The dynamics of the Rydberg spin chains considered in this work would therefore have to be applied to similar conditions than those found in FRET experiments, in order to make the relevance of our results more applicable to the wider community.

5.4 Conclusions

We have investigated the impact of two-electron effects on the dipole-dipole interactions of strontium. We find the effect of perturbers to be negligible, however the singlet-triplet mixing found in the $^{1,3}\mathrm{D}_2$ states can have a noticeable impact, particularly in states with high admixture coefficients or in pair states where there is a near degeneracy with another pair state (Förster resonances). The dipole-dipole interaction, however, does not have a significant impact on the admixture of the perturbers.

We also identify the presence of a Förster resonance in the $^3\mathrm{D}_2$ states that is due to a dipole-forbidden, spin-changing coupling in the $2 \times n\,^3\mathrm{D}_2 \rightarrow (n-2)\,^1\mathrm{F}_3 + (n-3)\,^3\mathrm{F}_2$ channel. We have studied the possibility of observing a spin-changing transition due to the dipole-dipole interaction for the $30\,^3\mathrm{D}_2$ state and conclude that the transition probability becomes high when the interatomic spacing is of the order of 500 nm.

By extending the investigation to a chain of four atoms in a lattice, we have calculated the expectation values of the spin and total angular momentum quantum numbers as they evolve in time. We find spin waves and total angular momentum waves that propagate through the lattice due to the coupling to the $^1\mathrm{F}_3$ state in the atoms. We also find that the spin waves and angular momentum waves can decouple due to the presence of an avoided crossing in the potential curves, such that spin-charge separation (where the

quantum number J is used as an analogue for charge) naturally arises in a one-dimensional optical lattice of strontium Rydberg atoms. The spin-charge separation phenomenon is similar to the case of Luttinger liquids, and is of interest to the ultracold atom community [163]. For a fixed lattice spacing, it is also possible to tune the avoided crossing using microwave fields, leading to the possibility of controllably switching between spin transport and spin-charge separation through a chain of Rydberg atoms.

Chapter 6

Conclusions

In this thesis, we have presented calculations relating to the physical properties of the Rydberg states of strontium, including the investigation of two-electron effects. Specifically, the investigation of long-range interactions were the focus of the calculations, to supplement the experimental efforts of the strontium group in Durham [22, 145]. Long-range interactions lead to the dipole blockade effect for high enough densities of Rydberg gases [9], an effect which has uses in topics such as quantum optics [103], quantum entanglement [80] and quantum information [3, 10], driving recent interest in Rydberg atoms. Other motivations involving quantum many-body physics were also detailed in the introduction chapter, where novel states of matter can be created by exploiting the strong dipole-dipole interactions and the long lifetimes of Rydberg states [82, 83]. Finally, a more technical motivation was present: the investigation of the validity of the single active electron model in two-electron Rydberg atoms, which has been previously applied with good success [22, 114].

Chapter 2 was devoted to developing the single active electron model for the various calculations of the physical properties of Rydberg atoms. Specifically, different methods for calculating dipole matrix elements (which characterize the strength of atomic transitions) were presented. For Rydberg state to Rydberg state transitions, either the semiclassical approximation [28, 41, 43, 44] or quantum defect theory [34, 45, 49, 165] can be used in the calculation of the radial dipole matrix elements. Dipole matrix elements involving either

a ground state or low-excited state to Rydberg state transition can be calculated with quantum defect theory (the semiclassical approximation is not valid for low-n). We apply these methods to the calculation of the natural radiative lifetimes of rubidium (the most closely related one-electron atom to strontium), and find excellent agreement between the calculations from quantum defect theory and experimental values [78].

The calculation of long-range interactions was presented in the chapter 3, which made use of the methods in chapter 1. Using the one active electron model, we presented calculations of dipole-dipole and quadrupole-quadrupole interactions in calcium, rubidium, strontium, caesium and ytterbium Rydberg atoms. Two methods of calculation were presented, the perturbative and non-perturbative methods; this chapter focused mainly on the perturbative treatment, as this allowed a consistent survey of all the series in the three atoms studied where energy levels were available. The main conclusions of this chapter were that the details of the dipole-dipole interactions strongly depended on the atom and the series being studied. Quadrupole-quadrupole interactions were usually negligible compared to the dipole-dipole interactions, except for cases where the dipole-dipole interactions were unusually small (known as Förster zero states). A number of Förster resonances (near-degeneracies between pair states causing resonances in the dipole-dipole interactions) were found in strontium triplet states, as well as in both rubidium and caesium; no Förster resonances were found in calcium and ytterbium. Finally, the S states of strontium proved to be particularly interesting as the singlet series were found to be the only series to have isotropically attractive interactions. These isotropically attractive interactions may be critical for self-focusing non-linear optics schemes [103] and generating quantum many body entangled states [12].

The calculations of long-range interactions in chapter 3 were performed for principal quantum numbers above $n = 30$, where the effects of the second electron are expected to be small. The purpose of chapter 4 was to elucidate the role of the second electron in determining various physical properties of the Rydberg states of strontium. To investigate the effects of the second electron, we employed multichannel quantum defect theory, the formalism of which we review at the beginning of chapter 4. In particular, we derive the

K matrix, known as the reactance matrix, and we show its use in numerical studies of Rydberg series perturbed by doubly excited states. By fitting the reactance matrix such that the models reproduce the experimentally determined bound state energy levels, a description of the perturbations in all series of strontium for $L \leq 3$ was found. These models were compared to previous work, and found that most of these agreed very well with these previous studies [61, 128]. For certain series, the more recent experimental data used revealed new information about the perturbations of the series, for example in the $^1S_0$ states where the small uncertainties allowed the identification of different fine-structure components of the $4d^2$ perturbers. Finally, using the new MQDT models developed in chapter 4, we incorporate the multichannel formalism into the calculation of dipole matrix elements, which we use to investigate the radiative lifetimes of perturbed Rydberg states of strontium. The perturbations were found to have a large effect on the lifetimes, causing a reduction of the $^1D_2$ state lifetimes in strontium by an order of magnitude compared to the ^2D state lifetimes in rubidium, thereby emphasizing the importance of including these two-electron effects in these calculations.

In the final chapter, we combine the two-electron MQDT formalism with the description of dipole-dipole interactions derived in chapter 3. We focus on the most heavily perturbed series, the $^{1,3}D_2$ states, where the 4d6s configuration causes singlet-triplet mixing of the Rydberg states. We find that the C_6 coefficients describing the second-order dipole-dipole interactions change very little for high-n (the changes are to within the error of the C_6 coefficients calculated in chapter 3), however for lower n larger deviations are found. Interestingly, a Förster resonance is found in the $^3D_2$ series which constitutes a spin-forbidden transition. We investigate the possible dynamics of this spin-forbidden transition, first limiting the number of atoms to only two before extending this to four atoms. Oscillations between the states are found, and when the spin and total angular momentum expectation values are investigated, spin-charge separation is found to occur for smaller values of the lattice spacing. At higher values of the lattice spacing, spin transport is seen in the system; this is the first time a real spin wave has been predicted in a lattice of cold atoms (usually, the spin is mapped to an internal state of the atom [163]). In the context of one dimensional Fermi gases, the spin-

charge separation is a hallmark feature of Luttinger liquids, a widely used and investigated model for interacting 1D gases [154].

Finally, we wish to emphasize the context of the work in cold, Rydberg atoms. The calculations of dipole matrix elements have been investigated for more than fifty years, however many studies are incomplete. Alkali atoms, which are widely used in the field of Rydberg atoms [3], can now be easily described numerically, in large part thanks to advances in computational resources. Alkaline-earth atoms, however, have yet to be explored in the same detail as the alkali atoms. The work presented in this thesis is a step towards the complete description of these alkaline-earth atoms. Alkaline-earth atoms could present significant advantages over alkali atoms for certain applications such as Rydberg dressing [26], and the use of these atoms in the wider atomic physics community is slowly increasing (see for example [166, 167]). It is hoped that as alkaline-earth atoms see more and more widespread use, the work done in this thesis will prove a boon to the future endeavours of researchers in the field.

Appendix A

Angular Factors

In the calculations of dipole matrix elements, it is convenient to split the matrix elements of the dipole operator into angular and radial parts. Explicitly, the dipole matrix element between a state $|nlLSJM_J\rangle$ and another state $|n'l'L'S'J'M_{J'}\rangle$ can be written

$$\langle n'L'S'J'M_{J'}|\underline{r}|nLSJM_J\rangle = \langle L'S'J'M_{J'}|\hat{r}|LSJM_J\rangle\langle n'l'|r|nl\rangle, \qquad \text{(A.0.1)}$$

where $\hat{r}$ denotes the angular part of the position operator and r denotes the radial part. We have also used the convention that upper case letters denote the coupled atomic quantum numbers and the lower case letters denote the electronic quantum numbers.

In this appendix, we derive the angular dipole matrix elements, $\langle L'S'J'M_{J'}|\hat{r}|LSJM_J\rangle$, used in various parts of the thesis. We write $\underline{r}$ in terms of its spherical components, r_p, where

$$r_p = r\sqrt{\frac{4\pi}{3}}\sum_{p=-1}^{1} Y_{1,p}, \qquad \text{(A.0.2)}$$

where $Y_{k,p}$ is a spherical harmonic. The expression for higher order multipoles is more complicated.

A.1 Single Atom Transitions for Singly Excited States

To derive the single atom angular dipole matrix element for singly excited states, we must assume that all core electrons (whether there is a valence electron included in the core or not) carry no orbital angular momentum. We write our original state as $|nll_{\mathrm{c}}Lss_{\mathrm{c}}SJM_J\rangle$, where upper case letters denote coupled atomic angular momenta, lower case letters denote electronic angular momenta and the subscript c denotes the angular momentum carried by the core. The orbital part of the core angular momentum is $l_{\mathrm{c}} = 0$. Our final state can be written as $|n'l'l_{\mathrm{c}}L'ss_{\mathrm{c}}SJ'M_{J'}\rangle$; the spin part of the state is unaffected by the dipole operator.

The dipole operator acts on the electronic orbital angular momentum of the active electron. This means that the state vector written above must be decoupled, such that [40]

$$|nll_{\mathrm{c}}Lss_{\mathrm{c}}SJM_J\rangle = \sum_{M_L,M_S} C^{JM_J}_{LM_L,SM_S}|nll_{\mathrm{c}}LM_L\rangle|ss_{\mathrm{c}}SM_S\rangle, \tag{A.1.3}$$

where $C^{JM_J}_{LM_L,SM_S}$ is a Clebsch-Gordan coefficient. In (A.1.3) we have split up the orbital and spin parts. When taking the matrix element of the operator in (A.0.2), the spin part is unaffected; consequently, the spin part can be factored out. Using the normalization of the states, we have that $\langle ss_{\mathrm{c}}SM_S|ss_{\mathrm{c}}SM_S\rangle = 1$. Decoupling the states in (A.1.3) further, we find

$$|nll_{\mathrm{c}}Lss_{\mathrm{c}}SJM_J\rangle = \sum_{M_L,M_S} C^{JM_J}_{LM_L,SM_S}|nLM_L\rangle|ss_{\mathrm{c}}SM_S\rangle, \tag{A.1.4}$$

where we have used the fact that $C^{LM_L}_{lm_l,00} = \delta_{lL}\delta_{m_lM_L}$ and consequently omitted the electronic orbital angular momentum labels. Applying the expression in (A.1.4) and the equivalent expression for the final state vector, we find

$$\begin{aligned}\Omega_{1e} \equiv \langle n'l'l_{\mathrm{c}}L'ss_{\mathrm{c}}SJ'M_{J'}|\hat{r}|nll_{\mathrm{c}}Lss_{\mathrm{c}}SJM_J\rangle = \\ \sum_{M_LM_S}\sum_{M_{L'}M_{S'}} C^{JM_J}_{LM_L,SM_S}C^{J'M_{J'}}_{L'M_{L'},SM_S}\langle nLM_L|\hat{r}|n'L'M_{L'}\rangle.\end{aligned} \tag{A.1.5}$$

The matrix element $\langle nLM_L|\hat{r}|n'L'M_{L'}\rangle$ can be evaluated using the properties

of spherical harmonics to give [40]

$$\begin{aligned}\Omega_{1e} = &\sum_{p}\sum_{M_L M_S}\sum_{M_{L'} M_{S'}} (-1)^{L+L'+2S-M_J-M_{J'}}\sqrt{(2J+1)(2J'+1)} \\ &\times \begin{pmatrix} L & S & J \\ M_L & M_S & -M_J \end{pmatrix}\begin{pmatrix} L' & S & J' \\ M_{L'} & M_S & -M_{J'} \end{pmatrix}\sqrt{\frac{4\pi}{3}} \\ &\times \begin{pmatrix} L & 1 & L' \\ 0 & 0 & 0 \end{pmatrix}\begin{pmatrix} L & 1 & L' \\ M_L & p & -M_{L'} \end{pmatrix}\sqrt{\frac{3(2L+1)(2L'+1)}{4\pi}},\end{aligned} \tag{A.1.6}$$

where the symbols in round brackets denote Wigner $3j$ symbols. Using standard summation rules for Wigner $3j$ symbols, we obtain [40, 168]

$$\begin{aligned}\Omega_{1e} = &\sum_{p}(-1)^{S-M_J-L-J}\sqrt{(2J+1)(2L+1)}C^{L'0}_{L0,10}C^{J'M_{J'}}_{JM_J,1p} \\ &\times \begin{Bmatrix} J & 1 & J' \\ L' & S & L \end{Bmatrix}.\end{aligned} \tag{A.1.7}$$

Finally, we use explicit expressions for the first Clebsch-Gordan coefficient and sum over the squares of the second Clebsch-Gordan in (A.1.7) to obtain [40]

$$\Omega^2_{1e} = (2J'+1)l_{\max}\begin{Bmatrix} J & 1 & J' \\ L' & S & L \end{Bmatrix}, \tag{A.1.8}$$

as found in the literature (see for example [27]).

A.2 Single Atom Transitions for Doubly Excited States

For divalent atoms it is possible to have doubly excited states, as discussed in chapter 4. The doubly excited states can undergo dipole transitions as well, however the angular momentum is not only carried by the electron undergoing the transition. The sharing of the angular momentum between two electrons in strontium necessitates a more complicated expression than that in equation (A.1.8).

In the derivation of (A.1.8) we assumed that the inner core carried no momentum. In the case of strontium, however, we describe the state with

$|n_1 n_2 l_1 l_2 L s_1 s_2 S J M_J\rangle$, where we take the electron labelled 2 as being the active electron in the transition. Expanding this in a similar way to (A.1.3) using Wigner $3j$ symbols we have

$$\begin{aligned}|n_1 n_2 l_1 l_2 L S J M\rangle = &\sum_{M_L M_S}\sum_{m_{l_1} m_{l_2}} \\ &(-1)^{L+S-M_J+l_1+l_2-M_L}\sqrt{(2L+1)(2J+1)} \\ &\begin{pmatrix} L & S & J \\ M_L & M_S & -M_J \end{pmatrix}\begin{pmatrix} l_1 & l_2 & L \\ m_{l_1} & m_{l_2} & -M_L \end{pmatrix} \\ &\times |n_1 l_1 m_{l_1} n_2 l_2 m_{l_2}\rangle |S M_S\rangle.\end{aligned} \tag{A.2.9}$$

Taking the angular matrix element of the angular dipole operator for the second electron, we find

$$\begin{aligned}\Omega_{2e} &\equiv \sum_p \sqrt{\frac{4\pi}{3}}\langle n_1 n_2 l_1 l_2' L' S J' M_J' | Y_{1p} | n_1 n_2 l_1 l_2 L S J M_J\rangle \\ &= \sum_p \sqrt{\frac{4\pi}{3}} \sum_{M_L m_{l_1} m_{l_2}} \sum_{M_{L'}' m_{l_2}'} \sum_{M_S} (-1)^{m_{l_1}-M_J-M_J'-M_L-M_L'-m_{l_2}-l_1-1} \\ &\times \begin{pmatrix} l_1 & l_2 & L \\ m_{l_1} & m_{l_2} & -M_L \end{pmatrix}\begin{pmatrix} L & S & J \\ M_L & M_S & -M_J \end{pmatrix} \\ &\times \begin{pmatrix} l_1' & l_2' & L' \\ m_{l_1}' & m_{l_2}' & -M_{L'}' \end{pmatrix}\begin{pmatrix} L' & S' & J' \\ M_{L'}' & M_{S'}' & -M_{J'}' \end{pmatrix} \\ &\times \sqrt{(2L+1)(2J+1)(2L'+1)(2J'+1)}\langle n_2' l_2' m_{l_2}' | Y_{1p} | n_2 l_2 m_{l_2}\rangle.\end{aligned} \tag{A.2.10}$$

By evaluating the matrix element $\langle n_2' l_2' m_{l_2}' | Y_{1p} | n_2 l_2 m_{l_2}\rangle$ in a similar way than in (A.1.6) and applying sum rules for the Wigner $3j$ symbols we obtain

$$\begin{aligned}\Omega_{2e} &= \sum_p \sqrt{\frac{4\pi}{3}}\langle n_1 n_2 l_1 l_2' L' S J' M_J' | Y_{1p} | n_1 n_2 l_1 l_2 L S J M_J\rangle \\ &= (-1)^{l_1+S+M_J'}\sqrt{\frac{3}{4\pi}(2l_2+1)(2l_2'+1)}\begin{pmatrix} l_2 & 1 & l_2' \\ 0 & 0 & 0 \end{pmatrix} \\ &\times \sqrt{(2L+1)(2L'+1)(2J+1)(2J'+1)} \\ &\times \begin{pmatrix} J' & 1 & J \\ -M_{J'} & p & -M_J \end{pmatrix}\begin{Bmatrix} J' & 1 & J \\ L & S & L' \end{Bmatrix}\begin{Bmatrix} L' & 1 & L \\ l_2 & l_1 & l_2' \end{Bmatrix}.\end{aligned} \tag{A.2.11}$$

Finally, we apply the same expressions for Clebsch-Gordan coefficients as in (A.1.8) (after converting the Wigner $3j$ symbols) and take the root of the sum of squares of the second Wigner $3j$ symbol in (A.2.11) to find the final expression

$$\Omega_{2e} = (-1)^{l_1+l_{2,\max}+S}\sqrt{l_{2,\max}(2L'+1)(2J'+1)(2L+1)} \times \begin{Bmatrix} J' & 1 & J \\ L & S & L' \end{Bmatrix} \begin{Bmatrix} L' & 1 & L \\ l_2 & l_1 & l_2' \end{Bmatrix}. \tag{A.2.12}$$

A.3 Two Atom Transitions for Singly Excited States

In the calculation of dipole-dipole and quadrupole-quadrupole interactions, it is useful to separate the calculation into the radial parts and the angular parts in a similar way to the case of single atom transitions. The full interaction Hamiltonian for multipolar interactions is given by equation (3.11), which contains radial and angular parts. In equation (3.14), the angular parts are separated from the interatomic distance and the radial parts, leaving us with the angular coefficient

$$H_{\text{int}}^{(\text{angular})} = \sum_{k_1,k_2=1}^{\infty} (-1)^{k_2}\sqrt{\frac{(4\pi)^3(2k_1+2k_2)!}{(2k_1+1)!(2k_2+1)!(2k_1+2k_2+1)}} \times \sum_{p=-(k_1+k_2)}^{k_1+k_2} \sum_{p_1=-k_1}^{k_1} \sum_{p_2=-k_2}^{k_2} C_{k_1p_1,k_2p_2}^{k_1+k_2,p} Y_{k_1,p_1}(\hat{r}_1) Y_{k_2,p_2}(\hat{r}_2) Y_{k_1+k_2,p}(\hat{R}). \tag{A.3.13}$$

We follow the same procedure as for the dipole transitions, and decompose the basis to obtain (assuming the inner core does not carry angular momentum) equation (A.1.4). We note that once again (A.3.13) does not act on the spin parts of the wavefunction.

When we do not sum over the values of p (as was the case in the single atom

transition) we have the matrix elements of the spherical harmonics given by

$$\begin{aligned}\langle L'S'J'M'_J|Y_{k,p}|LSJM_J\rangle \\ &= (-1)^{l_o+l'_o+1}\sqrt{\frac{(2l_o+1)(2J+1)(2k+1)}{4\pi}} \\ &\quad\times C^{l'_o 0}_{l_o 0 k 0} C^{J'M'_J}_{JM_J kp} \begin{Bmatrix} J & k & J' \\ l'_o & S & l_o \end{Bmatrix}. \end{aligned} \tag{A.3.14}$$

Combining this matrix element with the full expression for the angular part of the multipolar interaction in (A.3.13), we find the coefficients for the angular part of the interaction to be

$$\begin{aligned} D_{k_1k_2}(\alpha' M'_1 M'_2, \alpha M_1 M_2; \hat{R}) &= (-1)^{k_2} \\ &\times \sqrt{\frac{4\pi(2k_1+2k_2)!(2L_1+1)(2L_2+1)}{(2k_1)!(2k_2)!(2k_1+2k_2+1)}} \\ &\times \sqrt{(2J_1+1)(2J_2+1)}\, C^{L'_1 0}_{L_1 0, k_1 0} C^{L'_2 0}_{L_2 0, k_2 0} \\ &\times \begin{Bmatrix} J_1 & k_1 & J'_1 \\ L'_1 & S & L_1 \end{Bmatrix} \begin{Bmatrix} J_2 & k_2 & J'_2 \\ L'_2 & S & L_2 \end{Bmatrix} \\ &\times \sum_{p=-(k_1+k_2)}^{k_1+k_2} \sum_{p_1=-k_1}^{k_1} \sum_{p_2=-k_2}^{k_2} Y_{k_1+k_2,p}(\hat{R}) \\ &\times C^{k_1+k_2,p}_{k_1 p_1, k_2 p_2} C^{J'_1 M'_1}_{J_1 M_1, k_1 p_1} C^{J'_2 M'_2}_{J_2 M_2, k_2 p_2}. \end{aligned} \tag{A.3.15}$$

Recall that α and α' denote the full set of quantum numbers needed to describe the original and final states respectively, and $\hat{R}$ is the angular part of atom 2 relative to atom 1.

Appendix B

MQDT Models

In this appendix we present the tables of the MQDT models which were used to calculate the data in chapter 4. The tables include the **K** reactance matrix, as well as the ionization limits used in the model and the energy dependences.

Channel	$5sns\ {}^1S_0$	$4d_{3/2}nd_{3/2}$	$4d_{5/2}nd_{5/2}$
i	1	2	3
Ionization Limit (cm^{-1})	45932.1982	60488.09	60768.48
K_{i1}	1.054(2)	-0.023(1)	0.370(3)
K_{i2}	-0.023(1)	2.9(3)	0.0
K_{i3}	0.370(3)	0.0	-0.66(1)
$K_{ii}^{(1)}$	0.83(3)	-13(10)	0.51(7)

Table B.1: The three-channel MQDT parameters for the $^1S_0$ series of strontium. The energy dependence of the diagonals of the $K_{i\alpha}$ matrix are defined in (4.15). Estimates of the uncertainties in the last digit are shown in brackets.

Channel	5sns ^{3}S$_1$	5pnp
i	1	2
Ionization Limit (cm^{-1})	45932.1982	70048.11
K_{i1}	-34.2(4)	-155(4)
K_{i2}	-155(4)	-1470(40)
$K_{ii}^{(1)}$	-19.14(2)	-1408(4)

Table B.2: The two-channel MQDT parameters for the ^{3}S$_1$ series of strontium. The energy dependence of the diagonals of the $K_{i\alpha}$ matrix are defined in (4.15). Estimates of the uncertainties in the last digit are shown in brackets.

Channel	5snp ^{1}P$_1$	4dnp
i	1	2
Ionization Limit (cm^{-1})	45932.1982	60628.26
K_{i1}	10.842(4)	16.18(2)
K_{i2}	16.18(2)	22.56(3)
$K_{ii}^{(1)}$	-0.39(1)	1.68(2)

Table B.3: The two-channel MQDT parameters for the ^{1}P$_1$ series of strontium. The energy dependence of the diagonals of the $K_{i\alpha}$ matrix are defined in (4.15). Estimates of the uncertainties in the last digit are shown in brackets.

Channel	5snp ^{3}P$_0$	4dnp ^{3}P$_0$	4dnf
i	1	2	3
Ionization Limit (cm^{-1})	45932.1982	60628.26	60628.26
K_{i1}	-1.028(2)	-0.1831(3)	-0.1040(5)
K_{i2}	-0.1831(3)	-0.617(2)	0
K_{i3}	-0.1040(5)	0	-0.6089(2)
$\frac{dK_{ii}}{dE}$	-0.9854(5)	0.282(4)	0.1185(9)
Channel	5snp ^{3}P$_1$	4dnp ^{3}P$_1$	4dnf
K_{i1}	-1.063(2)	-0.1887(1)	-0.107(1)
K_{i2}	-0.1887(1)	-0.57(1)	0
K_{i3}	-0.107(1)	0	-0.6047(3)
$\frac{dK_{ii}}{dE}$	-1.013(2)	0.09(6)	0.083(2)
Channel	5snp ^{3}P$_2$	4dnp ^{3}P$_2$	4dnf
K_{i1}	-1.1067(9)	-0.1716(1)	-0.1273(4)
K_{i2}	-0.1716(1)	-0.6052(7)	0
K_{i3}	-0.1273(4)	0	-0.6115(5)
$\frac{dK_{ii}}{dE}$	-1.0243(9)	0.089(4)	0.086(1)

Table B.4: The three-channel MQDT parameters for the ^{3}P$_0$ (top), ^{3}P$_1$ (middle) and ^{3}P$_2$ (bottom) series of strontium. The energy dependence of the diagonals of the $K_{i\alpha}$ matrix are defined in (4.15). Estimates of the uncertainties in the last digit are shown in brackets. The 5s13p states of all the triplet series are outliers and have been neglected, as discussed in section 4.7.

Channel	$5snd_{5/2}$	$5snd_{3/2}$	$4d_{5/2}ns$	$4d_{3/2}ns$	$5pnp$	$4dnd$
i	1	2	3	4	5	6
Ionization Limit (cm^{-1})	45932.1982	45932.1982	60768.48	60488.09	70048.11	60628.26
K_{i1}	-0.6507(9)	-0.114(6)	-0.759(2)	$-2.7(1) \times 10^{-4}$	-0.56(1)	$-4(7) \times 10^{-4}$
K_{i2}	-0.114(6)	-0.489(3)	0.362(7)	-0.644(1)	0.11(1)	0.0909(5)
K_{i3}	-0.759(2)	0.362(7)	1.060(2)	0.222(1)	0	0
K_{i4}	$-2.7(1) \times 10^{-4}$	-0.644(1)	0.222(1)	1.172(2)	0	0
K_{i5}	-0.56(1)	0.11(1)	0	0	1.51(5)	0
K_{i6}	$-4(7) \times 10^{-4}$	0.0909(5)	0	0	0	2.3660(1)
$K_{ii}^{(1)}$	3.2(1)	0.06(3)			0.06(9)	

Table B.5: The six-channel MQDT parameters for the $^{1,3}D_2$ series of strontium. The energy dependence of the channel quantum defects are defined in (4.15). Estimates of the uncertainties in the last digit are shown in brackets.

Channel	5snd ^{3}D$_1$	4dns	4dnd
i	1	2	3
Ionization Limit (cm^{-1})	45932.1982	60628.26	60628.26
K_{i1}	-1.55(1)	0.549(2)	-0.0004(8)
K_{i2}	0.549(2)	1.451(1)	0
K_{i3}	-0.0004(8)	0	2.2(8)
$K_{ii}^{(1)}$	-1.25(2)	1.2(1)	-30(50)
Channel	5snd ^{3}D$_3$	4dns ^{3}D$_3$	5pnp
K_{i1}	-1.487(8)	0.43(2)	0.23(2)
K_{i2}	0.4(2)	1.21(1)	0
K_{i3}	0.2(2)	0	-0.5(2)
$K_{ii}^{(1)}$	-1.10(1)	10(2)	7(2)

Table B.6: The three-channel MQDT parameters for the ^{3}D$_1$ (top) and ^{3}D$_3$ (bottom) series of the D states of strontium. The energy dependence of the diagonals of the $K_{i\alpha}$ matrix are defined in (4.15). Estimates of the uncertainties in the last digit are shown in brackets. The 5s13d ^{3}D$_1$ and 5s22d ^{3}D$_3$ are outliers and have been excluded, as discussed in section 4.3.6.

Channel	5snf ^{1}F$_3$	4dnp
i	1	2
Ionization Limit (cm^{-1})	45932.1982	60628.26
K_{i1}	0.383(4)	0.4522(6)
K_{i2}	0.4522(6)	-0.683(5)
$K_{ii}^{(1)}$	0.333(6)	-1.41(4)

Table B.7: The two-channel MQDT parameters for the ^{1}F$_3$ series of strontium. The energy dependence of the channel quantum defects are defined in (4.15). Estimates of the uncertainties in the last digit are shown in brackets.

Channel	5snf ^{3}F$_2$	4dnp ^{3}F$_2$	4dnf
i	1	2	3
Ionization Limit (cm^{-1})	45932.1982	60628.26	60628.26
K_{i1}	0.6489(2)	-0.056(2)	-0.006(1)
K_{i2}	-0.056(2)	1.15(6)	0
K_{i3}	-0.006(2)	0	2.44(2)
$K_{ii}^{(1)}$	0.4444(2)	3.77(6)	-22.6(4)
Channel	5snf ^{3}F$_3$	4dnp ^{3}F$_3$	4dnf
K_{i1}	0.6505(9)	-0.0512(9)	-0.007(6)
K_{i2}	-0.0512(9)	1.1(2)	0
K_{i3}	-0.007(6)	0	3.0(2)
$K_{ii}^{(1)}$	0.449(1)	10(2)	-33(5)
Channel	5snf ^{3}F$_4$	4dnp ^{3}F$_4$	4dnf
K_{i1}	0.662(8)	-0.03(2)	-0.011(3)
K_{i2}	-0.03(2)	1.11(5)	0
K_{i3}	-0.011(3)	0	2.68(8)
$K_{ii}^{(1)}$	0.47(1)	30(10)	-24.4(5)

Table B.8: The three-channel MQDT parameters for the ^{3}F$_2$ (top), ^{3}F$_3$ (middle) and ^{3}F$_4$ (bottom) series of strontium. The energy dependence of the diagonals of the K_{ii} matrix are defined in (4.15). Estimates of the uncertainties in the last digit are shown in brackets.

Appendix C

C_3 Coefficients for Spin Transfer Calculations

To calculate the various dynamics arising from the $2 \times n\,^3\mathrm{D}_2 \rightarrow (n-2)\,^1\mathrm{F}_3 + (n-3)\,^3\mathrm{F}_3$ Förster resonance in a spin chain (as shown in chapter 5), the couplings between the different states are required. We present the C_3 coefficients for the resonant couplings between the states of interest in table C.1; note that we have taken $M_J = 2$ for all states, as discussed in chapter 5.

Initial Pair State	Final Pair State	C_3 coefficient (a.u.)
$30\ ^3\mathrm{D}_2 + 28\ ^1\mathrm{F}_3$	$28\ ^1\mathrm{F}_3 + 30\ ^3\mathrm{D}_2$	-3716.9
$30\ ^3\mathrm{D}_2 + 27\ ^3\mathrm{F}_3$	$27\ ^3\mathrm{F}_3 + 30\ ^3\mathrm{D}_2$	-124122
$30\ ^3\mathrm{D}_2 + 30\ ^3\mathrm{D}_2$	$28\ ^1\mathrm{F}_3 + 28\ ^1\mathrm{F}_3$	4397.9
$30\ ^3\mathrm{D}_2 + 30\ ^3\mathrm{D}_2$	$27\ ^3\mathrm{F}_3 + 27\ ^3\mathrm{F}_3$	146863
$30\ ^3\mathrm{D}_2 + 30\ ^3\mathrm{D}_2$	$27\ ^3\mathrm{F}_3 + 28\ ^1\mathrm{F}_3$	25414.3*
$30\ ^3\mathrm{D}_2 + 28\ ^1\mathrm{F}_3$	$27\ ^3\mathrm{F}_3 + 30\ ^3\mathrm{D}_2$	-21479
$30\ ^3\mathrm{D}_2 + 28\ ^3\mathrm{F}_3$	$27\ ^3\mathrm{F}_3 + 30\ ^3\mathrm{D}_2$	142154
$30\ ^3\mathrm{D}_2 + 28\ ^3\mathrm{F}_3$	$28\ ^1\mathrm{F}_3 + 30\ ^3\mathrm{D}_2$	24599.5
$30\ ^3\mathrm{D}_2 + 30\ ^3\mathrm{D}_2$	$28\ ^3\mathrm{F}_3 + 28\ ^3\mathrm{F}_3$	192636
$30\ ^3\mathrm{D}_2 + 30\ ^3\mathrm{D}_2$	$27\ ^3\mathrm{F}_3 + 28\ ^3\mathrm{F}_3$	-168200*
$30\ ^3\mathrm{D}_2 + 28\ ^3\mathrm{F}_3$	$28\ ^3\mathrm{F}_3 + 30\ ^3\mathrm{D}_2$	-162807
$30\ ^3\mathrm{D}_2 + 30\ ^3\mathrm{D}_2$	$28\ ^1\mathrm{F}_3 + 28\ ^3\mathrm{F}_3$	-29106.5*

Table C.1: C_3 coefficients used in the calculations presented in chapter 5 when determining the dynamics of spin transfer in chains of strontium Rydberg atoms. All coefficients remain the same under interchange of the initial and final states, and those states marked with asterisks are also symmetric when the ordering of the final pair state is swapped.

Bibliography

[1] I Martinson and L J Curtis. Janne Rydberg— his life and work. *Nuclear Instruments and Methods in Physics Research Section B*, 235:17, 2005. 1

[2] T F Gallagher. *Rydberg Atoms*. Cambridge University Press, 1994. 1, 2, 9, 12, 27, 32, 34, 67

[3] M Saffman, T G Walker, and K Mølmer. Quantum information with Rydberg atoms. *Reviews of Modern Physics*, 82:2313, 2010. 1, 2, 35, 137, 140

[4] I Lesanovsky. Many-Body Spin Interactions and the Ground State of a Dense Rydberg Lattice Gas. *Physical Review Letters*, 106:025301, 2011. 1, 2

[5] H Weimer, M Müller, I Lesanovsky, P Zoller, and H P Büchler. A Rydberg quantum simulator. *Nature Physics*, 6:382, 2010. 1

[6] J J Mestayer, B Wyker, J C Lancaster, F B Dunning, C O Reinhold, S Yoshida, and J Burgdörfer. Realization of Localized Bohr-Like Wave Packets. *Physical Review Letters*, 100:243004, 2008. 2

[7] C Monroe. Quantum information processing with atoms and photons. *Nature*, 416:238, 2002. 2

[8] T G Walker and M Saffman. Consequences of Zeeman degeneracy for the van der Waals blockade between Rydberg atoms. *Physical Review A*, 77: 032723, 2008. 2, 36, 48, 52, 53, 54, 66

[9] M D Lukin, M Fleischhauer, R Cote, L M Duan, D Jaksch, J I Cirac, and P Zoller. Dipole Blockade and Quantum Information Processing in Mesoscopic Atomic Ensembles. *Physical Review Letters*, 87:037901, 2001. 2, 35, 137

[10] D Paredes-Barato and C S Adams. All-Optical Quantum Information Processing Using Rydberg Gates. *Physical Review Letters*, 112:040501, 2014. 2, 137

[11] J D Pritchard, D Maxwell, A Gauguet, K J Weatherill, M P A Jones, and C S Adams. Cooperative Atom-Light Interaction in a Blockaded Rydberg Ensemble. *Physical Review Letters*, 105:193603, 2010. 2, 33, 35

[12] R Mukherjee, J Millen, M P A Jones, and T Pohl. Manby-body physics with alkaline-earth Rydberg lattices. *Journal of Physics B*, 44:184010, 2011. 2, 57, 66, 109, 138

[13] R Heidemann, U Raitzsch, V Bendkowsky, B Butscher, R Löw, L Santos, and T Pfau. Evidence for Coherent Rydberg Excitation in the Strong Blockade Regime. *Physical Review Letters*, 99:163601, 2007. 3

[14] G Pupillo, A Micheli, M Boninsegni, I Lesanovsky, and P Zoller. Strongly Correlated Gases of Rydberg-Dressed Atoms: Quantum and Classical Dynamics. *Physical Review Letters*, 104:223002, 2010. 3, 4

[15] N Henkel, R Nath, and T Pohl. Three-Dimensional Roton Excitations and Supersolid Formation in Rydberg-Excited Bose-Einstein Condensates. *Physical Review Letters*, 104:195302, 2010. 3, 33

[16] E Kim and M H W Chan. Probable observation of a supersolid helium phase. *Nature*, 427:225, 2004. 3

[17] D Y Kim and M H W Chan. Absence of Supersolidity in Solid Helium in Porous Vycor Glass. *Physical Review Letters*, 109:155301, 2012. 3

[18] W D Phillips. Laser cooling and trapping of neutral atoms. *Reviews of Modern Physics*, 70:721, 1998. 3, 9

[19] M Aymar. Rydberg Series of Alkaline-Earth Atoms Ca through Ba. *Physics Reports*, 110:163, 1984. 4, 5, 68, 72, 79, 92

[20] J Millen. *A cold strontium Rydberg gas*. PhD thesis, University of Durham, 2011. 4, 102

[21] J Millen, G Lochead, and M P A Jones. Two-Electron Excitation of an Interacting Cold Rydberg Gas. *Physical Review Letters*, 105:213004, 2010. 4

[22] J Millen, G Locheead, G R Corbett, R M Potvliege, and M P A Jones. Spectroscopy of a cold strontium Rydberg gas. *Journal of Physics B*, 44: 184001, 2011. 4, 5, 22, 49, 50, 67, 108, 137

[23] B H Bransden and C J Joachain. *Physics of Atoms and Molecules*. Pearson Education, 2nd edition edition, 2003. 4, 12, 13, 14, 15, 16, 26, 27, 30, 34, 42, 55, 92, 93, 131, 132

[24] A V Gorshkov, M Hermele, V Gurarie, C Xu, P S Julienne, J Ye, P Zoller, E Demler, M D Lukin, and A M Rey. Two-orbital $SU(N)$ magnetism with ultracold alkaline-earth atoms. *Nature Physics*, 6:289, 2010. 4, 33, 109

[25] A D Ludlow, T Zelevinsky, G K Campbell, S Blatt, M M Boyd, M H G de Miranda, M J Martin, J W Thomsen, S M Foreman, J Ye, T M Fortier, J E Stalnaker, S A Diddams, Y Le Coq, Z W Barber, N Poli, N D Lemke, K M Beck, and C W Oates. Sr Lattice Clock at 1×10^{16} Fractional Uncertainty by Remote Optical Evaluation with a Ca Clock. *Science*, 319:1805, 2008. 4, 109

[26] L I R Gil, R Mukherjee, E M Bridge, M P A Jones, and T Pohl. Spin squeezing in a Rydberg lattice clock. *Physical Review Letters*, 112:103601, 2014. 4, 56, 68, 109, 140

[27] C E Theodosiou. Lifetimes of alkali-metal - atom Rydberg states. *Physical Review A*, 30:2881, 1984. 4, 30, 32, 34, 143

[28] A R Edmonds, R Pullen, J Picart, and N Tran Minh. Tables for the computation of radial integrals in the Coulomb approximation. *Journal of Physics B*, 12:2781, 1979. 19, 20, 34, 137

[29] M Aymar, O Robaux, and S Wane. Central-field calculations of photoionisation cross sections of excited states of Rb and Sr^+ and analysis of photoionisation cross sections of excited alkali atoms using quantum defect theory. *Journal of Physics B*, 17:993, 1984. 4

[30] M Aymar, C H Greene, and E Luc-Koenig. Multichannel Rydberg spectroscopy of complex atoms. *Reviews of Modern Physics*, 68:1015, 1996. 5, 6, 67, 68, 70, 73

[31] H G C Werij, C H Greene, C E Theodosiou, and Gallagher A. Oscillator strengths and radiative branching ratios in atomic Sr. *Physical Review A*, 46:1248, 1992. 5, 100, 102, 104

[32] T. Giamarchi. *Quantum Physics in One Dimension*. Oxford University Press, 2003. 6, 109, 118, 133

[33] P J Mohr, B N Taylor, and D B Newell. CODATA recommended values of the fundamental physical constants: 2010. *Reviews of Modern Physics*, 84: 1527, 2012. 8

[34] M J Seaton. Quantum Defect Theory. *Reports on Progress in Physics*, 46: 167, 1983. 11, 70, 71, 73, 137

[35] C Cohen-Tannoudji, J Dupont-Roc, and G Grynberg. *Atom-Photon Interactions*. John Wiley and Sons, 1992. 15, 32

[36] J Ahn, T C Weinacht, and P H Bucksbaum. Information Storage and Retrieval Through Quantum Phase. *Science*, 287:463, 2000. 15

[37] R P Abel, C Carr, U Krohn, and C S Adams. Electrometry near a dielectric surface using Rydberg electromagnetically induced transparency. *Physical Review A*, 84:023408, 2011. 15

[38] C J Joachain, N J Kylstra, and R M Potvliege. *Atoms in Intense Laser Fields*. Cambridge University Press, 2011. 16

[39] M Marinescu, H R Sadeghpour, and A Dalgarno. Dispersion coefficients for alkali-metal dimers. *Physical Review A*, 49:982, 1994. 17, 36

[40] D M Brink and G R Satchler. *Angular Momentum*. Clarendon Press, 3rd edition edition, 1993. 18, 30, 37, 62, 78, 142, 143

[41] V A Davydkin and B A Zon. Radiation and polarization characteristics of Rydberg atomic states. *Optics and Spectroscopy*, 51:25, 1981. 18, 19, 20, 34, 137

[42] R E Langer. On the Connection Formulas and the Solutions of the Wave Equation. *Physical Review*, 51:669, 1937. 19, 23

[43] B Oumarou, J Picart, N Tran Minh, and J Chapelle. New and rapid method for calculation of electric dipole and quadrupole radial integrals between atomic Rydberg states. *Physical Review A*, 37:1885, 1988. 19, 20, 21, 34, 137

[44] J Picart, A R Edmonds, and N Tran Minh. Extrapolation to high principal quantum numbers of radial integrals in the Coulomb approximation. *Journal of Physics B*, 11:L651, 1978. 19, 20, 34, 137

[45] M J Seaton. Coulomb functions for attractive and repulsive potentials and for positive and negative energies. *Computer Physics Communications*, 146: 225, 2002. 23, 27, 34, 70, 76, 137

[46] M J Seaton. FGH, a code for the calculation of Coulomb radial wave functions from series expansions. *Computer Physics Communications*, 146:250, 2002. 24

[47] M J Seaton. NUMER, a code for Numerov integrations of Coulomb functions. *Computer Physics Communications*, 146:254, 2002. 23, 24, 34

[48] M J Seaton. Coulomb functions analytic in the energy. *Computer Physics Communications*, 25:87, 1982. 23, 25

[49] F S Ham. The Quantum Defect Method. *Solid State Physics*, 1:217, 1955. 25, 137

[50] E Clementi and C Roetti. Roothan-Hartree-Fock Atomic Wavefunctions: Basis Functions and their Coefficients for Ground and Certain Excited States of Neutral and Ionized Atoms, $Z \leq 54$. *Atomic Data and Nuclear Data Tables*, 14:177, 1974. 26

[51] M S Safronova and U I Safronova. Critically evaluated theoretical energies, lifetimes, hyperfine constants and multipole polarizabilities in ^{87}Rb. *Physical Review A*, 83:052508, 2011. 26, 30

[52] J E Sansonetti. Wavelengths, Transition Probabilities, and Energy Levels for the Spectra of Rubidium (Rb I through Rb XXXVII). *Journal of Physical and Chemical Reference Data*, 35:301, 2006. 27

[53] W Demtröder. *Laser Spectroscopy*. Springer, 2003. 27

[54] T F Gallagher, R M Hill, and S A Edelstein. Resonance measurements of d-f splittings in highly excited states of sodium. *Physical Review A*, 13:1448, 1976. 27

[55] I G Hughes and T P A Hase. *Measurements and Their Uncertainties*. Oxford University Press, 2010. 28, 34, 51, 75

[56] J E Sansonetti. Wavelengths, Transition Probabilities, and Energy Levels for the Spectra of Cesium (Cs I - Cs LV). *Journal of Physical and Chemical Reference Data*, 38:761, 2009. 28

[57] W Li, I Mourachko, M W Noel, and T F Gallagher. Millimeter-wave spectroscopy of cold Rb Rydberg atoms in a magneto-optical trap: Quantum defects of the ns, np, and nd series. *Physical Review A*, 67:052502, 2003. 29

[58] J Han, Y Jamil, D V L Norum, P J Tanner, and T F Gallagher. Rb nf quantum defects from millimeter-wave spectroscopy of cold ^{8}5Rb Rydberg atoms. *Physical Review A*, 74:054502, 2006. 29

[59] C J Lorenzen and K Niemax. Precise Quantum Defects of nS, nP and nD Levels in Cs I. *Zeitschrift für Physik A*, 315:127, 1984. 29

[60] K H Weber and C J Sansonetti. Accurate energies of nS, nP, nD, nF, and nG levels of neutral cesium. *Physical Review A*, 35:4650, 1987. 29

[61] P Esherick. Bound, even-parity $J = 0$ and $J = 2$ spectra of Sr. *Physical Review A*, 15:1920, 1977. 28, 31, 37, 69, 72, 79, 80, 85, 89, 90, 92, 93, 115, 139

[62] R Beigang, K Lücke, A Timmermann, P J West, and D Frölich. Determination of absolute level energies of $5sns\,{}^{1}\mathrm{S}_0$ and $5snd\,{}^{1}\mathrm{D}_2$ Rydberg series of Sr. *Optics Communications*, 42:19, 1982. 29, 31, 80, 81, 90

[63] J R Rubbmark and S A Borgström. Rydberg Series in Strontium Found in Absorption by Selectively Laser-Excited Atoms. *Physica Scripta*, 18:196, 1978. 31, 86, 96, 98, 99

[64] R Beigang, K Lücke, D Schmidt, A Timmermann, and P J West. One-Photon Laser Spectroscopy of Rydberg Series from Metastable Levels in Calcium and Strontium. *Physica Scripta*, 26:183, 1982. 31, 84, 94, 95

[65] J A Armstrong, J J Wynne, and P Esherick. Bound, odd-parity $J = 1$ spectra of the alkaline earths: Ca, Sr, and Ba. *Journal of the Optical Society of America*, 69:211, 1979. 28, 29, 31, 86, 87

[66] P Esherick, J J Wynne, and J A Armstrong. Spectroscopy of $^{3}\mathrm{P}_0$ states of alkaline earths. *Optics Letters*, 1:19, 1977.

[67] R Beigang and D Schmidt. Two-Channel MQDT Analysis of Bound $5snd\,{}^{3}D_{1,3}$ Rydberg States of Strontium. *Physica Scripta*, 27:172, 1983.

[68] C E Moore. *Atomic Energy Levels (Chromium Through Niobium)*, volume 2. Washington, DC: US Government Printing Office, 1952.

[69] W R S Garton and K Codling. Ultra-violet extensions of the arc spectra of the alkaline earths: The absorption spectrum of strontium vapour. *Journal of Physics B*, 1:106, 1968.

[70] C J Dai. Perturbed $5snd\,^{1,3}D_2$ Rydberg series of Sr. *Physical Review A*, 52: 4416, 1995. 28, 89, 100

[71] T R Gentile, B J Hughey, and D Kleppner. Microwave spectroscopy of calcium Rydberg states. *Physical Review A*, 42:440, 1990. 29, 31

[72] M Miyabe, C Geppert, M Kato, M Oba, I Wakaida, K Watanabe, and K D A Wendt. Determination of Ionization Potential of Calcium by High-Resolution Resonance Ionization Spectroscopy. *Journal of the Physical Society of Japan*, 75:034302, 2006. 29, 31

[73] H Maeda, Y Matsuo, and M Takami. Optical-microwave double-resonance spectroscopy of highly excited Rydberg states of ytterbium. *Physical Review A*, 45:1732, 1992. 29, 31

[74] M Aymar, R J Champeau, C Delsart, and O Robaux. Three-step laser spectroscopy and multichannel quantum defect analysis of odd-parity Rydberg states of neutral ytterbium. *Journal of Physics B*, 17:3645, 1984. 29, 31, 37

[75] T F Gallagher and W E Cooke. Interactions of Blackbody Radiation with Atoms. *Physical Review Letters*, 42:835, 1979. 32

[76] I I Beterov, I I Ryabtsev, D B Tretyakov, and V M Entin. Quasiclassical calculations of blackbody-radiation-induced depopulation rates and effective lifetimes of Rydberg nS, nP, and nD alkali-metal atoms with $n \leq 80$. *Physical Review A*, 79:052504, 2009. 32

[77] J W Farley and W H Wing. Accurate calculation of dynamic Stark shifts and depopulation rates of Rydberg energy levels induced by blackbody radiation. Hydrogen, helium, and alkali-metal atoms. *Physical Review A*, 23:2397, 1981. 32, 34

[78] D B Branden, T Juhasz, T Mahlokozera, C Vesa, R O Wilson, M Zheng, A Kortyna, and D A Tate. Radiative lifetime measurements of rubidium Rydberg states. *Journal of Physics B*, 43:015002, 2010. 32, 33, 34, 138

[79] A L de Oliveira, M W Mancini, V S Bagnato, and L G Marcassa. Measurement of Rydberg-state lifetimes using cold trapped atoms. *Physical Review A*, 65:031401(R), 2002. 32, 33, 34

[80] T Wilk, A Gaëtan, C Evellin, J Wolters, Y Miroshnychenko, P Grangier, and A Browaeys. Entanglement of Two Individual Neutral Atoms Using Rydberg Blockade. *Physical Review Letters*, 104:010502, 2010. 35, 137

[81] L Isenhower, E Urban, X L Zhang, A T Gill, T Henage, T A Johnson, T G Walker, and M Saffman. Demonstration of a Neutral Atomc Controlled-NOT Quantum Gate. *Physical Review Letters*, 104:010503, 2010. 35

[82] F Cinti, P Jain, M Boninsegni, A Micheli, P Zoller, and G Pupillo. Supersolid Droplet Crystal in a Dipole-Blockaded Gas. *Physical Review Letters*, 105: 135301, 2010. 35, 137

[83] T Pohl, E Demler, and M D Lukin. Dynamical Crystallization in the Dipole Blockade of Ultracold Atoms. *Physical Review Letters*, 104:043002, 2010. 137

[84] J Schachenmayer, I Lesanovsky, A Micheli, and A J Daley. Dynamical crystal creation with polar molecules or Rydberg atoms in optical lattices. *New Journal of Physics*, 12:103044, 2010.

[85] C Carr, R Ritter, C G Wade, K J Weatherill, and C S Adams. Nonequilibrium Phase Transition in a Dilute Rydberg Ensemble. *Physical Review Letters*, 111:113901, 2013. 35

[86] V Bendkowsky, B Butscher, J Nipper, J P Shaffer, R Löw, and T Pfau. Observation of ultralong-range Rydberg molecules. *Nature*, 458:1005, 2009. 35

[87] K R Overstreet, A Schwettmann, J Tallant, D Booth, and J P Shaffer. Observation of electric-field-induced Cs Rydberg atom macrodimers. *Nature Physics*, 5:581, 2009. 35

[88] M P Robinson, B Laburthe Tolra, M W Noel, T F Gallagher, and P Pillet. Spontaneous Evolution of Rydberg Atoms into an Ultracold Plasma. *Physical Review Letters*, 85:4466, 2000. 35

[89] R J Buehler and J O Hirschfelder. Bipolar Expansion of Coulombic Potentials. *Physical Review*, 83:628, 1951. 36, 38, 40, 41

[90] A Dalgarno and W D Davison. The Calculation of Van Der Waals Interactions. *Advances in Atomic and Molecular Physics*, 2:1, 1966. 36, 43, 110

[91] K Singer, J Stanojevic, M Weidemüller, and R Côté. Long-range interactions between alkali Rydberg atom pairs correlated to the ns-ns, np-np and nd-nd asymptotes. *Journal of Physics B*, 38:S295, 2005. 36, 43, 45, 47, 48, 52, 55, 56, 66

[92] N Samboy, J Stanojevic, and Côté. Formation and properties of Rydberg macrodimers. *Physical Review A*, 83:050501(R), 2011. 36, 45

[93] A Reinhard, T Cubel Liebisch, B Knuffman, and G Raithel. Level shifts of rubidium Rydberg states due to binary interactions. *Physical Review A*, 75: 032712, 2007. 36, 52, 56, 66

[94] A Schwettman, J Crawford, K R Overstreet, and J P Shaffer. Cold Cs Rydberg-gas interactions. *Physical Review A*, 74:020701(R), 2006. 36

[95] J Stanojevic, R Côté, D Tong, S M Farooqi, E E Eyler, and P L Gould. Long-range Rydberg-Rydberg interactions and molecular resonances. *The European Physical Journal D*, 50:3, 2006. 36, 45

[96] C L Vaillant, M P A Jones, and R M Potvliege. Long-range Rydberg-Rydberg interactions in calcium, strontium and ytterbium. *Journal of Physics B*, 45:135004, 2012. 36, 52, 66, 78, 81, 115

[97] J A Armstrong, P Esherick, and J J Wynne. Bound even-parity $J = 0$ and 2 spectra of Ca: A multichannel quantum-defect theory analysis. *Physical Review A*, 15:180, 1977. 37, 72

[98] P M Morse and H Feshbach. *Methods of Theoretical Physics*, volume 1. McGraw-Hill, 1953. 38

[99] R J Le Roy. Energy levels of a diatomic near dissociation. *Molecular Spectroscopy*, 1:113, 1973. 41

[100] K T Tang and J P Toennies. An improved simple model for the van der Waals potential based on universal damping functions for the dispersion coefficients. *The Journal of Chemical Physics*, 80:3726, 1984. 41

[101] C Boisseau, I Simbotin, and R Côté. Macrodimers: Ultralong Range Rydberg Molecules. *Physical Review Letters*, 88:133004, 2002. 44

[102] J Brown and A Carrington. *Rotational Spectroscopy of Diatomic Molecules*. Cambridge University Press, 2003. 45

[103] S Sevincli, N Henkel, C Ates, and T Pohl. Nonlocal Nonlinear Optics in Cold Rydberg Gases. *Physical Review Letters*, 107:153001, 2011. 57, 66, 137, 138

[104] M Rafiq, M A Kalyar, and M A Baig. Multi-photon excitation spectra of the 3sn*l* (l =0,1,2 and 3) Rydberg states of magnesium. *Journal of Physics B*, 40:3181, 2007. 57

[105] M A Zia and M A Baig. Two-step laser optogalvanic spectroscopy of the odd-parity Rydberg states of atomic mercury. *The European Physical Journal D*, 28:323, 2004.

[106] A Nadeem, M Nawaz, S A Bhatti, and M A Baig. Multi-step laser excitation of the highly excited states of zinc. *Optics Communications*, 259:834, 2006.

[107] M Kompitsas, C Baharis, and Z Pan. Rydberg states of zinc and measurement of the dipole polarizability of the Zn^+ ion. *Journal of the Optical Society of America B*, 11:697, 1994. 57

[108] S M Farooqi, D Tong, S Krishnan, J Stanojevic, Y P Zhang, J R Ensher, A S Estrin, C Boisseau, R Côté, E E Eyler, and P L Gould. Long-Range Molecular Resonances in a Cold Rydberg Gas. *Physical Review Letters*, 91: 183002, 2003. 57

[109] J Nipper, J B Balewski, A T Krupp, B Butscher, R Löw, and T Pfau. Highly Resolved Measurements of Stark-Tuned Förster Resonances between Rydberg Atoms. *Physical Review Letters*, 108:113001, 2012. 57, 118

[110] I I Ryabtsev, D B Tretyakov, I I Beterov, and V M Entin. Observation of the Stark-Tuned Förster Resonance between Two Rydberg Atoms. *Physical Review Letters*, 104:073003, 2010. 57

[111] L Béguin, A Vernier, R Chicireanu, T Lahaye, and A Browaeys. Direct Measurement of the van der Waals Interaction between Two Rydberg Atoms. *Physical Review Letters*, 110:263201, 2013. 59, 60, 61

[112] W Li, C Ates, and I Lesanovsky. Nonadiabatic Motional Effects and Dissipative Blockade for Rydberg Atoms Excited from Optical Lattices or Microtraps. *Physical Review Letters*, 110:213005, 2013. 59

[113] C H Greene and M Aymar. Spin-orbit effects in the heavy alkaline-earth atoms. *Physical Review A*, 44:1773, 1991. 63, 77, 79

[114] Zhi M C, Dai C J, and Li S B. Stark structure of the Rydberg states of alkaline-earth atoms. *Chinese Physics*, 10:929, 2001. 67, 108, 137

[115] R Le Targat, L Lorini, Y Le Coq, M Zawada, J Guéna, M Abgrall, M Gurov, P Rosenbusch, D G Rovera, B Nagórny, R Gartman, P G Westergaard, M E Tobar, M Lours, G Santarelli, A Clairon, S Bize, P Laurent, P Lemonde, and J Lodewyck. Experimental realization of an optical second with strontium lattice clocks. *Nature Communications*, 4:2109, 2013. 68

[116] C Froese Fischer, T Brage, and P Jönsson. *Computational Atomic Structure*. IOP Publishing, 1997. 68

[117] P G Burke and K A Berrington. *Atomic and molecular processes : An R-Matrix approach*. IOP Publishing, 1993. 68

[118] R G Parr and W Yang. *Density-Functional Theory of Atoms and Molecules*. Oxford University Press, 1989. 68

[119] R D Cowan. *The Theory of Atomic Structure and Spectra*. University of California Press, 1981. 68, 79, 84

[120] J J Wynne and J A Armstrong. Systematic Behavior in Alkaline Earth Spectra: A Multichannel Quantum Defect Analysis. *IBM Journal of Research and Development*, 23:491, 1979. 68, 69, 72, 79, 92

[121] W E Cooke and C L Cromer. Multichannel quantum-defect theory and an equivalent N-level system. *Physical Review A*, 32:2725, 1985. 70

[122] Eric Jones, Travis Oliphant, Pearu Peterson, et al. SciPy: Open source scientific tools for Python, 2001–. URL http://www.scipy.org/. 75, 76

[123] U Fano. Quantum defect theory of l uncoupling in H_2 as an example of channel-interaction treatment. *Physical Review A*, 2:353, 1970. 76

[124] J E Sansonetti and G Nave. Wavelengths, Transition Probabilities, and Energy Levels for the Spectrum of Neutral Strontium (Sr I). *Journal of Physical and Chemical Reference Data*, 39:033103, 2010. 78, 79, 80, 84, 86, 87, 96, 98, 99

[125] M Aymar, P Camus, M Dieulin, and C Morillon. Two-photon spectroscopy of neutral barium: Observations of the highly excited even levels and theoretical analysis of the $J = 0$ spectrum. *Physical Review A*, 18:2173, 1978. 79

[126] J E Sansonetti. Wavelengths, Transition Probabilities, and Energy Levels for the Spectra of Strontium Ions (Sr II through Sr XXXVIII). *Journal of Physical and Chemical Reference Data*, 41:013102, 2012. 81

[127] C J Dai and X A Zhao. Study of Sr $5sns\,^1S_0 Rydberg Series$. *Journal of Quantitative Spectroscopy and Radiative Transfer*, 54:1019, 1995. 79, 100

[128] M Aymar, E Luc-Koenig, and S Watanabe. R-matrix calculation of eigenchannel multichannel quantum defect parameters for strontium. *Journal of Physics B*, 20:4325, 1987. 79, 82, 83, 84, 85, 89, 91, 92, 94, 95, 139

[129] E Luc-Koenig, M Aymar, J-M Lecomte, and A Lyras. Eigenchannel R-matrix study of two-photon excitation of low-lying autoionizing states in strontium: dielectronic core-polarization effects. *Journal of Physics B*, 31: 727, 1998. 79, 85, 91, 92

[130] C Froese Fischer and J E Hansen. Comparison of multichannel-quantum-defect theory and multiconfiguration-Hartree-Fock wave functions for alkaline-earth atoms. *Physical Review A*, 24:631, 1981. 79, 82, 92

[131] A Aspect, J Bauche, A L A Fonseca, P Grangier, and G Roger. Experimental and theoretical isotope shifts of strontium levels subject to very strong configuration mixing. *Journal of Physics B*, 17:1761, 1984. 79, 82, 92

[132] S Kunze, R Hohmann, H-J Kluge, J Lantzsch, L Monz, J Stenner, K Stratmann, K Wendth, and K Zimmer. Lifetime measurements of highly excited Rydberg states of strontium I. *Z. Phys. D*, 27:111, 1993. 84

[133] K T Lu. On the interaction between the 5s-p and 4d-p channels in Sr I. *Proc. Phys. Soc. London A*, 353:431, 1977. 85

[134] J J Wynne, J A Armstrong, and P Esherick. Zeeman Effect of $J = 2$ States of Sr: g-factor Variation for Interacting Rydberg Series. *Physical Review Letters*, 39:1520, 1977. 89, 93, 94

[135] M Kompitsas, S Cohen, C A Nicolaides, O Robaux, M Aymar, and P Camus. Observation and theoretical analysis of the odd $J = 3$ autoionising spectrum of Sr up to the 4d threshold. *Journal of Physics B*, 23:2247, 1990. 91, 96, 97

[136] J E Hansen and W Persson. Strong configuration interaction between 4d5p ^{1}F and the $5snf$ ^{1}F series in Sr I. *Journal of Physics B*, 10:L363, 1977. 96

[137] N Vaeck, M Godefroid, and J E Hansen. Multiconfiguration Hartree-Fock calculations for singlet terms in neutral strontium. *Physical Review A*, 38: 2830, 1988. 96, 98, 103

[138] A Lindgard. A Discussion of Mixing Coefficients Obtained Using the Many Channel Quantum Defect Theory in Fitting to Atomic Spectra and Their Use for Calculations of Lifetimes for B I and Al II. *Physica Scripta*, 26:84, 1982. 100

[139] M Aymar, R J Champeau, C Delsart, and J C Keller. Lifetimes of Rydberg levels in the perturbed 6snd ^{1,3}D$_2$ series of barium I. *Journal of Physics B*, 14:4489, 1981. 100

[140] R C Hilborn. Einstein coefficients, cross sections, f values, dipole moments, and all that. *American Journal of Physics*, 50:982, 1982. 102

[141] P Grafström, J Zhan-Kui, G Jönsson, C Levinson, H Lundberg, and S Svanberg. Natural radiative lifetimes in the interacting $5snd\,^{1,3}D_2$ sequences in Sr. *Physical Review A*, 27:947, 1983. 102

[142] W Gornik. Lifetime Measurements of Highly Excited Levels of Sr I Using Stepwise Excitation by Two Pulsed Dye Lasers. *Zeitschrift für Physik A*, 283:231, 1977. 102

[143] A L Osherovich, Ya F Verolainen, S A Pulkin, V I Privalov, and S M Lupekhin. Investigation of the radiative lifetimes of the excited states of Sr i and Sr ii. *Opt. Spectrosc.*, 46:134, 1979. 102

[144] H Bergström, C Levinson, and H Lundberg. Natural Radiative Lifetimes in the $5snd\,^1D_2$ Series of Sr I. *Z. Phys. D*, 2:127, 1986. 102, 104

[145] G Lochead. *Excited state spatial distributions in a cold strontium gas*. PhD thesis, University of Durham, 2012. 102, 137

[146] W H Parkinson, E M Reeves, and F S Tomkins. Neutral calcium, strontium and barium: determination of f values of the principal series by the hook method. *Journal of Physics B*, 9:157, 1976. 102

[147] J P Connerade, W A Farooq, H Ma, M Nawaz, and N Shen. Atomic f-value measurements of high Rydberg members by pulsed laser based magneto-optical spectroscopy. *Journal of Physics B*, 25:1405, 1992.

[148] W Mende and M Kock. Oscillator strengths of the Sr I principal series. *Journal of Physics B*, 30:5401, 1997.

[149] W Mende and M Kock. Oscillator strengths of Ba I and Sr I Rydberg transitions. *Journal of Physics B*, 29:655, 1996. 102, 103

[150] G D Scholes. Long-Range Resonance Energy Transfer in Molecular Systems. *Annual Reviews of Physical Chemistry*, 54:57, 2003. 109, 135

[151] C L Vaillant, M P A Jones, and R M Potvliege. MQDT models of Strontium Rydberg Series. *arXiv preprint arXiv:1402.5802*, 2013. 111

[152] L D Landau and E M Lifschitz. *Lehrbuch der Theoretischen Physik: Quantenmechanik*, volume 3. Akademie-Verlag: Berlin, 1974. 114

[153] A O Govorov. Spin-Förster transfer in optically excited quantum dots. *Physical Review B*, 71:155323, 2005. 117, 135

[154] A Imambekov, T L Schmidt, and Glazman L I. One-dimensional quantum liquids: Beyond the Luttinger liquid paradigm. *Reviews of Modern Physics*, 84:1253, 2012. 118, 134, 140

[155] I Bloch, J Dalibard, and S Nascimbène. Quantum simulations with ultracold quantum gases. *Nature Physics*, 8:267, 2012. 119

[156] I Bloch. Ultracold quantum gases in optical lattices. *Nature Physics*, 1:23, 2005. 119

[157] C J Foot. *Atomic Physics*. Oxford University Press: Oxford, 2005. 122, 132

[158] E Anderson, Z Bai, C Bischof, S Blackford, J Demmel, J Dongarra, J Du Croz, A Greenbaum, S Hammarling, A McKenney, and D Sorensen. *LAPACK Users' Guide*. Society for Industrial and Applied Mathematics, Philadelphia, PA, third edition, 1999. ISBN 0-89871-447-8 (paperback). 123

[159] R. Clint Whaley and Antoine Petitet. Minimizing development and maintenance costs in supporting persistently optimized BLAS. *Software: Practice and Experience*, 35:101–121, February 2005. 123

[160] M. Born and V. Fock. Beweis des Adiabatensatzes. *Zeitschrift fr Physik*, 51: 165, 1928. 124

[161] C Kittel. *Introduction to Solid State Physics*. Wiley and Sons: New York, 1953. 126, 133

[162] X Li, P L Voss, J E Sharping, and P Kumar. Optical-Fiber Source of Polarization-Entangled Photons in the 1550 nm Telecom Band. *Physical Review Letters*, 94:053601, 2005. 127

[163] A Recati, P O Fedichev, W Zwerger, and P Zoller. Spin-Charge Separation in Ultracold Quantum Gases. *Physical Review Letters*, 90:020401, 2003. 129, 136, 139

[164] I. Zutic, J. Fabian, and S. Das Sarma. Spintronics: Fundamentals and applications. *Review of Modern Physics*, 76:323, 2004. 133

[165] M J Seaton. Quantum defect theory I. General formulation. *Proceedings of the Physical Society*, 88:801, 1966. 137

[166] G Bannasch, T C Killian, and T Pohl. Strongly Coupled Plasmas via Rydberg Blockade of Cold Atoms. *Physical Review Letters*, 110:253003, 2013. 140

[167] S Ye, X Zhang, T C Killian, F B Dunning, M Hiller, S Yoshida, S Nagele, and J Burgdörfer. Production of very-high-n strontium Rydberg atoms. *Physical Review A*, 88:043430, 2013. 140

[168] A Messiah. *Quantum mechanics*, volume 1. (North Holland: Amsterdam, english edition, 1962. 143